

The origin of metal and chondrules in CH and CB
chondrites – Evidence from Fe, Ni, and Si isotopes and
trace element compositions

Von der Naturwissenschaftlichen Fakultät der
Gottfried Wilhelm Leibniz Universität Hannover
zur Erlangung des Grades
Doktorin der Naturwissenschaften (Dr. rer. nat.)

genehmigte Dissertation

von

Mona Weyrauch, M. Sc.

2018

Referent: Prof. Dr. Stefan Weyer

Korreferenten: Prof. Dr. Addi Bischoff
Prof. Dr. Franz Renz

Tag der Promotion: 07.09.2018

Acknowledgements

First of all, I want to thank Stefan Weyer and Jutta Zipfel for giving me the opportunity to write this thesis and for the fruitful discussions that carried my work forward.

Moreover, I am grateful to the DFG (Deutsche Forschungsgemeinschaft e.V.) for funding this project within the special priority program “The first 10 million years of the solar system – a planetary materials approach” (SPP 1385).

I am thankful for the technical support I got from Heidi Höfer and Markus Schölmerich with the electron microprobe in Frankfurt, and from Chao Zhang and Renat Almeev with the EMPA in Hannover. Help with the LA-ICP-MS analyses came from Ingo Horn, Stephan Schuth, and most of all from Martin Oeser-Rabe who also introduced me to LA-ICP-MS measurements. I thank Annika Brüske for helping me with my first attempts of column separation in the clean lab and solution analyses. Julian Feige and Tina Emmel need to be thanked for sample preparation.

I also want to thank Rainer Bartoschewitz for providing a sample from his private collection to be analyzed in this study, and also the Meteorite working group for lending Antarctic meteorites to enhance the statistics of this thesis.

I very much appreciate my colleagues, who made work more enjoyable. Especially Lena, Lennart, Yvonne, Dominik, Martin, and Moritz. Thank you for all the coffee breaks with chocolate, and technical, and non-technical discussions.

Most of all, I am grateful for the endless support of my family throughout the years.

Abstract

The formation processes of the unusually metal-rich CB and CH chondrites are highly debated. Chemically and isotopically zoned metal, unzoned metal, and cryptocrystalline (CC) chondrules from these meteorites are proposed to have formed by condensation. However, it is still unclear if they condensed directly from the solar nebula or from an impact-induced vapor plume, and how metal and chondrule formation are related. This thesis aims at unravelling the formation conditions of CH and CB chondrite constituents by laser ablation analyses of Fe, Ni, and Si isotopes in combination with trace element analyses.

Parallel zoning of Fe and Ni isotopes in zoned metal from CH and CB_b chondrites confirm a condensation origin of the zoning and exclude exchange diffusion as the formation process. Tungsten in zoned metal grains is depleted relative to other refractory elements which is suggestive for elevated oxygen fugacities in the gas reservoir, and thus, also for an impact event. Combined results of isotope and trace element analyses reveal that zoned metal formed in the fast-cooling shell regions, which favor kinetic fractionation while unzoned metal would have condensed from the slow-cooling interior of the plume under more equilibrium-like conditions.

CC chondrules from CH and CB_b chondrites were analyzed for Si isotope and trace element compositions to unravel their formation histories. Trace element abundances revealed two different populations of CC chondrules: (1) superchondritic refractory element contents and depletion in volatile elements most likely condensed from an unfractionated reservoir, and (2) with generally subchondritic element contents formed from a reservoir that was fractionated beforehand by an ultrarefractory phase. Tungsten, Mo, and Cr concentrations in metal and chondrules indicate elevated oxygen fugacities, and formation of those constituents from a closed system. Silicon isotope compositions of chondrules are heavier than BSE and the chondritic average. Thus, we propose that light Si isotopes were extracted from the gas reservoir, either due to the impact or by condensation of forsterite or melilite prior to CC chondrule formation.

A relationship between CB, CH, and CR chondrites is proposed due to isotopic similarities (Cr, Ti, N, O), high metal contents, and similarities in hydrated clasts from CH and CB chondrites with CR matrix. Iron and Ni isotope results, combined with trace element contents, reveal relatively homogeneous composition of CR chondrite metal. These findings combined with textural differences, lead to the conclusion that metal from CR chondrites did not form in the same event as that of CH and CB chondrites.

Bulk isotopic similarities (Cr, Ti, N, O) of the three chondrite groups may reflect (1) formation of precursor material in the same region, (2) accretion in the same region, or (3) inheritance of the isotope signature of a CR impactor by CH and CB chondrites.

Zusammenfassung

Die Bildungsprozesse der ungewöhnlich metallreichen CB- und CH-Chondrite sind sehr umstritten. Es wird diskutiert, dass sich chemisch und isotopisch zonierte Metall, unzoniertes Metall und kryptokristalline (CC) Chondren dieser Meteorite durch Kondensation gebildet haben. Es ist jedoch immer noch unklar, ob sie direkt aus dem solaren Nebel oder aus einer Impaktwolke kondensiert sind und wie die Metall- und Chondrenbildung zusammenhängen. Ziel dieser Arbeit ist es, die Entstehungsbedingungen dieser CH- und CB-Chondritbestandteile durch Laserablationsanalysen der Fe-, Ni- und Si-Isotopen in Kombination mit Spurenelementanalysen aufzuklären.

Die parallele Zonierung von Fe- und Ni-Isotopen in zonierten Metallen aus CH- und CB_b-Chondriten bestätigt einen Kondensationsursprung der Zonierung und schließt diffusiven Austausch der Elemente als Bildungsprozess aus. Wolfram in zonierten Metallkörnern ist gegenüber anderen refraktären Elementen verarmt, dies ist ein Hinweis auf erhöhte Sauerstofffugazitäten im Gasreservoir und somit auch auf ein Impaktereignis. Kombinierte Isotopen- und Spurenelementanalysen zeigen, dass zonierte Metall in den schnell abkühlenden äußeren Regionen gebildet wird, in welchen die kinetische Fraktionierung begünstigt wird. Unzoniertes Metall kondensiert aus dem langsam abkühlenden Inneren der Wolke unter gleichgewichtsähnlicheren Bedingungen.

CC-Chondren aus CH- und CB_b-Chondriten wurden auf ihre Si-Isotopen- und Spurenelementzusammensetzungen analysiert, um ihre Entstehungsgeschichte zu entschlüsseln. Die Spurenelementhäufigkeiten zeigen zwei unterschiedliche Populationen von CC-Chondren: (1) superchondritische refraktäre Elementgehalte und Verarmung in volatilen Elementen kondensiert aus einem unfraktionierten Reservoir, und (2) mit generell subchondritischen Elementgehalten aus einem Reservoir, das zuvor durch eine ultra-refraktäre Phase fraktioniert wurde. Wolfram-, Mo- und Cr-Konzentrationen in Metall und Chondren weisen auf erhöhte Sauerstofffugazitäten und die Bildung dieser Bestandteile aus einem geschlossenen System hin. Siliziumisotopenzusammensetzungen der Chondren sind schwerer als BSE und der chondritische Durchschnitt. Daher ist es wahrscheinlich, dass leichte Si-Isotope aus dem Gasreservoir entzogen wurden, entweder aufgrund eines Impakts oder der Kondensation von Forsterit oder Melilit vor der CC-Chondrenbildung.

Aufgrund von Isotopenähnlichkeiten (Cr, Ti, N, O), hohen Metallgehalten und Ähnlichkeiten hydrierter Klasten in CH- und CB-Chondriten mit CR-Matrix, wird eine Verwandtschaft zwischen CB-, CH- und CR-Chondriten angenommen. Ergebnisse der Eisen- und Ni-Isotopenmessungen, kombiniert mit Spurenelementgehalten, zeigen eine relativ homogene Zusammensetzung von CR-Chondrit Metall. Diese Ergebnisse, kombiniert mit Unterschieden im Gefüge, führen zu der Schlussfolgerung, dass das Metall der CR-Chondrite nicht im selben Prozess gebildet wurde wie das der CH- und CB-Chondrite.

Ähnlichkeiten der isotopischen Gesamtzusammensetzung (Cr, Ti, N, O) der drei Chondritgruppen können auf (1) die Bildung von Vorläufermaterial in der gleichen Region, (2) die Akkretion in der gleichen Region oder (3) die Vererbung der Isotopensignatur von einem CR-Impaktor auf CH- und CB-Chondrite hinweisen.

Schlagwörter/Keywords

Schlagwörter: metallreiche Chondrite, Fe,Ni-Metall, Kondensation, Fe Isotopie, Ni Isotopie, Spurenelemente, Impakt, Chondren

Keywords: metal-rich chondrites, Fe,Ni-metal, condensation, Fe isotopes, Ni isotopes, trace elements, impact, chondrules

Table of Contents

Acknowledgements.....	III
Abstract.....	IV
Zusammenfassung.....	V
Schlagwörter/Keywords.....	VI
Table of Contents.....	VII
Objectives and Background.....	X
Part I - <i>In situ</i> high-precision Ni isotope analysis of metals with femtosecond LA – MC – ICP – MS.....	16
1 Abstract.....	16
2 Introduction.....	17
3 Materials and samples.....	18
4 Experimental.....	19
4.1 Sample preparation for the solution nebulization MC-ICP-MS bulk analysis.....	19
4.2 Bulk solution nebulization MC-ICP-MS.....	19
4.3 <i>In situ</i> Ni isotope determinations by <i>fs</i> -LA-MC-ICP-MS.....	20
5 <i>In situ</i> isotope analyses of meteorites.....	21
6 Results and discussion.....	23
6.1 Sample homogeneity.....	23
6.2 Comparison of bulk solution and laser ablation analyses.....	26
6.3 Application to Kamacite-Taenite interfaces in iron meteorites.....	28
7 Conclusions.....	30
Part II: Origin of metal from CB chondrites in an impact plume - A combined study of Fe and Ni isotope composition and trace element abundances.....	32

Table of Contents

1 Abstract	32
2 Introduction.....	33
3 Samples and Methods.....	34
3.1 Petrography of the examined meteorites.....	34
3.1.1 CB _a Chondrites	36
3.1.2 CB _b Chondrites	36
3.1.3 CH/CB _b breccia Isheyevo	37
3.2 Analytical procedures.....	37
4 Results.....	40
4.1 Zoned metal.....	40
4.1.1 Chemical composition	40
4.1.2 Isotopic composition of zoned metal.....	42
4.2 Unzoned metal	44
4.2.1 Chemical composition	44
4.2.2 Isotopic composition.....	45
5 Discussion.....	46
5.1 Origin of zoning in metal	46
5.2 Compositional variation of zoned metal	48
5.3 Compositional variations of unzoned metal.....	48
5.4 Properties of the impact plume	50
5.4.1 Gas evolution during condensation of zoned and unzoned metal.....	50
5.4.2 Oxidizing conditions in the impact plume: Evidence from Mo and W	53
5.5 Possible formation processes of unusual zoning patterns in metal	54
5.5.1 Uncontinuous zoning and plessite	54
5.5.2 Reversed zoning in grains from Isheyevo	55
6 Conclusion	56
 Part III: Constraints on the relationship of CH, CB, and CR chondrites from	
metal grains.....	57
1 Abstract	57
2 Introduction.....	58
3 Samples and Methods.....	60
3.1 Petrographic description.....	60
3.1.1 CB _a (Gujba, Bencubbin, NWA 4025).....	61
3.1.2 CB _b (HaH 237, QUE 94411, MAC 02675)	61
3.1.3 CH/CB _b breccia (Isheyevo).....	62
3.1.4 CH (Acfer 214, PAT 91546, SaU 290)	62
3.1.5 CR (NWA 852).....	63
3.2 Analytical Procedure	64
4 Results.....	64
4.1 Chemical and isotopic characteristics of metal from CH chondrites.....	64
4.1.1 Zoned metal.....	65
4.1.2 Unzoned metal	67
4.2 Chemical and isotopic characteristics of metal from CR chondrites	68
4.3 Isotopic and chemical similarities and differences of CR, CB, and CH chondrites' metal.....	71
5 Discussion.....	74
5.1 Formation conditions and relationship of CB and CH chondrite metal	74
5.2 Modelling of formation conditions of zoned metal from CH and CB _b samples ..	75
5.3 Possible formation conditions of CR chondrite metal.....	76
5.4 Possible relationship of CR, CB, and CH chondrites	77
6 Conclusion	78

**Part IV: Evidence for the formation conditions of cryptocrystalline
chondrules from CH and CB_b chondrites from their trace element**

composition	80
1 Abstract	80
2 Introduction.....	81
3 Samples and Methods.....	82
4 Results.....	84
4.1 Chemical composition of CC chondrules.....	84
4.1.1 Superchondritic chondrules	85
4.1.2 Subchondritic chondrules.....	86
4.2 Si isotope composition	88
5 Discussion.....	89
5.1 Formation conditions of CC chondrules in CH and CB _b chondrites	89
5.2 Constraints on the formation of CC chondrules from their Si isotope compositions.....	91
5.3 Relation of chondrules and metal in CH and CB chondrites	92
6 Conclusion	94
Conclusion and Outlook	96
References.....	99
Appendix.....	105
1 Appendix Part I.....	106
2 Appendix Part II.....	109
3 Appendix Part III	114
4 Appendix Part IV	118
5 Curriculum Vitae	120
6 List of publications	122

Objectives and Background

Objectives and Background

This dissertation aims to unravel the formation histories and the relationship of CH, CB and CR chondrites. For this purpose, samples are being investigated by laser ablation mass spectrometry to measure Fe, Ni, and Si isotope compositions of the constituents of the samples, as well as their trace element abundances.

CR CLAN CHONDRITES

Meteorites are fragments of the oldest solid materials we know. Thus, they are the most suitable archives to investigate the early stages of planet formation in our solar system. Chondritic meteorites are especially important as they contain the oldest solid material known in our solar system (CAIs). The initial composition of chondrites is often overprinted by thermal metamorphism or aqueous alteration (petrologic types 3.1-6 and 1-2, respectively). Meteorites which do not show signs of such overprinting have the most primordial composition and are considered to faithfully have recorded the conditions of their formation quite well. Pristine chondrites mainly consist of chondrules, which are siliceous spherules that formed from melt droplets by rapid cooling, embedded into fine-grained matrix material (Fig. 1a).

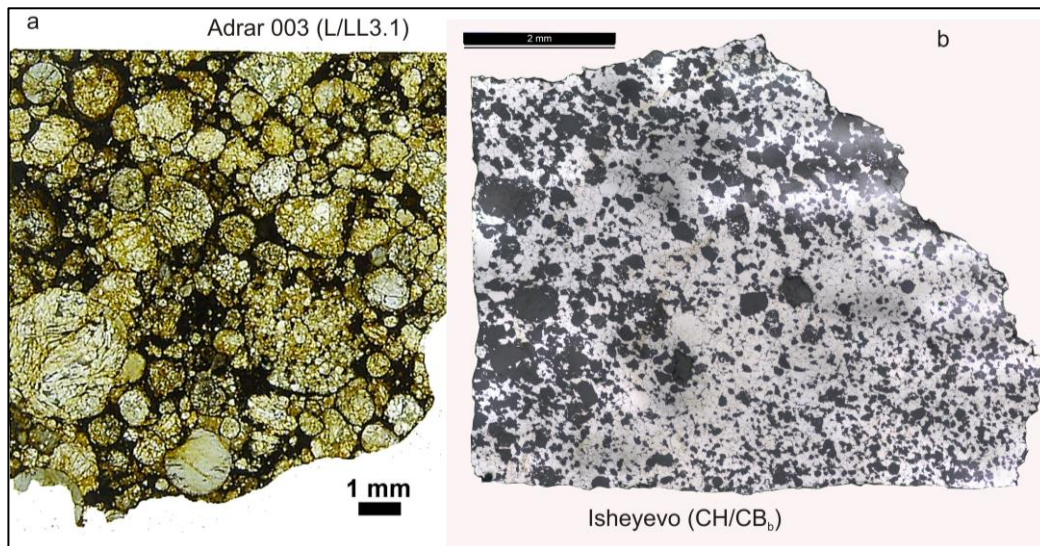


Figure 1: Overview pictures of an ordinary chondrite (a) which is rich in chondrules and a metal-rich chondrite (b). (a) image in transmitted light; brownish rounded objects are chondrules, black areas are matrix and opaque phases. (b) image in reflected light; white areas represent metal, greyish objects are silicates. The image of Adrar 003 is kindly provided by the Institut für Planetologie (WWU Münster).

CH and CB chondrites do not show any signs for thermal metamorphism or aqueous alteration and thus, are very pristine in their composition (Krot et al., 2002). However, petrologic types cannot easily be assigned to them as they are very special among the primitive

Objectives and Background

meteorites. They have extraordinarily high metal contents (Fig. 1b) of 20-40 vol% (CH) and ~70 vol% (CB), and lack matrix material (Krot et al., 2002). Moreover, they are chemically somewhat different from other primitive meteorites as they are depleted in moderately volatile elements (Zipfel et al., 1998). Another unusual characteristic are chondrule ages that are about 2 Ma younger than those of other chondrite types (Kleine et al., 2005; Krot et al., 2005; Bollard et al., 2015). All these outstanding properties of CH and CB chondrites makes them very interesting objects for investigation of early Solar System processes, as they may give more information about the diversity of planet-forming processes and the timespan in which those processes proceeded.

CR chondrites are thought to be related to CH and CB chondrites based on their similar N and O isotope compositions (Franchi et al., 1986; Clayton, 1993; Clayton and Mayeda, 1999) and other akin characteristics, such as a bulk depletion in moderately volatile elements and Mg-rich mafic silicates (Krot et al., 2002). The three chondrite groups are merged together to the CR clan chondrites (Weisberg et al., 1995; Krot et al., 2002). Thus, it is reasonable to examine all three chondrite groups to unravel their formation conditions and relationship.

IN SITU ISOTOPE ANALYSES – FE AND NI ISOTOPE SYSTEMS

Iron is a highly abundant element in most rock-forming minerals. In terrestrial samples Fe isotope analyses are performed as planetary differentiation processes, result in characteristic Fe isotope fractionation between different reservoirs on Earth and other terrestrial planets, such as Mars (Dauphas et al., 2017). On smaller scales iron isotope investigations also allow to draw conclusions on the relationship of different mineral phases within a rock (Dauphas, 2007). In situ isotope analyses with high spatial resolution give the possibility to distinguish between various kinetic processes such as diffusion, evaporation or condensation. Laser ablation techniques (especially if using a femtosecond laser) combined with high mass resolution MC-ICP-MS enables Fe isotope analyses with both high spatial resolution and high precision (0.1‰, (Steinhefel et al., 2009; Oeser et al., 2014)). In contrast to other in situ techniques, femtosecond laser ablation mass spectrometry (*fs*LA-ICP-MS) is not biased by matrix effects or thermal fractionation (Poitrasson et al., 2003; Horn et al., 2006).

In meteorites, Fe is abundant in silicate phases but even more in Fe,Ni-alloys. Iron isotopes have mainly been investigated in meteorites to reveal the relationship of type I and type II chondrules, as it was suggested that type I chondrules formed by Fe evaporation of type II chondrule material (Alexander and Wang, 2001). Moreover, Fe isotope compositions were measured for the different iron meteorite metal phases (Poitrasson et al., 2005; Dauphas, 2007). Nickel-rich taenite and Ni-poor kamacite. It was observed that taenite is heavier than kamacite

Objectives and Background

(Poitrasson et al., 2005; Dauphas, 2007). From chemical gradients and the difference in iron isotope composition it was suggested that diffusion of Fe between the two phases played a substantial role in the formation of an assemblage of the two phases (Brearley and Jones, 1998; Poitrasson et al., 2005; Dauphas, 2007). High spatial resolution measurements with LA-ICP-MS allow to measure full profiles of such an assemblage. However, Fe isotope analyses alone do not allow to quantify the formation conditions such as cooling rates, temperature and pressure. Likewise, they do not allow to specify the formation conditions of chemically and isotopically zoned metal grains which were found in CB_b and CH chondrites (e.g., Meibom et al., 1999). To determine if zoning in those phases was formed by diffusion or condensation processes, it is necessary to analyse a second isotope system of a metal with similar chemical zoning.

For such purposes, I also measured the Ni isotope composition in those phases in addition to iron isotopes. With the combination of both isotope systems it is possible to reveal the nature of zoning within the metal phases. Diffusion can be revealed by opposed zoning of the two isotope systems, while condensation is represented by parallel zoning of Fe and Ni isotope compositions. Such combined in situ Fe and Ni isotope studies were first performed in the case of this study. It was necessary to develop a new measurement set up for in situ measurements of Ni isotopes with LA-MC-ICP-MS for that (Part I). The new measurement technique was then applied to the analyses of zoned Fe,Ni-metal grains from CB_b and CH chondrites (Part II & III). Another application was the investigation of kamacite taenite exsolution (by the investigation of the kamacite taenite interface, in Part I) and also the formation of other iron-bearing phases in pallasites and iron meteorites within an international cooperation (Chernozhkin et al., 2017).

SI ISOTOPE SYSTEM

Silicon contents are strongly varying among the different meteorite types, however, Si is always one of the most abundant elements in silicate meteorites. Silicon isotope analyses are well established in cosmochemistry. Early findings showed mass-independent fractionations in presolar grains and some rare CAIs.

Objectives and Background

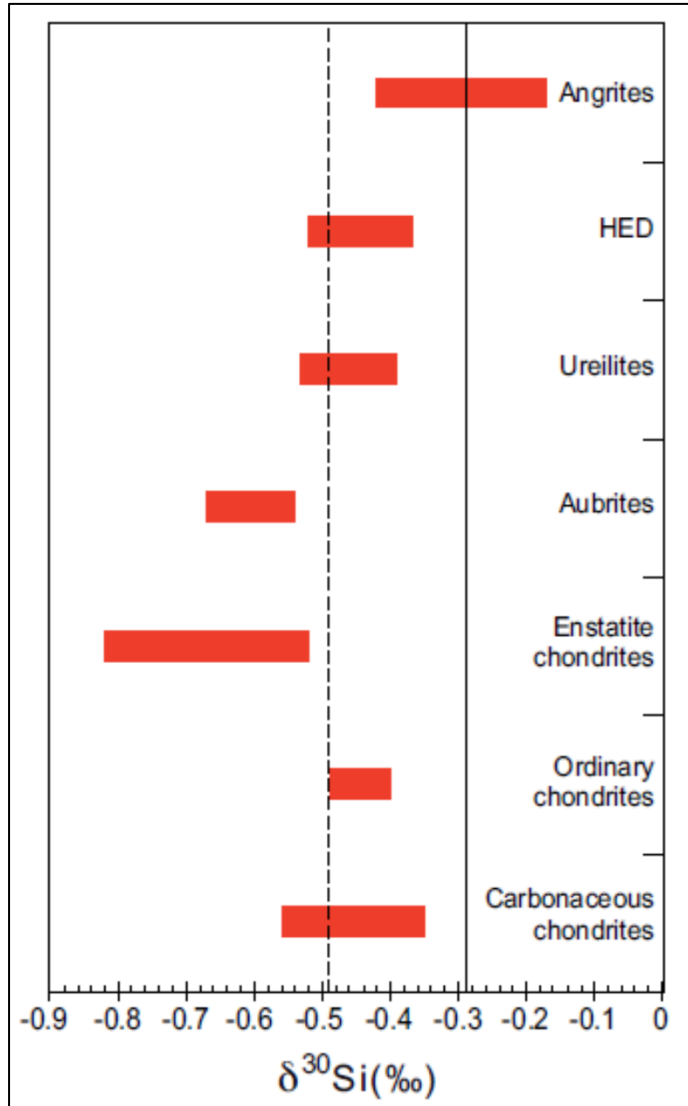


Figure 2: Si isotope compositions of the different meteorite groups (Figure 3 from Poitrasson, 2017). The solid line represents the estimated BSE value, dashed line represent Si isotope composition of Mars.

However, other extraterrestrial materials do not show mass-independent fractionation of Si isotopes (Poitrasson, 2017). Silicon isotope studies showed that it is possible to distinguish some meteorite groups from others by their $\delta^{30}\text{Si}$ compositions (Fitoussi et al., 2009; Pringle et al., 2013). All primitive meteorites show lighter isotope composition than the bulk silicate earth (BSE, Fig. 2), enstatite chondrites (EC) have the lightest composition (Poitrasson, 2017). However, the silicate portion of EC was shown to have similar Si isotope values as ordinary chondrites (OC) and carbonaceous chondrites (CC) (Savage and Moynier, 2013), which overlap in their Si isotope compositions and plot between bulk EC and BSE. The achondrite groups of Ureilites and HED (Howardites-Eucrites-Diogenites) are indistinguishable from OC and CC in their Si isotope compositions (Poitrasson, 2017). Due to these compositional similarities, it is suggested that the protoplanetary accretion disk was homogeneous in Si isotope composition (Pringle et al., 2013). Nonetheless, the achondrite group of Angrites and the Moon have similar ^{30}Si values as the BSE. The heavy Si isotope compositions of BSE and Moon are considered

Objectives and Background

to be result of Si isotope fractionation during formation of proto-Earth's core (before the giant impact, Georg et al., 2007). In contrast, the heavy Si isotope composition of angrites compared to other meteorite types is discussed to be a consequence of light Si isotope loss related to an impact event (Pringle et al., 2014) or due to isotope fractionation during high temperature condensation in the solar nebula (Dauphas et al., 2015). Thus, Si isotopes may provide important information on planet formation and differentiation processes.

TRACE ELEMENT INVESTIGATION

In addition to isotope analyses, trace element abundances were determined. Trace element concentrations may deliver information about the processes that occurred during formation of examined chondrules and metal grains. In cosmochemistry, trace element patterns are often used for classification of constituents. Such as subdivision of CAIs into different groups (Brearley and Jones, 1998 and references therein). Where each group has different rare earth element (REE) abundance patterns that indicate variable condensation and evaporation effects during formation of CAIs (Brearley and Jones, 1998 and references therein). Moreover, trace element abundances were used to clarify formation conditions of metal sulfide silicate intergrowths (MSSI) in enstatite chondrites. Some abundance patterns are interpreted to represent melting processes (Horstmann et al., 2014), others interpret those patterns as evidence for condensation (El Goresy et al., 2016).

Trace element concentrations measured for the here examined metal grains and chondrules are evaluated with focus on the cosmochemical behavior of the elements. Abundance patterns that indicate fractionation of the elements controlled by the volatility of the elements, may be evidence for formation by condensation of metal and chondrules.

OBJECTIVES

Part I describes the development of a highly precision and high spatial resolution technique for in situ Ni isotope analyses via laser ablation. This was necessary since no such technique was established before and both, Fe and Ni, isotope systems are needed to determine processes within Fe,Ni-metal. In order to develop this analytical method, the characterization of potential standards was required. After successful identification of standards and demonstration of repeatability of our results, the method was applied to a taenite-kamacite profile in combination with Fe isotope analyses. This confirmed that diffusional exchange, of Fe and Ni, during exsolution of kamacite from taenite can be verified by the isotope zoning between the two phases.

Objectives and Background

Part II aims at identifying the formation process of zoned and unzoned metal from CB chondrites. In situ Fe and Ni isotope, and trace element analyses are used in order to unravel if zoned and unzoned metal were formed by condensation and if they were formed in the same process. Another important question is whether metal from CB chondrites formed in an impact induced vapor plume or if it formed directly from the solar nebula. Furthermore, data may give hint towards the relationship of CB_a and CB_b chondrites.

In **Part III**, CR and CH chondrite metal are being comparatively investigated with CB chondrite metal, using the same methods, in order to clarify the relationship of the different meteorite groups. Like CB_b chondrites, CH chondrites contain zoned metal grains. Thus, chemical and isotopic results can indicate if zoned metals from CH and CB_b chondrites have the same origin. Additionally, it will be examined if CR chondrite metal can have formed in the same process as metal of CH and CB chondrites. All groups have some important chemical and isotopic features in common, but also show significant differences, especially in their textures.

Objective of **Part IV** is to reveal the formation origin of chondrules (with a focus on cryptocrystalline chondrules, CC) from CH and CB_b chondrites. Trace element data and Si isotope compositions may give information about the formation conditions and help shed light on the relationship of chondrules with the metal from CH and CB_b chondrites. An important question addressed is, whether some or even all chondrules formed in the same event as metal or whether they formed in a separate event.

Part I - *In situ* high-precision Ni isotope analysis of metals with femtosecond LA – MC – ICP - MS

Modified version published in *Journal of Analytical Atomic Spectrometry*:

Weyrauch M., Oeser M., Brüske A., and Weyer S. (2017). *In situ* high precision Ni isotope analysis of metals with femtosecond LA-MC-ICP-MS. *J. Anal. At. Spectrom.* **32**, 1312-1319.

DOI: 10.1039/c7ja00147a

1 ABSTRACT

In this study, an *in situ* technique for high-precision determination of Ni stable isotope ratios by femtosecond-laser ablation - multi collector – ICP – MS (fs-LA-MC-ICP-MS) was developed. With this technique, the Ni isotope compositions of Ni-bearing steels (NIST RM-1226 and BAM D 184-1) and a Ni-rod (standard 10209 from MAC) was determined, both by fs-LA-MC-ICP-MS analyses and by solution MC-ICP-MS, the latter in order to verify the results of the *in situ* analyses. The LA-MC-ICP-MS analyses revealed that all analyzed standard material was homogeneous within analytical uncertainties and may thus be suitable as external standards for Ni isotope determination by *in situ* analysis of metal phases and sulfides. Bulk solution MC-ICP-MS and LA-MC-ICP-MS analyses for these metals agreed within their analytical uncertainties of 0.03 ‰ for the solution analyses and < 0.1‰ (2SD, over 12months) for the LA-MC-ICP-MS analyses. These results imply that the accuracy of the *in situ* analyses of metals is better than 0.1 ‰. The average of four solution nebulization analyses of the Ni-rod and D 184-1, and of 16 analyses of NIST RM-1226 material, revealed $\delta^{62}\text{Ni}$ values of -0.26 ‰, 0.12 ‰, and -0.28 ‰ relative to NIST SRM-986, respectively.

In order to show the applicability and potential of the presented method, the Ni and Fe isotope composition of a kamacite-taenite interface in IAB iron meteorite Canyon Diablo was determined by fs-LA-MC-ICP-MS analyses. The isotope profile reveals lighter Fe isotopes in kamacite than in taenite, while Ni isotope composition is vice versa. Evolution of the isotope signals along the interface of these metal phases strongly points to diffusion-driven fractionation of Fe and Ni isotopes during the formation of kamacite by the replacement of

Part I: *In situ* Ni isotope analysis via fsLA-MC-ICP-MS

taenite. Due to Fe-Ni exchange diffusion between taenite and kamacite and the generally faster diffusion of light isotopes compared to heavy isotopes, the remaining taenite is left with heavier Fe and lighter Ni isotope composition than the newly-formed kamacite. Demonstration of such detailed information about the diffusion processes in the kamacite-taenite system was not possible before, due to the lack of an appropriate high-precision and high spatial resolution technique for *in situ* Ni isotope analyses.

2 INTRODUCTION

Nickel isotope measurements are especially useful in the field of cosmochemistry. Since ^{60}Ni is the daughter isotope of the short lived nuclide ^{60}Fe , Ni isotope analyses represent an important way to receive information about the possible role of ^{60}Fe as a heat source in the early solar system and may also function as a chronometer (Elliot and Steele, 2017). Moreover, abundance of the five different stable Ni isotopes varies with the stellar environment. Thus, conclusions may be drawn on the nucleosynthetic origin of Ni from Ni isotope analyses (Elliot and Steele, 2017) (and references therein). Nickel is abundant in Fe-Ni alloys in meteorites with heterogeneous distribution of Ni concentration among different alloy phases (kamacite and taenite (Reed, 1965; Narayan and Goldstein, 1985; Brearley and Jones, 1998)) or even show zoning within single metal grains (Weisberg and Prinz, 1999). Previous studies have shown that Fe-Ni-metal phases (kamacite and taenite) from meteorites have different Fe and Ni stable isotope compositions (Poitrasson et al., 2005; Horn et al., 2006; Cook et al., 2007; Dauphas, 2007). However, these studies are based on microdrilling techniques and subsequent analyses of sample solutions. Thus, spatial resolution is rather low ($\sim 400\ \mu\text{m}$ (Cook et al., 2007)) and no fully resolved profile of the kamacite-taenite interface could be determined (cf. (Richter et al., 2009)). Thus, *in situ* isotope analyses are necessary to resolve the evolution of isotope composition along such an interface or to analyze Fe,Ni-isotope compositions of small metal grains from meteorites (e.g., (Weisberg and Prinz, 1999)). Ni isotope compositions of such zoned metal grains were already determined with ion probe measurements (Alexander and Hewins, 2004; Richter et al., 2014). However, these measurements have rather large uncertainties with a minimum of 1‰/amu. Also individual olivine grains of ureilites were already investigated for their Ni isotope composition (Kita et al., 1997) with an ion probe. Uncertainties on those measurements are even bigger with 3-4 ‰ on $^{62/61}\text{Ni}$, unfortunately it is not clearly stated in that work if this is the uncertainty on the isotope ratio or on the δ -values. Thus, a more precise analytical method to determine Ni isotope composition is needed, as Ni isotope variations are frequently small and thus cannot be resolved by ion probe investigation

Part I: *In situ* Ni isotope analysis via fsLA-MC-ICP-MS

due to high analytical uncertainties. To achieve precise Ni isotope measurements with high spatial resolution, we combine a femtosecond laser ablation system with high mass resolution MC-ICP-MS. A big advantage of the femtosecond laser is that there is only minor thermal interaction with the sample material, essentially avoiding isotope fractionation during laser ablation (e.g., (Poitrasson et al., 2003) and (Fernández et al., 2007)). For any method of *in situ* isotope analyses, an appropriate homogeneous standard material with known isotope composition is necessary. Since the commonly used Ni isotope standard NIST SRM-986, is only available as powder, it is unsuitable for *in situ* isotope analysis with LA-MC-ICP-MS. Though fs-LA-MC-ICP-MS measurements can be performed essentially matrix-independent (Poitrasson et al., 2003; Fernández et al., 2007), we selected standard materials, two Ni-bearing steels and a pure Ni rod, that are compositionally close to our target sample materials (meteorite metals). The investigated metals were characterized for their Ni isotope composition with bulk solution nebulization MC-ICP-MS and comparatively with fs-LA-MC-ICP-MS analysis (1) to determine the precision and accuracy of our *in situ* method, (2) to precisely determine the Ni isotope compositions of the potential standards and (3) to check their isotopic homogeneity. We further demonstrate the applicability of the herewith developed analytical method by determination of a Fe and Ni isotope profile of a kamacite-taenite interface from the iron meteorite Canyon Diablo. This application shows that analyses of Ni- in combination with Fe stable isotope ratios with high precision and high spatial resolution in isotopically heterogeneous meteorite samples, allows drawing constraints on their formation processes.

3 MATERIALS AND SAMPLES

Ni-bearing steels and a Ni-rod that are available as electron microprobe standards were investigated. The Ni-bearing steels comprise the certified BAM (Bundesanstalt für Materialforschung und –Prüfung) standard D-184.1 and the NIST standard RM 1226. A Ni-rod is analyzed as well (standard 10209 from MAC, Micro-Analysis Consultants Ltd.). The Ni-bearing steels were chosen due to having similar chemical composition as the sample material we want to analyze. The Ni-rod was chosen as a standard material with a high Ni content to check if our *in situ* determined Ni isotope composition is independent on the Fe/Ni ratio. All potential standards were mounted and polished. Additionally, the Ni isotope composition of the Ni ICP standard solution from Merck was determined (batch no. 1.70382.0100). Furthermore, the herewith developed *in situ* analysis technique was applied to measure a kamacite-taenite profile in Canyon Diablo, a main group IAB iron meteorite.

4 EXPERIMENTAL

4.1 Sample preparation for the solution nebulization MC-ICP-MS bulk analysis

Four chips of NIST RM-1226 with weights between 50 and 70 mg were dissolved in 5 mL of aqua regia (3:1, concentrated HCl, and concentrated HNO₃, both from Merck, distilled from pa grade) at 120 °C for 24 hours in Savillex® Teflon beakers, yielding 4 individual sample solutions of NIST RM-1226. One sample solution of BAM D-184.1 was produced by treating ~100 mg (consisting of numerous flakes) of the steel in the same manner as material from NIST RM-1226. An aliquot of the Ni-rod (~20 mg) was dissolved in 5 mL 2 mol/L HNO₃ at 120 °C. All samples except for the pure Ni-rod were purified and separated from matrix elements following the procedure of (Cook et al., 2006) for ion exchange chromatography. Only the first step (Fe separation) of the procedure was performed since all other elements have negligibly low concentrations. Iron was separated from the samples by anion exchange chromatography using 12 mL BioRad Poly Prep columns filled with 1 mL Dowex AG1-X8 resin (200-400 mesh). Matrix elements (including Ni) were eluted with 6 mL 6 mol/L HCl and collected in Savillex® Teflon beakers. This fraction was dried down and redissolved in 0.5 mL 3 mol/L HNO₃ for the bulk solution nebulization analyses.

The Ni fractions were diluted to ~5 µg/mL Ni in 3% HNO₃ solution and doped with ~4 µg/mL Cu (NIST C 125-1) which was used for instrumental mass bias correction.

4.2 Bulk solution nebulization MC-ICP-MS

Nickel isotope analyses were performed in high mass resolution mode ($M/\Delta M \approx 6000$, 5-95 % peak flank width definition; (Weyer and Schwieters, 2003)) using a Thermo Scientific Neptune Plus MC-ICP-MS. This mass resolution provides sufficiently wide plateaus to analyze Ni apart from any oxide or nitride interferences (Fig. S1). The MC-ICP-MS was equipped with an ESI PFA-ST nebulizer (uptake rate of 100 µL/min, Elemental Scientific, Omaha, NE, USA), a quartz glass spray chamber (double pass Scott design), and a Ni H-type skimmer cone in combination with a Ni sampler cone.

Faraday cups were positioned for simultaneous detection of ⁵⁷Fe, ⁵⁸Ni, ⁶⁰Ni, ⁶¹Ni, ⁶²Ni, ⁶³Cu, and ⁶⁵Cu. ⁵⁷Fe (Tab. S1) was monitored to correct for the isobaric interference of ⁵⁸Fe on ⁵⁸Ni. Instrumental mass bias was monitored by concurrent determination of the Cu isotope composition (reversed to e.g., (Bigalke et al., 2010; Lazarov and Horn, 2015) who used a Ni standard to correct for instrumental mass bias during Cu isotope analyses) by adding a Cu standard solution (NIST C 125-1) to the sample solutions prior to analyses. Iron could also be

Part I: *In situ* Ni isotope analysis via fsLA-MC-ICP-MS

used for instrumental mass bias correction, in theory. However, many terrestrial and extraterrestrial samples, including the materials examined in this study, contain high amounts of Fe. This would require extensive chemical separation of Ni and Fe, which is possible for solution analyses, however, not for laser ablation analyses. Thus, Cu was chosen as mass bias monitor, which is a trace element in most geo-materials. Nickel isotope measurements were carried out with a sample-standard bracketing protocol using the NIST SRM 986 Ni standard and mass bias correction was calculated with the exponential law. For all solution nebulization analyses delta values ($\delta^{62}\text{Ni}$) were determined with the following equation:

$$\delta^{62}\text{Ni} = \left[\left(\frac{\left(\frac{^{62}\text{Ni}}{^{60}\text{Ni}} \right)_{\text{sample}}}{\left(\frac{^{62}\text{Ni}}{^{60}\text{Ni}} \right)_{\text{SRM986}}} \right) - 1 \right] * 1000 \quad (1)$$

A signal of ~19 V on ^{58}Ni was achieved for a ~5 $\mu\text{g/mL}$ Ni solution and ~17 V on ^{63}Cu for a Cu concentration of ~4 $\mu\text{g/mL}$. Each measurement consisted of 100 cycles with an integration time of ~2 s. The internal precision of a single analysis (2SE, n=100) was always better than 0.02 ‰, the repeatability of individual samples during one analytical session was always better than 0.05 ‰ (2 SD, n=4).

4.3 *In situ* Ni isotope determinations by fs-LA-MC-ICP-MS

In situ analyses of Ni isotope concentrations were performed using the Thermo Scientific Neptune Plus as described above which was connected to a Spectra-Physics Solstice femtosecond laser ablation system. Table S2 shows the instrumental parameters of the Neptune Plus. A Ni X-type skimmer cone was used in combination with a Ni Jet sampler cone to enhance intensities as the investigated Ni-bearing steels, D-184.1 and NIST RM 1226, have relatively low Ni concentrations of only 3.3 wt% and 5.8 wt%, respectively. Additional 10% signal increase was achieved by using a 0.8 mm copper spacer (see Fig. S2).

Faraday cup configurations (Table S1), interference correction, and instrumental mass discrimination corrections were the same as for solution analyses. For mass bias correction, a Cu standard solution (NIST C-125-1) was added to the system with a 100 $\mu\text{L/min}$ capillary connected to a glass spray chamber via an ESI PFA-ST nebulizer (Elemental Scientific, Omaha, NE, USA). A signal of ~27 V on ^{63}Cu was achieved for a solution with ~1 $\mu\text{g/mL}$ Cu. The solution signal gives higher intensities than in bulk solution measurements, as the cone assembly is different between the two analytical procedures (Jet sample cone and X skimmer-cone for LA; standard sample cone and H skimmer cone for bulk solution).

Part I: *In situ* Ni isotope analysis via fsLA-MC-ICP-MS

The femtosecond laser ablation system, including the ablation cell and the stage/visualization system, and respective instrumental parameters are identical to those described in (Horn et al., 2006; Horn and von Blanckenburg, 2007; Oeser et al., 2014; Lazarov and Horn, 2015)

All analyses on the Ni-bearing steels and the Ni-rod were carried out in raster mode and consist of one block with 180 cycles and 1 s integration time per cycle. Scanning speed was 15 $\mu\text{m/s}$. The first 30 cycles were measured without a signal from laser ablation and were used for blank correction. A signal of $\sim 5\text{-}7$ V on ^{60}Ni was achieved with the laser for the various samples. For the Ni-steels a beam diameter of ~ 45 μm was used, for pure Ni the diameter had to be smaller (~ 30 μm) to get a signal similar to that of the Ni-steels. Moreover, the laser repetition rate had to be adjusted for the different Ni concentrations in the samples in order to achieve similar ion beams (BAM ≈ 30 Hz, NIST ≈ 17 Hz, Ni-rod ≈ 2 Hz). The Ni-rod and D-184.1 were analyzed relative to NIST RM-1226. $\delta^{62}\text{Ni}$ values were re-calculated relative to NIST SRM 986 with the following equation :

$$\delta^{62}\text{Ni}_{\text{sample/SRM986}} = \delta^{62}\text{Ni}_{\text{sample/RM1226}} + \delta^{62}\text{Ni}_{\text{RM1226/SRM986}} \quad (2)$$

5 IN SITU ISOTOPE ANALYSES OF METEORITES

We analyzed a kamacite-taenite interface (Fig. 1) *in situ* for its Fe and Ni isotope compositions in the IAB-MG iron meteorite Canyon Diablo.

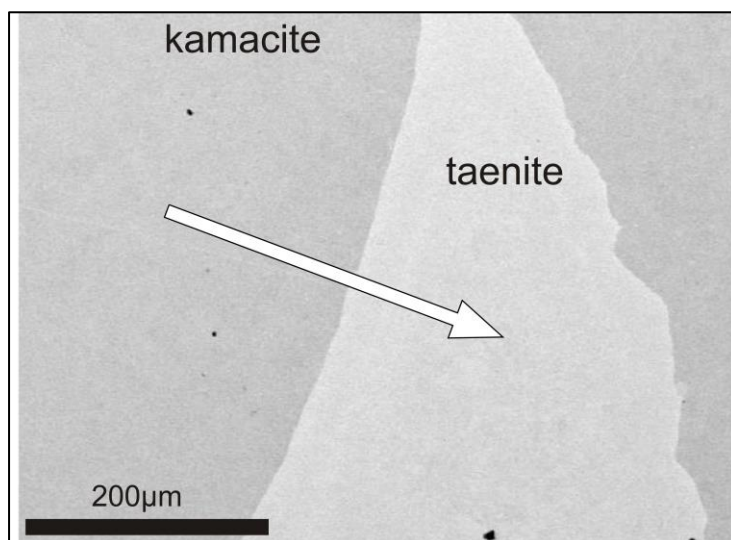


Figure 1: BSE of the examined kamacite-taenite interface. The arrow indicates the direction of the measured profile.

The element concentrations were analyzed with a Cameca SX 100 electron microprobe in Hannover. Iron isotope analyses were carried out using the set up described in (Horn et al., 2006; Oeser et al., 2014). A nickel standard sample cone and a skimmer H-cone were used. A solution with 3 $\mu\text{g/mL}$ Ni (NIST SRM-986) was added for mass bias correction (Oeser et al., 2014). The measured $^{60}\text{Ni}/^{58}\text{Ni}$ was used to perform a mass bias-corrected interference

Part I: *In situ* Ni isotope analysis via fsLA-MC-ICP-MS

correction for the ^{54}Cr interference on ^{54}Fe , which is based on the measured ^{52}Cr signal. This mass bias-corrected interference correction is necessary if the Fe/Cr of the sample is lower than 260 (see example below). For such samples, omitting the mass bias-corrected interference correction would lead to a significant underestimation of the contribution of ^{54}Cr on the total signal on mass 54, i.e. the effect on the determined $^{56}\text{Fe}/^{54}\text{Fe}$ would be larger than 0.1 ‰ (the precision and accuracy of our method). For example, the analyses of samples with Fe and Cr concentrations of 90 wt% and 3600 ppm, respectively, would yield $^{56}\text{Fe}/^{54}\text{Fe}$ ratios that are 0.105 ‰ too low (assuming an instrumental mass bias of 6.5 ‰) if the interference correction of ^{54}Cr on ^{54}Fe is performed without a mass bias correction for the $^{52}\text{Cr}/^{54}\text{Cr}$ ratio. Additionally, as the analyzed meteorite sample contains 5-35 wt% Ni, mass bias correction of the measured Fe isotope ratios was performed offline, applying an interpolation of the Ni isotope ratios that were measured during the Fe background measurement (first 30 cycles measured without laser ablation) of the current analysis and those measured during the Fe background measurement of the following analysis. This means a mean β -value is calculated for the background analyses of the recent analysis and the following one. β represents the mass bias fractionation coefficient and is calculated as follows:

$$\beta_{\text{Ni}} = \ln \left(\frac{\left(\frac{60}{58}\right)_t}{\left(\frac{60}{58}\right)_m} \right) / \ln \left(\frac{M_{60\text{Ni}}}{M_{58\text{Ni}}} \right) \quad ((3) \text{ according to the exponential law})$$

Where $(60/58)_t$ is the true $^{60}\text{Ni}/^{58}\text{Ni}$ ratio and $(60/58)_m$ is the measured $^{60}\text{Ni}/^{58}\text{Ni}$ ratio.

It is assumed that the β -value changes linearly with time and an individual β -value was calculated from that trend to be applied to each cycle of an analysis. Measurements of several Fe-Ni-metal grains with varying Ni concentrations and Ni isotope compositions showed that this interpolation is advantageous over online mass bias correction for metal grains with Ni contents higher than ~7 wt% and a Ni isotope composition that differs by at least ~1.5 ‰ from that of NIST SRM-986 (Fig. S3). The interpolated Ni mass bias was also applied to the measured Fe isotope ratios, though this does not improve the reproducibility of the determined $\delta^{56}\text{Fe}$ between the sample in comparison to non-mass bias corrected Fe isotope ratios (both 2SD = 0.1‰ on $\delta^{56}\text{Fe}$ for 26 measurements on Puratronic in-house Fe isotope standard). The major reason to apply the interpolated Ni mass bias was its applications for the mass bias correction of the Cr interference correction (see above). In particular, if samples have unknown Ni isotope composition, we recommend to perform this interpolation method for all samples that contain Ni as a major element (in a % level).

The setup for *in situ* Ni isotope analyses was as described above. A long traverse of ~200 μm was analyzed across the kamacite-taenite interface with a laser scan speed of 3 $\mu\text{m}/\text{s}$ and a spot size of ~40 μm . The integration time of each cycle was 0.26 s. To get a delta-value

Part I: *In situ* Ni isotope analysis via fsLA-MC-ICP-MS

for every 10 μm , the mean $^{62}\text{Ni}/^{60}\text{Ni}$ ratio was determined for every period of 13 cycles and the $\delta^{62}\text{Ni}$ was calculated by using the mean $^{62}\text{Ni}/^{60}\text{Ni}$ of the bracketing standards that were analyzed before and after the kamacite-taenite traverse.

Table 1: Results of the solution nebulization MC-ICP-MS analyses.

	sample	$\delta^{62}\text{Ni}$ [‰] rel to SRM 986	2SD in ‰	n
solution	Ni-ICP	-0.41	0.04	2
	NIST 1226 Chip 1	-0.28	0.01	4
	NIST 1226 Chip 2	-0.28	0.02	4
	NIST 1226 Chip 3	-0.30	0.01	4
	NIST 1226 Chip 4	-0.27	0.00	4
	NIST 1226 mean	-0.28	0.02	16
	BAM D 184-1	0.12	0.02	4
	Ni-rod	-0.26	0.04	4

6 RESULTS AND DISCUSSION

6.1 Sample homogeneity

In order to assess the suitability of the investigated metals as Ni reference material, they have been checked for their isotopic homogeneity. For the NIST RM-1226 (with a size of $\sim 3 \times 5$ mm), raster scans on different positions were analyzed in bracketing with each other, measuring one of the rasters twice to imitate a bracketing standard (see Fig. 2a for locations). Each raster had a size of about 200×100 μm and was scanned with 15 $\mu\text{m}/\text{s}$. One measurement consisted of 100 cycles with an integration time of ~ 2 s/cycle.

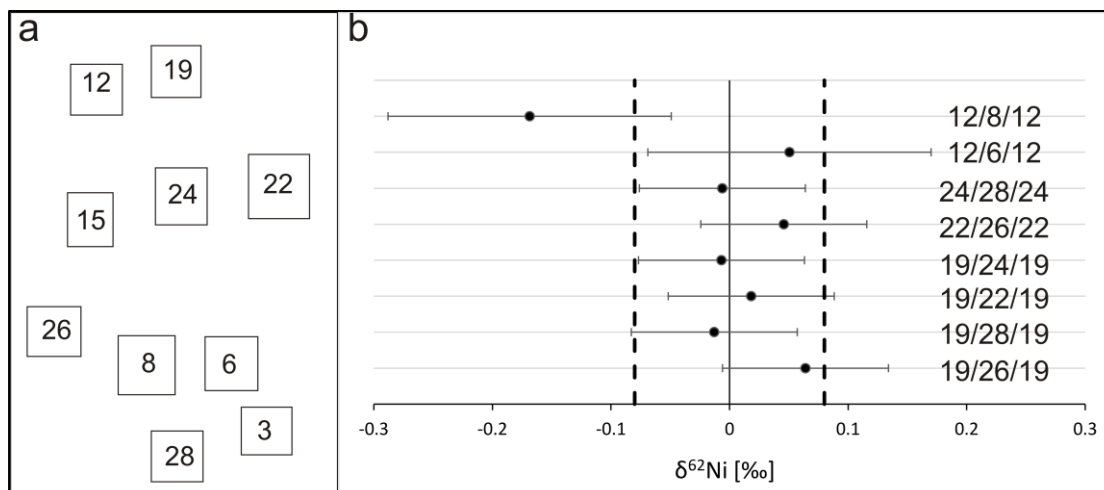
Part I: *In situ* Ni isotope analysis via fsLA-MC-ICP-MS

Figure 2: a) Schematic draw, displaying the positions of the raster-mode Ni isotope analyses on NIST 1226. The total size of the mounted steel chip is $\sim 3 \times 5$ mm. b) Delta values of the different raster analyses on NIST 1226 measured relative to each other. Numbers indicate the raster numbers measured in bracketing with each other. Dashed lines represent the analytical uncertainty of the presented method. As most individual measurements fall in this range, the standard material can be considered homogeneous. Error bars = $2\sigma = 2 * 1000 * ((SEStd1/62/60NiStd1)^2 + (SEStd2/62/60NiStd2)^2 + (SEsample/62/60Nisample)^2)^{0.5}$.

The Ni-rod is 5 mm in diameter and was analyzed for homogeneity via bracketing of several short laser traverses on opposing locations on the sample with each other (see Fig. 3a for locations). Short lines were measured with 15 $\mu\text{m/s}$, one analysis consisted of 120 cycles with an integration time of 2 s/cycle. Moreover, four long line scans (~ 2 mm length) were performed on this standard. These line scans consisted of 450 and 480 cycles, scan speed was 5 $\mu\text{m/s}$ and integration time of each cycle was ~ 1 s. The mean $^{60}\text{Ni}/^{58}\text{Ni}$ and $^{62}\text{Ni}/^{60}\text{Ni}$ ratios were calculated for every 50 μm ($n=10$ cycles) and with these ratios the $\delta^{60}\text{Ni}$ and $\delta^{62}\text{Ni}$ (see equation 1) for every 50 μm were calculated relative to the mean isotope ratios of the whole analysis ($n \approx 430$ cycles). If the variation in δ -values was below 0.08 ‰ (= external reproducibility of $\delta^{62}\text{Ni}$ of the Ni-rod relative to the NIST RM-1226 metal by laser ablation, see below) the sample can be considered to be homogeneous regarded its Ni isotope composition.

BAM D-184.1 consists of flakes with sizes of up to 1x2 mm. Several of these flakes were analyzed in bracketing with NIST RM-1226. Measurements consisted of 180 cycles with an integration time of each cycle of ~ 1 s, scanning speed was 15 $\mu\text{m/s}$.

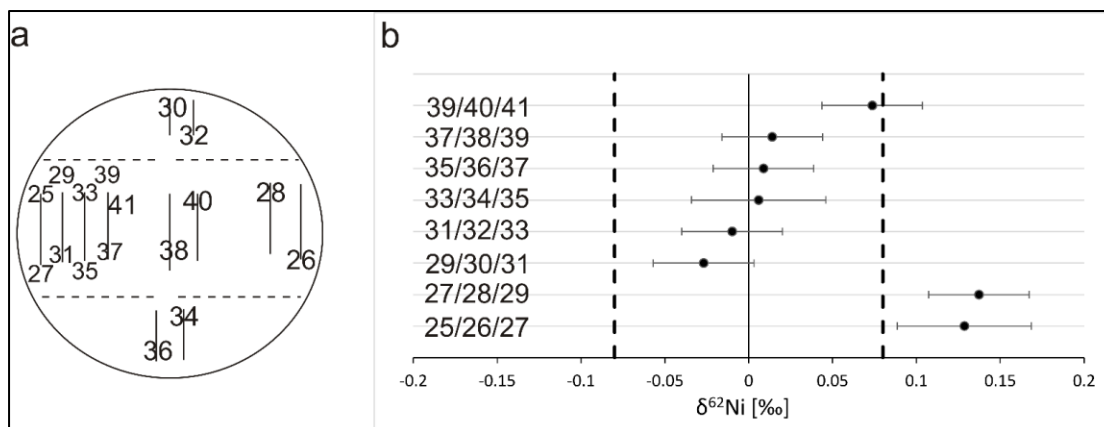
Part I: *In situ* Ni isotope analysis via fsLA-MC-ICP-MS

Figure 3: a) Schematic display of the Ni-rod and the positions of the line scans ($\sim 100\text{-}200\ \mu\text{m}$) performed on it. Dashed lines represent the long traverses ($\sim 2\ \text{mm}$). The diameter of the mounted Ni-rod is $\sim 5\ \text{mm}$. b) Delta values of the different short lines on the Ni-rod, numbers represent the lines measured in bracketing with each other. Dashed lines represent typical analytical uncertainties; i.e. measurements that fall in this range are considered as identical indicating the material being homogeneous. Error bars = 2σ (the uncertainty of a single δ -value calculated with the error propagations of the bracketing standards and of the analyzed sample, see equation in figure caption 2).

The homogeneity test of the Ni-rod yielded mostly identical δ -values for the long and short laser traverses within $0.08\ \text{‰}$ (Figs. 3b and 4). However, two of the δ -values of the Ni-rod differ slightly from the others exceeding the analytical uncertainty (Fig. 3b, 26 and 28). These analyses are located in the same area on the sample (Fig. 3a). So the deviation from the other analytical spots may originate in a minor heterogeneity of the sample or is caused by an artificial offset of the measured Ni isotope ratios, potentially by a change of the gas flow in that area of the sample cell. Such position effects were previously described by (Sio et al., 2013). This may also cause the slight shift towards heavier values (Fig. 3b), as the analyzed lines with heavier isotope composition (e.g., 40) are located closer to the positions of the two outlying measurements (see Fig. 3a). Nonetheless, the Ni-rod can be considered as overall isotopically homogeneous within the uncertainty on a μm to mm scale. This is confirmed by the Ni isotope compositions of the long traverses shown in Figure 4, as the vast majority of the analyses agree with each other, within their individual uncertainties. The raster analyses of opposing positions on NIST 1226 also reveals homogeneous δ -values with a variability below $0.08\ \text{‰}$ (Fig. 2). The Ni-rod was analyzed in two different sessions against NIST RM-1226 with a reproducibility of $\sim 0.08\ \text{‰}$ (2SD, $n=7$, Table S3). Assuming that none of the observed variations results from sample heterogeneities, this value can be considered as the precision of our method. Various flakes of BAM D-184.1 were measured repeatedly against NIST RM-1226 via fs-LA-MC-ICP-MS over a period of twelve months, showing that the combined effect of long term reproducibility and potential isotopic variations among different flakes of BAM D-184.1 is smaller than $0.09\ \text{‰}$ (2SD, $n=38$, Table S3). This variability is very similar to that observed for repeated analyses of Ni rod against NIST RM-1226 and thus within analytical

Part I: *In situ* Ni isotope analysis via fsLA-MC-ICP-MS

uncertainty. Accordingly, BAM D-184.1 can also be considered to be homogenous (Fig. 5). These long term reproducibility values, as achieved for the analyses of the Ni rod and BAM D-184.1 relative to NIST RM-1226 are in good agreement with the precision that is typically achieved for *in situ* stable isotope analyses by fs-LA-MC-ICP-MS (≈ 0.1 ‰) (Horn et al., 2006; Steinhoefel et al., 2009; Oeser et al., 2014; Lazarov and Horn, 2015).

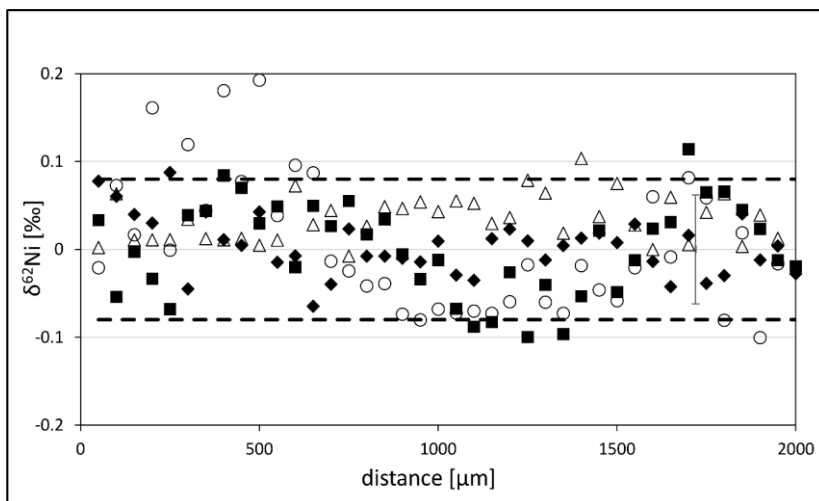


Figure 4: Delta values of the long traverses on the Ni-rod plotted against the distance of the traverses. Squares, diamonds, triangles and circles indicate the four different traverses. Dashed lines represent the analytical uncertainty of the presented method. As most individual measurements fall in this range, the rod can be considered homogeneous. The error bar is the mean 2SE of one individual analyses ($n=10$ cycles).

6.2 Comparison of bulk solution and laser ablation analyses

The results of the bulk solution nebulization analyses give identical values for all four analyzed chips of NIST RM-1226 (-0.28 ‰ in average, $2SD = 0.02$ ‰ for $n=16$, see Table 1). The $\delta^{62}\text{Ni}$ (-0.26 ‰) of the Ni-rod agrees within uncertainties with that of NIST RM-1226. The flakes of D-184.1 are isotopically heavier than NIST SRM 986 ($\delta^{62}\text{Ni} = 0.12$ ‰, Table 1).

Table 2: Mean values of fs-LA-MC-ICP-MS analyses relative to NIST RM 1226 and re-calculated to NIST SRM 986, derived from individual values in Table S3.

	sample	$\delta^{62}\text{Ni}$ [‰] rel to SRM 986	$\delta^{62}\text{Ni}$ [‰] rel to RM 1226	2SD in ‰	Ni conc	n
Laser	BAM D 184-1	0.09	0.37	0.08	3.3 wt%	38
	Ni-rod	-0.26	0.02	0.08	99.9 wt%	7

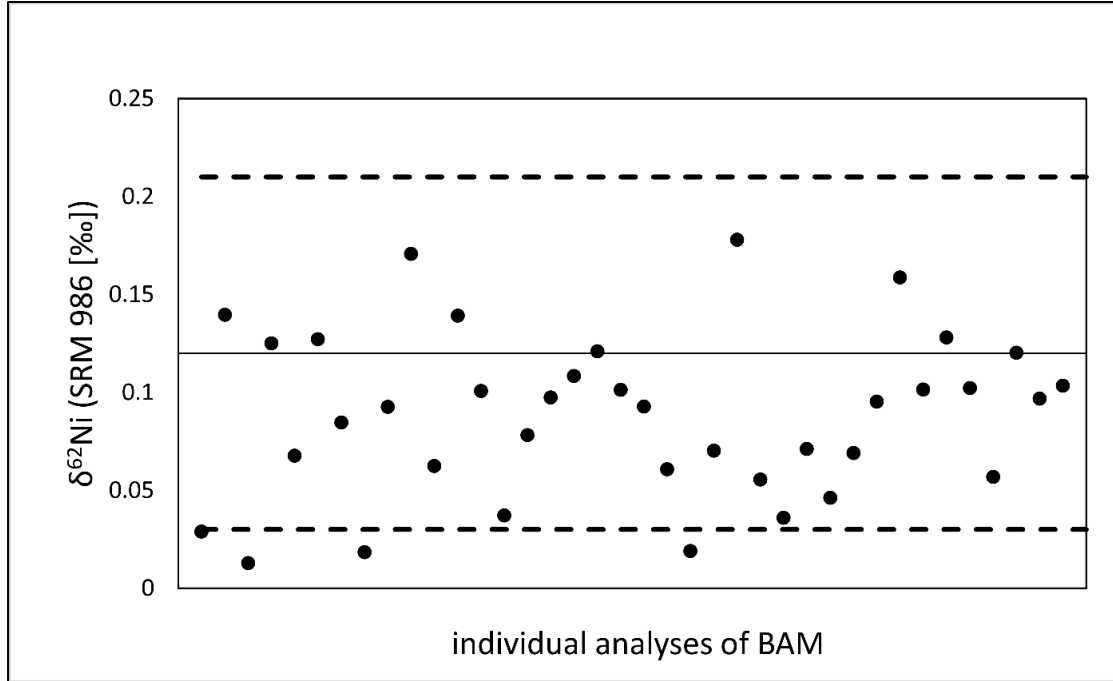
Part I: *In situ* Ni isotope analysis via fsLA-MC-ICP-MS

Figure 5: $\delta^{62}\text{Ni}$ values of individual laser ablation analyses of BAM D-184.1 against NIST-RM1226, re-calculated for standard SRM 986. The solid line in the middle represents the Ni isotope composition of D-184.1 derived from bulk solution analyses (0.12 ‰), the dashed lines mark the upper and lower values that lie within the precision (0.08 ‰) with which D-184.1 can be analyzed with the laser. The majority of the analyses lies within these boundaries, thus BAM D-184.1 can be considered as being homogenous.

As described above *in situ* isotope analyses of BAM D-184.1 and the Ni-rod were conducted by fs-LA-MC-ICP-MS and reported relative to NIST RM-1226. In order to compare the results of the laser ablation analyses for BAM D-184.1 and the Ni-rod, with those from the bulk solution nebulization analyses, the δ -values were re-calculated relative to NIST SRM 986 with equation (2). Tables 1 and 2, and Figure 6 show that the results of the LA-MC-ICP-MS analyses are in excellent agreement with those of the bulk solution nebulization analyses. Considering the results of solution nebulization analyses, which have a higher precision, as the true Ni isotope composition of the samples, may provide an estimate for the accuracy of the delta values derived from LA-MC-ICP-MS measurements. Both, the *in situ* $\delta^{62}\text{Ni}$ values for BAM D-184.1 and the Ni-rod agree within their precision, as determined above, with the values determined by solution nebulization analyses. The total analytical uncertainty on the $\delta^{62}\text{Ni}$ values analyzed with fs-LA-MC-ICP-MS for the presented Ni-bearing metals can be calculated with the following equation:

$$2S_{\text{LA}} = 2 * \sqrt{(S_{\text{rs}})^2 + (S_{\text{rl}})^2} \quad (4)$$

Part I: *In situ* Ni isotope analysis via fsLA-MC-ICP-MS

where S_{rs} is the reproducibility (1SD) of NIST RM-1226 from solution analyses, and S_{fl} is the reproducibility (1SD) of the Ni-bearing metals measured via laser ablation. This gives a total analytical uncertainty on $\delta^{62}\text{Ni}$ of $\sim 0.08\text{‰}$.

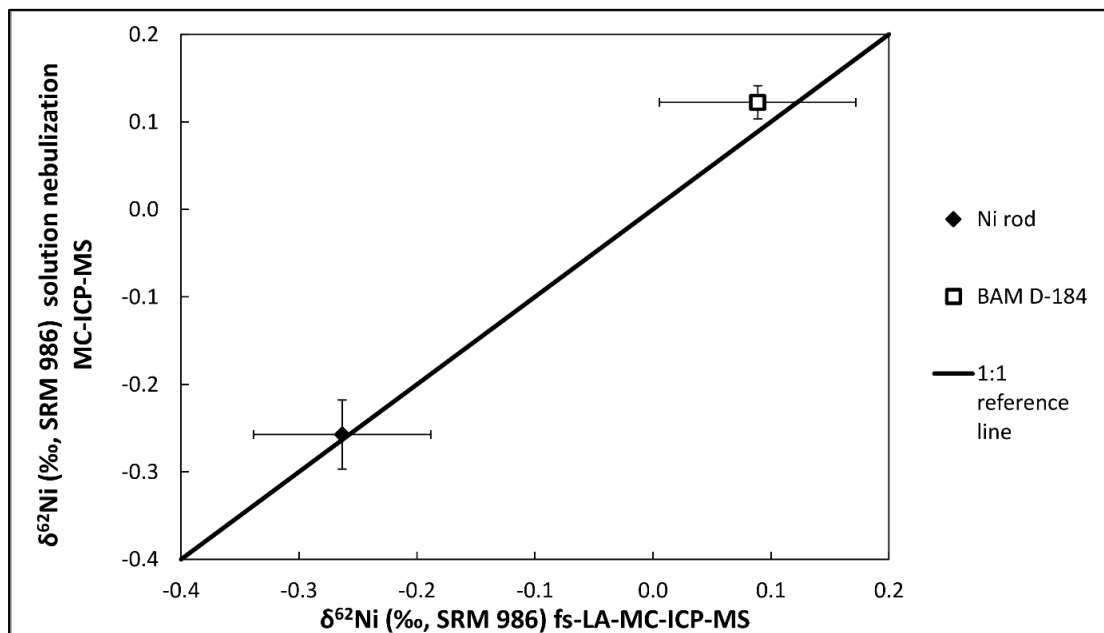


Figure 6: Results of solution MC-ICP-MS and LA-MC-ICP-MS for the Ni rod and BAM D-184 plotted against each other. Data for the Ni-rod (black diamond) and for BAM-D184.1 (white square) plot within analytical uncertainties on a 1:1 reference line. Error bars = 2SD.

6.3 Application to Kamacite-Taenite interfaces in iron meteorites

Figure 7 displays the chemical profile that was measured over a kamacite-taenite boundary. The Ni concentration in kamacite ($\sim 5\text{-}6\%$) decreases towards the interface. Ni concentrations in taenite are always $> 15\%$ and the highest Ni content ($\sim 30\text{ wt}\%$) was analyzed at the very border of the two phases. In general, kamacite has a heavier Ni isotope composition (on average $\delta^{62}\text{Ni} = 1.42 \pm 0.23\text{‰}$) than taenite (on average $\delta^{62}\text{Ni} = 0.34 \pm 0.5\text{‰}$). The relative variations in Fe isotope ratios are vice versa, on average $\delta^{56}\text{Fe} = -0.12 \pm 0.14\text{‰}$ in kamacite and $\delta^{56}\text{Fe} = 0.33 \pm 0.05\text{‰}$ in taenite. Differences in the isotope composition between the two phases were already previously reported for Ni (Cook et al., 2007) and for Fe (Poitrasson et al., 2005; Horn et al., 2006). However, these measurements (Poitrasson et al., 2005; Cook et al., 2007) were performed from kamacite and taenite bulk solutions after micro-sampling and were, because of the respective lower spatial resolution, unable to resolve any isotopic zoning. The isotopic profile measured for the kamacite-taenite interface with LA-MC-ICP-MS (Fig. 7) reveals that the Fe isotope composition in the kamacite becomes heavier towards the interface.

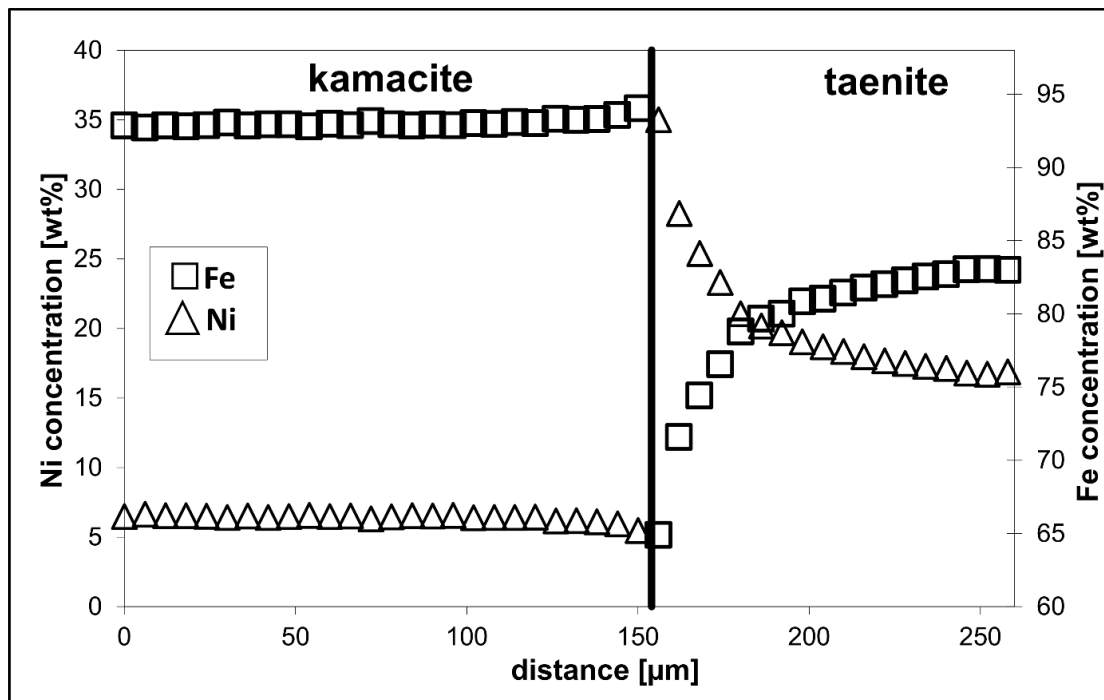
Part I: *In situ* Ni isotope analysis via fsLA-MC-ICP-MS

Figure 7: Chemical profile of the kamacite-taenite interface. Iron (white squares) and Ni concentrations (white triangles) plotted against the length of the profile.

Within the taenite Fe isotopes are slightly heavier than in kamacite (on average ~ 0.4 ‰), with the heaviest composition at the very border of the two phases (Fig. 8). Compared to Fe isotopes, zoning of Ni isotope compositions is generally stronger, in particular in taenite, where $\delta^{62}\text{Ni}$ increases from light compositions (~ 0.03 ‰) in the center of the taenite to a value of ~ 1.03 ‰ at the very border to kamacite. In kamacite, Ni isotopes are also zoned and show the heaviest compositions on the very border to taenite (~ 1.69 ‰) (Fig. 8). These isotope signatures can be explained by the exchange diffusion of Fe and Ni (Dauphas, 2007) that takes place during formation of kamacite from taenite. During replacement of taenite by the Ni-poor kamacite, Fe enters the newly formed kamacite while Ni stays in the taenite. As a result of decreasing temperatures during cooling of the meteorite parent body, taenite is progressively replaced by kamacite, leading to a moving kamacite-taenite boundary. This process results in progressive Ni enrichment in the remaining taenite, in particular in the taenite rim, generated by back-diffusion of Ni from the newly formed kamacite, while Fe diffuses out of taenite. As light isotopes diffuse faster than heavy ones (Richter et al., 1999), this leaves taenite with generally lighter Ni isotope compositions and heavier Fe isotope compositions compared to kamacite (Cook et al., 2007), as observed in our example. In the taenite, Ni continuously diffuses from the enriched rim towards the center of the taenite, and Fe towards the rim, resulting in further enrichment of light Ni isotopes and heavy Fe isotopes in the taenite core. If the temperature becomes low enough, and diffusion slow, the Ni at the taenite rim does not equilibrate anymore with the inner parts of the taenite, resulting in the preservation of a

Part I: *In situ* Ni isotope analysis via fsLA-MC-ICP-MS

concave-up Ni concentration profile (Fig. 7) and of light Ni isotopes in the center of taenite relative to the interface and kamacite (cf. (Richter et al., 2009)). Similarly, the kamacite rim, highly depleted in light Ni isotopes, does not equilibrate anymore with its center, resulting in the heaviest Ni isotope compositions at the kamacite rim. Due to the generally higher concentration of Fe compared to that of Ni, in both kamacite and taenite, the Fe isotope compositions in both phases is much less affected by these diffusive processes for mass balance reasons, i.e. the maximum Fe isotope fractionation in this profile does not exceed 0.7 ‰ in $\delta^{56/54}\text{Fe}$ (compared to ~ 1.9 ‰ in $\delta^{62/60}\text{Ni}$). Our observations thus provide the first *in situ* isotopic evidence for significant diffusive processes during the formation of kamacite out of taenite that was previously drawn from chemical zoning and bulk isotope compositions, alone (Reed, 1965; Narayan and Goldstein, 1985; Brearley and Jones, 1998; Poitrasson et al., 2005; Cook et al., 2007; Dauphas, 2007, and references therein).

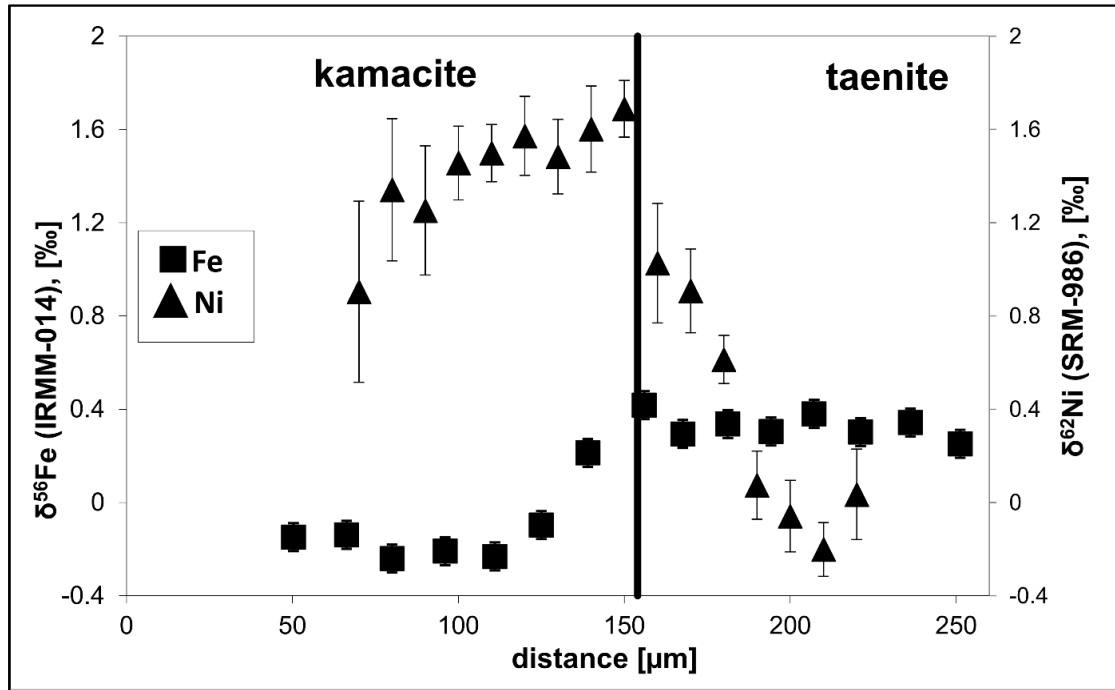


Figure 8: Isotopic profile of the kamacite-taenite interface. Iron (black squares) and Ni isotope composition (black triangles) plotted against the length of the profile. Error bars = 2σ .

7 CONCLUSIONS

This study presents for the first time a method to measure *in situ* high-precision Ni isotope compositions of metal with fs-LA-MC-ICP-MS. Both, the precision and accuracy of the *in situ* analyses is better than 0.1 ‰ (2SD) for $\delta^{62}\text{Ni}$, as demonstrated by replicate measurements of homogenous standard material, by solution and with LA-MC-ICP-MS. The presented method can be applied, e.g., for the analyses of small metal grains in meteorites that cannot be sampled otherwise. Furthermore, isotopic zoning of such metals can be resolved on

Part I: *In situ* Ni isotope analysis via fsLA-MC-ICP-MS

a scale of a few tens of μm . As shown in our example of a kamacite-taenite interface, the new analytical technique allows, in combination with other isotope systems such as Fe, to draw additional constraints on the formation processes of chemical and isotopic zoning. It may thus be applied to unravel processes such as chemical or thermal diffusion (Oeser et al., 2015) or condensation (Zipfel and Weyer, 2007).

Part II: Origin of metal from CB chondrites in an impact plume - A combined study of Fe and Ni isotope composition and trace element abundances

A modified version of this chapter was submitted to *Geochimica et Cosmochimica Acta*:
Weyrauch M., Zipfel J., and Weyer S. Origin of metal from CB chondrites in an impact plume
– A combined study of Fe and Ni isotope composition and trace element abundances.

1 ABSTRACT

The formation processes of the unusually metal-rich CB chondrites are a matter of debate. It is widely accepted that metal grains have formed by condensation. However, it is controversially discussed whether they condensed directly from the solar nebula or from an impact-induced vapor plume. In this study, we present high precision Fe and Ni isotope and trace element composition of zoned and unzoned metal grains from the CB_b chondrites Hammadah al Hamra 237, QUE 94411, and MAC 02675, and the CH/CB_b breccia Isheyev and unzoned metal from the CB_a chondrites Bencubbin, Gujba, and NWA 4025. Data were obtained using *femtosecond* laser ablation (multicollector) inductively coupled plasma mass spectrometry (*fs*-LA-(MC)-ICP-MS). Zoned metal grains from CB_b meteorites generally display parallel profiles of Ni and Fe isotope compositions with very low $\delta^{56}\text{Fe}$ and $\delta^{60}\text{Ni}$, and elevated concentrations of refractory siderophile elements in their cores. These findings are consistent with dominantly kinetic isotope- and trace element fractionation during condensation from a confined and fast cooling gas reservoir. Tungsten and Mo are frequently depleted relative to other refractory elements, particularly in zoned metal grains, which is suggestive for elevated oxygen fugacities in the gas reservoir. Such conditions are indicative for the formation of these metal grains during an impact event.

Compared to zoned metal, unzoned metal grains are isotopically more homogeneous and more similar to the heavier rims of the zoned metal grains. This indicates that they formed

Part II: Origin of metal from CB chondrites

under different conditions than the zoned metals. i.e. in a more slowly cooling environment. However, several unzoned grains still display significantly variable and correlated $\delta^{56}\text{Fe}$ and $\delta^{60}\text{Ni}$, suggesting their formation was related to that of the zoned metal grains. The kinetic fractionation-dominated isotopic signatures of the zoned metal grains strongly point to their formation during fast cooling, as may be expected for the exterior envelope of an impact plume. In contrast, the more homogenous isotopic signatures of the unzoned metal grains are more consistent with dominantly equilibrium-like isotope fractionation during condensation, as may be expected for the interior of an impact plume. In this scenario, the isotopically heavier rims of the zoned grains are best explained by a depletion of the outer plume gas reservoir in refractory elements and light isotopes. Accordingly, these findings indicate that zoned and unzoned metal grains likely formed during the same event. The compositional differences among individual unzoned metal grains, but also within some of the zoned grains, indicate turbulent gas mixing, also including movement of metals during their formation, between inner and outer regions of the impact plume.

2 INTRODUCTION

CB chondrites are unusually metal-rich chondrites with metal contents between ~60 and ~80 vol% (Weisberg and Prinz, 1999). Due to similarities, such as a high metal content, and N- and O-isotope composition, they are assorted to the CR-clan together with CH and CR chondrites (Krot et al., 2002). CB chondrites are especially primitive in their bulk chemical composition (Campbell et al., 2002) which makes them interesting research objects. Their pristine character may give insights into their formation processes and origin. These meteorites are not only special among the carbonaceous chondrites due to their high metal abundance and lack of matrix, but also because of their strong excess in refractory elements relative to solar values (Zipfel et al., 1998).

Additionally, the fine-grained CB_b chondrites have abundant chemically zoned Fe-Ni-metal grains (Weisberg and Prinz, 1999; Meibom et al., 2000). While Ni and Co concentrations are enriched in cores relative to rims, Fe and Cr show reverse zoning to that of Ni and Co (Meibom et al., 1999; Weisberg and Prinz, 1999). Refractory siderophile trace elements (e.g. Os, Ir, Ru) follow the zoning of Ni and Co (Campbell et al., 2000; Campbell et al., 2001). Moreover, these grains are isotopically zoned. Iron isotope analyses show lower $\delta^{56}\text{Fe}$ in metal cores than in rims (Zipfel and Weyer, 2007; Richter et al., 2014). Nickel isotope composition was also examined by ion microprobe analyses of some grains (Alexander and Hewins, 2004; Richter et al., 2014). Results of these studies have large analytical uncertainties, yet indicate

Part II: Origin of metal from CB chondrites

that Ni isotope composition change, like Fe isotopes, along a similar zoning profile. Both elemental and isotopic zoning suggest a condensation origin for the metals as elemental patterns follow the cosmochemical behavior of the elements (Campbell et al., 2005) and condensation of light isotopes prior to heavy ones is expected during kinetic isotope fractionation (Young et al., 2002). The majority of the metal grains in CB chondrite is unzoned. Two different settings are being discussed for formation of zoned metal in CB chondrites by condensation. One study assumes condensation occurred within the solar nebula (Weisberg and Prinz, 1999) while others assume condensation occurred within an impact induced vapor plume (Wasson and Kallemeyn, 1990; Kallemeyn et al., 2001; Fedkin et al., 2015). Findings that chondrules (Krot et al., 2005; Bollard et al., 2015) from CB chondrites are younger than those of other meteorites, and that the Fe content in chondrules is consistent with condensation under oxidizing conditions support the impact model (Krot et al., 2000).

In this study, we examine profiles of Fe and Ni isotope as well as trace element compositions of the zoned metal grains in order to comparatively discuss and elucidate models of their formation by condensation. Isotopic and chemical compositions of zoned and unzoned grains are compared in order to discuss their relation to each other and to assess the possibility of their formation during one and the same process. Combining these data, we address the question whether the metal grains more likely formed in the solar nebula or an impact plume and we develop potential scenarios for their formation.

3 SAMPLES AND METHODS

In this study we examined three CB_a (Bencubbin, Gujba, NWA 4025), three CB_b chondrites (Hammadah al Hamra 237 (HaH237), QUE 94411, MAC 02675), and the CH/CB_b breccia Isheyev. Metal grains were studied in the polished sections of Bencubbin (6 grains), Gujba (5 grains), NWA 4025 (8 grains), HaH237 (10 grains), QUE 94411 (9 grains), Isheyev (8 grains), and MAC 02675 (12 metal grains). The Antarctic samples (MAC 02675 and QUE 94411) were provided by the Meteorite Working Group. All CB_a chondrite samples, HaH 237, and the CH/CB_b breccia Isheyev belong to the collection of the Senckenberg Forschungsinstitut und Naturmuseum Frankfurt.

3.1 Petrography of the examined meteorites

In the following the examined meteorites are being described with focus on the metal features, as those are the main subject of this study. The CB chondrites are subdivided into two subgroups, the CB_a and the CB_b chondrites. Meteorites of the CB_a group are characterized by up to cm-sized metal aggregates and large (also up to cm-sized) silicate clasts ((Weisberg and

Part II: Origin of metal from CB chondrites

Prinz, 1999; Weisberg et al., 2001; Rubin et al., 2003)). CB_b chondrites are more fine-grained than CB_a samples with a mean grain size of about 200 μm (Krot et al., 2002). Another difference is that CB_b chondrites contain chemically zoned metal grains, which are absent in CB_a chondrites (Weisberg and Prinz, 1999; Weisberg et al., 2001). Moreover, CB, both CB_a and CB_b , chondrites lack matrix surrounding chondrules (Grossman et al., 1988; Krot et al., 2002), but contain so-called hydrated matrix lumps (Meibom et al., 2005).

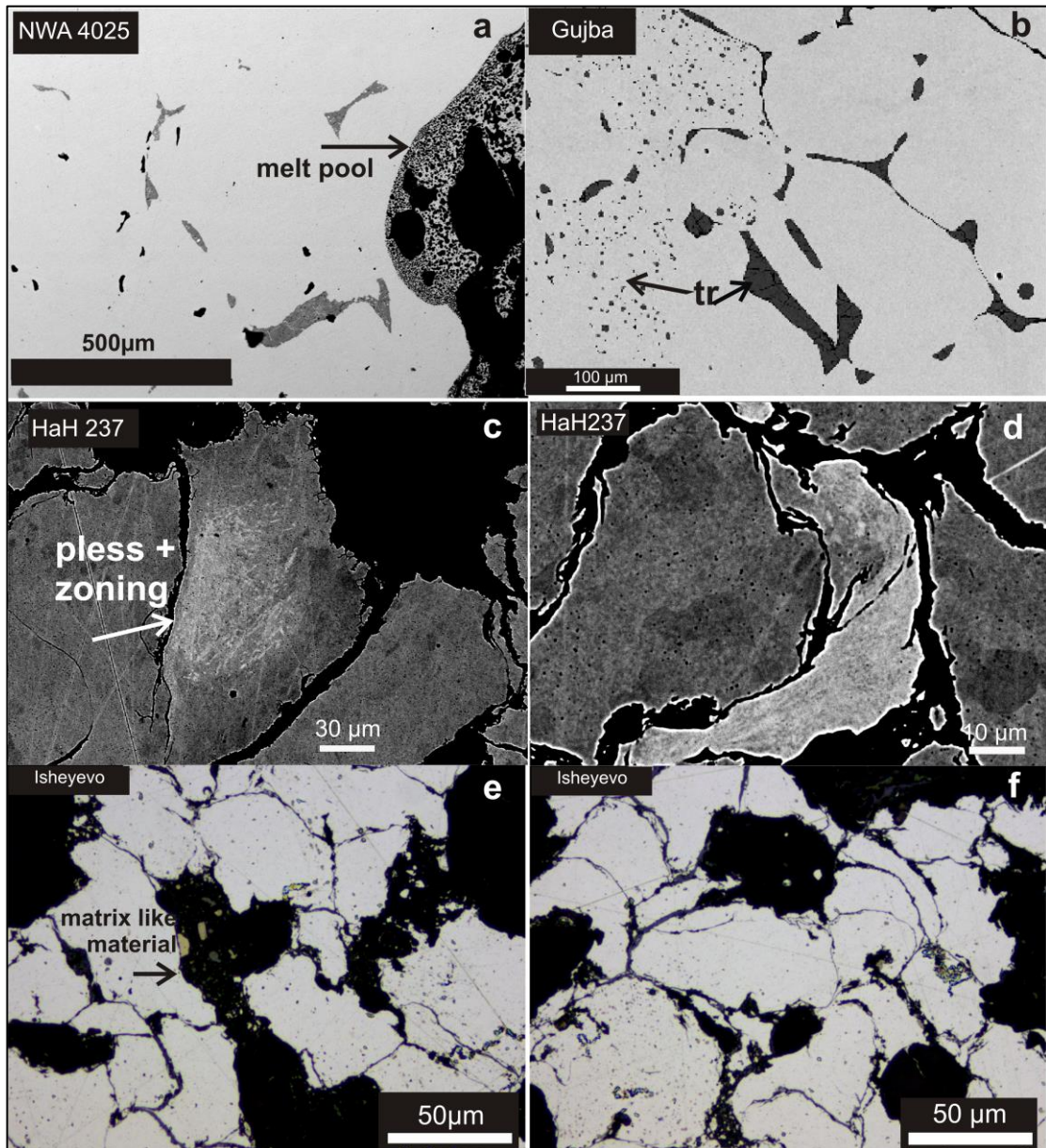


Figure 1: BSE images (c+d) and images in reflected light of textures in CB chondrites. a) Reflected light image of typical shock melt in CB chondrites (here CB_a chondrite NWA 4025). b) reflected light image displaying inner texture of a metal aggregate from CB_a chondrite Gujba. tr = troilite, abundant as blebs within metal or as networks interstitial to metal. c) BSE image of a zoned metal grain broken into two parts. Displaying that the zoning is also split into two parts and a plessitic texture in the core. d) BSE image of the crimped texture of metals in HaH 237. e) reflected light image of Isheyevu, showing the matrix-like material that can be found in CB_b chondrites. f) reflected light image of the texture found in the CB_b lithology of Isheyevu. This is also the typical texture for all CB_b chondrites.

Part II: Origin of metal from CB chondrites

3.1.1 *CB_a Chondrites*

Gujba

Gujba contains several isolated well rounded and slightly elongated metal aggregates of sizes varying between 1.5 mm and ~4 mm. Metal aggregates have a preferred orientation (30° of the mean azimuth (Rubin et al., 2003)). Most of these objects include abundant sulfides within. Troilite occurs in small well rounded blebs (mainly ~10 µm, up to 50 µm) or as a network of long thin lines connected by angles of 120°. Such triple junctions apparently outline grain boundaries of separated Fe,Ni-metal grains within a larger metal aggregate (Fig. 1a and b). Single metals in the so-called aggregates are up to ~550 µm in size. Furthermore, there are some metal grains that appear to be free of sulfides. Interstitial to metal and silicates, Gujba contains melt veins that are rich in silicate and contain small metal nodules. Total metal content in Gujba is 60% (Grossman and Zipfel, 2001).

NWA 4025 and Bencubbin

These two meteorites show essentially the same optical characteristics as Gujba. However, metal and silicate nodules are more fragmented than in Gujba (Rubin et al., 2001). Metal in Bencubbin has a preferred orientation, less than 45 degrees to reference axis (Meibom et al., 2005), similar as for Gujba (Rubin et al., 2003).

3.1.2 *CB_b Chondrites*

Hammadah al Hamra 237

The section examined showed that the majority of the metal grains are fine-grained (30-200 µm), flaky, and apparently crimped and stacked onto each other (Fig. 1b and f). However, there are also well-rounded metal grains that are larger than the rest (up to ~4 mm). Looking at the internal texture of these they show fine, well rounded blebs of sulfide or long thin lines of sulfides, which seem to form borders between separate metal grains. These objects look similar to the metal aggregates found in *CB_a* chondrites (see also (Weisberg et al., 2001; Meibom et al., 2005)). Zoned metal grains can occur in chains or in clusters, but also appear as isolated grains. The modal abundance of zoned metal grains was determined from two Ni element maps, covering an area of 4 mm² each. Zoned metal grains make up 10-18 % of the entire metal fraction of that meteorite. In element mappings, it can be observed that Fe and Ni zoning often follows the crimped outline of the grains (Fig. 1c and d). Moreover, it was revealed that some zoned metal grains have a fine plessitic texture in their center (similar to Fig. 1c). Interstitial to

Part II: Origin of metal from CB chondrites

metal and silicates are abundant shock veins. Some are dominated by silicate melt and others are dominated by metal melt. Further constituents of this meteorite are abundant chondrules, rare Ca-Al-rich inclusions and dark clasts of fine-grained material.

MAC 02675 and QUE 94411

The sections of these meteorites display essentially the same texture and occurrence of phases as was observed for HaH 237. For the section of MAC 02675, also two Ni element mappings, covering 4 mm² and ~2 mm², were evaluated for the modal abundance of the zoned metal grains. In both mappings zoned grains constitute ~about 19 % of the metal fraction.

3.1.3 CH/CB_b breccia Isheyev

Element mappings of the Isheyev section show variable metal contents of 30-60 vol% which is less variable as the range observed by (7-90% in (Ivanova et al., 2008)). Areas with contents of about 60 vol% metal are highly compacted and metals are crimped and stacked onto each other similar to textures in CB_b chondrites. Grain sizes are up to ~300 μm. Evaluation of a Ni element map of Isheyev (5 mm * 5 mm, 25 mm²) revealed that the proportion of zoned metal grains of the total metal is about 9 %. As already described for the CB_b chondrites, zoned metal often appears in clusters or chains, but can also occur as isolated grains. Chondrules are mainly of cryptocrystalline texture and (CC chondrules) typically reach sizes of up to ~100 μm. Rare larger CC chondrules with about 200 μm were observed. These characteristics represent the CB_b lithology, the more dominant one in Isheyev (Ivanova et al., 2008). The CH lithology is embodied by a more silicate-rich lithology. Metal grains are slightly smaller than in the CB_b lithology, and CC chondrules have essentially the same optical characteristics as in the CB_b-like lithology. However, also large silicate clasts of up to 1 mm in diameter occur in the CH lithology. Though there seem to be some features that allow to distinguish between CH and CB_b lithologies, there is no sharp boundary between the two (Ivanova et al., 2008). Both lithologies contain abundant shock veins interstitial to metal and silicate phases. These shock veins can be silicate-rich with small metal nodules inside or metal-rich with small silicate nodules inside. Rare isolated sulfides also appear interstitial to metal and chondrules. Additionally, interstitial to metal and silicates are clasts of very fine-grained material which also contain somewhat larger subhedral crystals with sizes up to 10 μm (Fig. 1e, possibly hydrated matrix lumps (Ivanova et al., 2005; Ivanova et al., 2008)).

3.2 Analytical procedures

Polished sections were examined in reflected light with a Zeiss Axiophot microscope (Frankfurt). Overview photos were taken automatically with a Leica DM4-M microscope and

Part II: Origin of metal from CB chondrites

the analySIS software by Olympus (Hannover). For a first characterization of the mineralogy, samples were investigated with a JEOL JSM-6490 LV scanning electron microscope (SEM) at the Senckenberg Forschungsinstitut in Frankfurt. Analyses and mappings with the SEM were only qualitative. Quantitative analyses were obtained by electron microprobe. EMPA analyses and element mappings were performed on the samples at the Goethe-Universität, Frankfurt am Main, with a JEOL Superprobe JXA-8900.

Quantitative analysis of Si, Fe, Cr, Ni, S, Co, and P in metal was carried out at 20 nA and 20 kV with a focused beam. For most elements, pure element metal standards were used for calibration. Only P, S, and Co were calibrated with KTiO_2PO_4 , FeS, and CoO, respectively. The CITZAF procedure of Armstrong (1995) was applied for matrix correction. Detection limits and measurement time on peak and background are summarized in Table S1. Element mappings for Mg, Fe, Al, Ca, and Ni were performed at 60 nA and 20 kV with a dwelltime of 10 ms and an interval of $3 \times 3 \mu\text{m}$. For calibration the same standards as for quantitative analyses were used. All elements were mapped with WDX detectors.

Some of the samples were mapped and analyzed at the Leibniz Universität Hannover with the same measurement conditions, using a Cameca SX 100. Matrix correction was made according to the PAP procedure (Pouchon and Pichoir, 1984). Standards used were Wollastonite for Si, Apatite Durango for P, Pyrite for S, Cr_2O_3 for Cr, and pure metal for Fe, Ni, and Co. Detection limits and measurement time on peak and background are summarized in Table S1.

Iron and Ni isotopic composition of the metal grains of CB chondrites were analyzed by femtosecond-laser ablation-multicollector-inductively coupled plasma-mass spectrometry (fs-LA-MC-ICP-MS) at the Institut für Mineralogie, Leibniz Universität Hannover. A Thermo Scientific Neptune Plus was connected to a Spectrapysics solstice femtosecond laser ablation system. Machine set up and mass bias correction for Fe isotope analyses was as described in (Horn et al., 2006; Oeser et al., 2014). Analyses were performed as line scans in standard sample bracketing mode.

Nickel isotope compositions were analyzed as described in (Chernonozhkin et al., 2017; Weyrauch et al., 2017). A Cu (0.5 ppm) solution was used for instrumental mass bias correction. Standards used for determination of Ni isotope composition were the Ni steels NIST RM-1226 and BAM D-184.1 with 5.4 wt% and 3.3 wt% Ni, respectively. Ni isotope composition of these steels were determined by MC-ICP-MS solution measurements beforehand. Delta values for Ni isotopes are reported relative to NIST SRM-986.

As most of the investigated metal grains have been analyzed for their Fe- and Ni-isotope, as well as for their trace element compositions, the analyzed area of the commonly small grains was ablated repeatedly. This process was monitored by a Keyence VK-9710K confocal laser

Part II: Origin of metal from CB chondrites

microscope, which was used to determine the shape and depth of the laser ablation craters (Fig. S1) after the different types of analyses (Institut für Bodenkunde, Leibniz Universität Hannover).

Since Fe isotope analyses are performed with small repetition rates of the laser, measuring tracks are only 3-5 μm deep. Similarly, tracks produced during trace element analyses were also only 5-7 μm deep, while the deepest craters of up to 30 μm were generated during Ni analyses for which higher repetition rates were required. We observed that successive analyses (in any order), without re-polishing in between the analyses, generated unreproducible results or small offsets for the measured Fe and Ni isotope composition. We thus decided to perform minor re-polishing ($\sim 10 \mu\text{m}$) between Fe + trace element, and Ni isotope analyses. Because of the low crater depth of the first two measurements, this procedure has only minor effect on the shape of the analyzed zoning profiles.

For both isotope systems analyses yield in accuracy and precision of $\sim 0.1 \%$ (Weyrauch et al., 2017).

For unzoned metals laser traverses were scanned several times with a scanning speed of 15 $\mu\text{m}/\text{s}$. A duration of 180 cycles with an integration time of $\sim 1 \text{ s}$ was chosen for unzoned grains, with ~ 30 cycles of background signal.

For zoned metal grains, lines were placed across single grains and the lengths varied with grain size. For Fe isotope analyses zoned metals were scanned with 1 $\mu\text{m}/\text{s}$ or 2 $\mu\text{m}/\text{s}$. The number of cycles was adjusted to the length of the laser profile and the scanning velocity. Integration time between the cycles was $\sim 1 \text{ s}$. For Ni isotope analyses a scanning speed of 2 $\mu\text{m}/\text{s}$ or 3 $\mu\text{m}/\text{s}$ was chosen which yielded sufficiently high intensities ($^{56}\text{Fe} = 13\text{-}17 \text{ V}$ and $^{60}\text{Ni} = 3\text{-}7 \text{ V}$). Integration time between the cycles was $\sim 0.5 \text{ s}$ or $\sim 0.3 \text{ s}$, respectively. Again, the number of cycles was adjusted to the length of the profile and the scanning velocity. Delta values were calculated using the mean $^{62/60}\text{Ni}$ ratio of 10 cycles (for 1 $\mu\text{m}/\text{s}$ and 2 $\mu\text{m}/\text{s}$) or of 13 cycles (3 $\mu\text{m}/\text{s}$) relative to the mean $^{62/60}\text{Ni}$ ratio of the bracketing standards of an analysis. Hence, a nominal isotope composition for every 10 μm was achieved. Spot size for Fe and Ni isotope analyses was $\sim 35 \mu\text{m}$.

Trace element abundances were also analyzed by fs-LA-ICP-MS. The Spectraphysics Laser system was connected to a Thermo Scientific Element XR. Measurements were performed using a $\sim 30 \mu\text{m}$ laser spot. External standards are the ataxite iron meteorite Lombard, which was shown to be homogenous in chemical composition, and PGE-A (Gilbert et al., 2013). Nickel contents, of the grains as determined by EMPA, were used as internal standard. Data reduction was performed with the Lotus-based spreadsheet program LAMTRACE (Jackson, 2008). Elements analyzed were arranged according to volatility from

Part II: Origin of metal from CB chondrites

Ge, Cu, Au, Fe, Pd, Co, Ni, Pt, Mo, Ru, Ir, W, Os, and to Re. Detection limits and the relative standard deviations (%) are summarized in Table 1.

4 RESULTS

In the following, results of fs-LA-ICP-MS analyses for zoned grains from CB_b chondrites and Isheyevo, and for unzoned grains from both CB_a and CB_b chondrites are described.

4.1 Zoned metal

Six zoned metal grains from MAC 02675 were analyzed for their isotopic and chemical composition. For QUE 94411 and Isheyevo such analyses were performed on four grains each. Additionally, three zoned metals from HaH 237 (CB_b) were examined. For the zoned grains from Isheyevo (which contains CB_b-like and CH-like lithologies) it was only possible to determine the parent lithology for grain Isheyevo_1.5 which stems from the CH-like lithology.

4.1.1 Chemical composition

Similar to earlier findings (Meibom et al., 1999; Weisberg and Prinz, 1999; Campbell et al., 2000; Meibom et al., 2000), we found that most zoned metal grains have higher Ni concentrations in cores than in rims, and that Co and highly refractory elements, such as Ir, Ru, and Os follow this zoning (Figures 2a,b,d,e,g,h), whereas Fe is zoned reversely (Figure 2).

However, not all zoned grains show continuous zoning. Some grains display typical zoning of Fe and Ni in the rim areas but more scattered patterns in the core area (Figure 2d). Trace element analyses in such grains do not reveal such a scattered pattern but have smooth patterns (Fig. 2e). As major elements were measured with EMPA, while trace elements with LA-ICP-MS, the smooth trace element zoning is likely simply a result of the larger spot size of the laser, integrating over the heterogenous chemical compositions displayed by the plessitic texture.

Furthermore, grains were found that show zoning in major element concentration (Fe, Ni, Co, and Cr) but not in trace element composition (e.g., grain MAC 02675_6.4, see Fig. S2, and also Fig. 2e). Some grains show zoning profiles in some trace elements that are reversed to that of Ni (e.g., grain MAC 02675_4.4, see Fig. S2). Especially affected are Os and Ir. Grain HaH 237_10.5 shows another type of zoning pattern for major and trace elements. Cobalt and Ni concentrations have a maximum in the very core of the grain. Compared to other zoned grains, the reduction of the element concentrations towards the rims is rather steep and evolves into another small plateau, from which Ni and Co contents decrease more smoothly (Fig. 2g).

Part II: Origin of metal from CB chondrites

This pattern is even more pronounced for the refractory trace elements. There is a peak with steep flanks in the core region and another smaller peak in the rim areas on both sides (Fig. 2h).

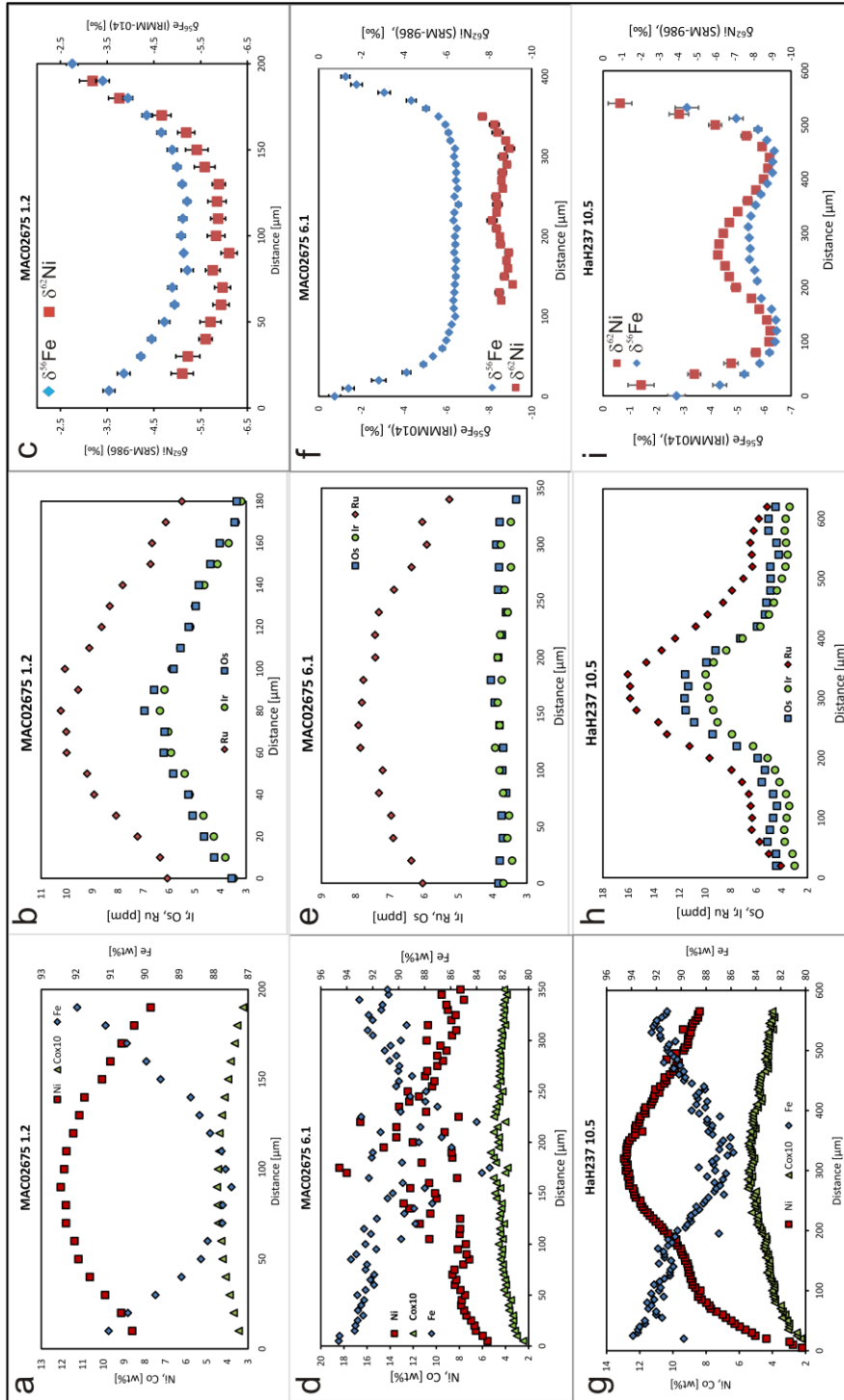


Figure 2: This diagram shows three important types of zoned metal grains. a)-c) represent the most common zoning, with bowl-shaped zoning profiles. a) major element profiles: Ni and Co have higher concentrations in the core than in the rims, while Fe is zoned reversely with lower contents in the core. b) associated trace element profile: refractory elements such as Ir, Os, and Ru have higher contents in the core than in rims. c) isotopic profile with parallel Fe and Ni isotopes zoning and light compositions in the core and heavier compositions at the rims. d)-f) represent zoning of grains with pleissitic texture in the core region. d) major elements display undisturbed dome-shaped [Ni] and bowl-shaped [Fe] zoning at the rims and disturbed scattered zoning in the core region. Co zoning is undisturbed and shows the common bowl-shaped zoning. e) trace element zoning, with refractory elements showing no resolvable zoning (Ir, Os) or common zoning with higher contents in the core than in rims (Ru). f) isotopic profiles with parallel Fe and Ni isotopes zoning profile and a plateau in the core region for Fe isotopes and a weak peak in the core region for Ni isotopes. g)-i) represent a unique zoned grain from HaH237. g) Major element composition shows a similar trend as commonly zoned metals. However, there is a “step” on the flank of the dome-shaped (Ni) or bowl-shaped (Fe) profile. h) Such a step is also apparent in the trace element zoning. i) Ni and Fe isotopes zoning are parallel as observed for commonly zoned metal. However, the profiles are w-shaped, i.e. there is a dome for both, Fe and Ni isotopes, in the very center of the grain.

Part II: Origin of metal from CB chondrites

CI normalized abundances of element concentrations of zoned metal grains reveal an enrichment in refractory elements of ~10-19xCI in the cores of these grains. Rim values are less enriched (Figure 3). Tungsten, and less pronounced Mo (Fig. 3), display negative anomalies relative to other refractory elements. Though moderately volatile elements Au, Cu, and Ge are generally depleted in zoned metal grains, an abrupt increase in the very outer rim can be noticed in some of the grains (especially Cu, see also (Campbell et al., 2005)).

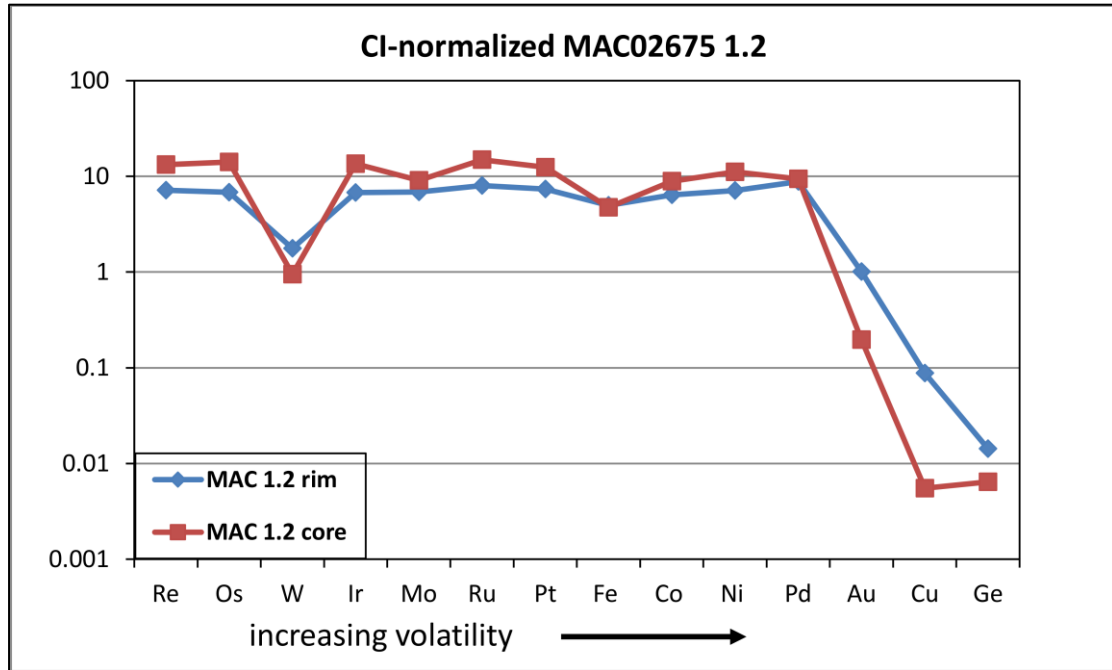


Figure 3: Representative plot of CI-normalized abundances of elements in zoned metal grains. Core (red squares) values are enriched by 12-14xCI and rims (blue diamonds) are enriched by 6-8xCI in refractory elements. Relative to other refractory elements, W is depleted in core and rims. The core also shows a small Mo depletion. The general depletion of moderately volatile elements, is slightly stronger in grain interior than at rim.

4.1.2 Isotopic composition of zoned metal

As already observed previously (Alexander and Hewins, 2004; Zipfel and Weyer, 2007; Richter et al., 2014) nearly all zoned metal grains have significantly lighter Fe isotopic composition in the core than in the rims. First Ni isotope analyses of zoned metal were performed by Alexander and Hewins (2004) and Richter et al. (2014), and indicated that Ni isotopes might be zoned in the same manner as Fe isotopes. However, according to the high uncertainties of the latter measurements, potential zoning was not well resolved. Nickel isotope analyses from our study reveal that nearly all investigated zoned metal grains show positively correlated Ni and Fe isotope zoning patterns (in direction and extent), with several permil lighter isotopic composition in the core than in the rims (Figure 2c,f). The largest fractionation of a core relative to the rims was analyzed in grain MAC 02675_4.4 with core values of: $\delta^{56}\text{Fe} = -7.41 \pm 0.07 \text{ ‰}$ and $\delta^{62}\text{Ni} = -10.85 \pm 0.26 \text{ ‰}$, and rim values of: $\delta^{56}\text{Fe} = -0.2 \pm 0.32 \text{ ‰}$

Part II: Origin of metal from CB chondrites

and $\delta^{62}\text{Ni} = -2.31 \pm 0.46 \text{ ‰}$. This is also the grain with the lightest Fe and Ni isotope composition of all analyzed metal cores.

However, not all zoned grains show a continuous zoning as described above. Grain HaH 237_10.5 also has lighter Fe and Ni isotope compositions in the core than in the rims. However, the core values do not display the lightest isotope compositions of the grain. Instead, both Fe and Ni isotope ratios display a w-shaped pattern (Figure 2i) and the areas between core and rim show the lightest Fe and Ni isotope composition. For grain QUE 94411_1.4, the situation is somewhat different, as Fe isotopes display a w-shaped signature, while Ni shows a more bowl-shaped signature as the majority of all zoned metal grains analyzed. Nevertheless, the Ni isotope pattern shows evidence for a small compositional plateau in the center of the grain (Fig. S3). Potentially, the w-shape pattern for Ni was not observed, as some material was removed during re-polishing before Ni isotope analyses and thus the Ni profile was analyzed further away from the core of the grain than the Fe isotope analyses. Grain MAC 02675_6.1 displays a flat plateau for $\delta^{56}\text{Fe}$ in the core area while $\delta^{62}\text{Ni}$ displays a w-shaped pattern (Fig. 2f).

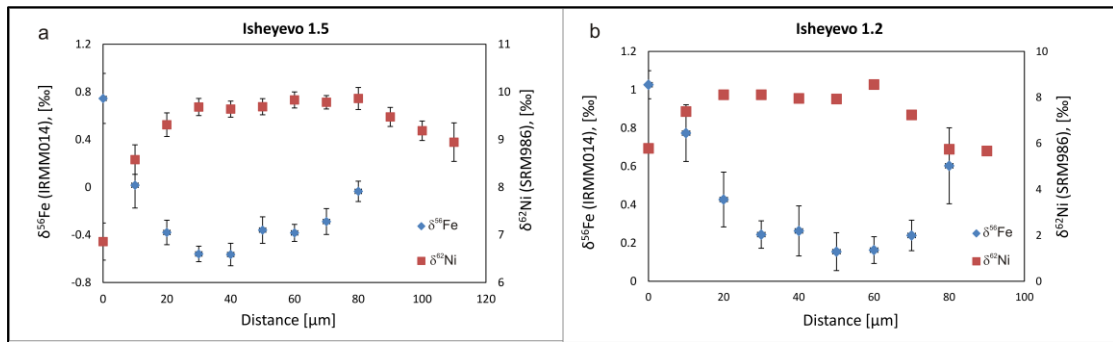


Figure 4: Isotope profiles of grains Isheyev_1.5 (a) and Isheyev_1.2 (b) from CH/CB_b breccia Isheyev. In contrast to other zoned metals, Fe and Ni isotope zoning is not parallel but opposed. Thus, zoning in those grains cannot originate from condensation.

Two of the four examined zoned grains from Isheyev (1.2 and 1.5) show relatively small zoning profiles in Fe and Ni isotopes. Furthermore, Fe and Ni isotopes are reversed. While Fe isotopes show lighter values in the cores than in the rims (1.5 core = -0.6 ‰ and rim about 0 ‰), Ni isotopes display heavier composition in the cores than in the rims (1.5 core = 9.8 ‰ and rim = 8.6 ‰; Fig. 4a). Moreover, it is striking that Ni isotope composition of this grain is much heavier than that of all other zoned metal grains. Table S2 lists the chemical and isotopic composition of cores and rims of all analyzed zoned metal grains.

Part II: Origin of metal from CB chondrites

4.2 Unzoned metal

Several unzoned metal grains from all meteorites studied were analyzed for their Fe and Ni isotope and their chemical composition (Table S3, Fig. 5 and 6). Grains Isheyevov_1.1 and Isheyevov_1.4 both seem to be located in the CB_b lithology rather than in the CH lithology.

4.2.1 Chemical composition

Unzoned metal grains in the CB_a chondrites Gujba, NWA 4025, and Bencubbin have quite a narrow range of Ni concentrations within individual samples, but also among the different meteorites (~5-8 wt% for all three meteorites). Some grains display slightly higher contents of Cr, P, and also Si (e.g., Gujba grain 2.10 see Table S3).

Unzoned metal grains in the CB_b meteorites and in Isheyevov have much more variable Ni contents. In Isheyevov, grains with Ni concentration of about 60 wt% were observed (Ivanova et al., 2008). Moreover, some grains were found with Si contents higher than 10 wt%. Such Ni- and Si-rich metal grains were already described for CH chondrites (Goldstein et al., 2007). Unfortunately, all grains with such high Ni or Si contents were too small (~20 μm in diameter) to be analyzed with the laser for trace elements and isotopes.

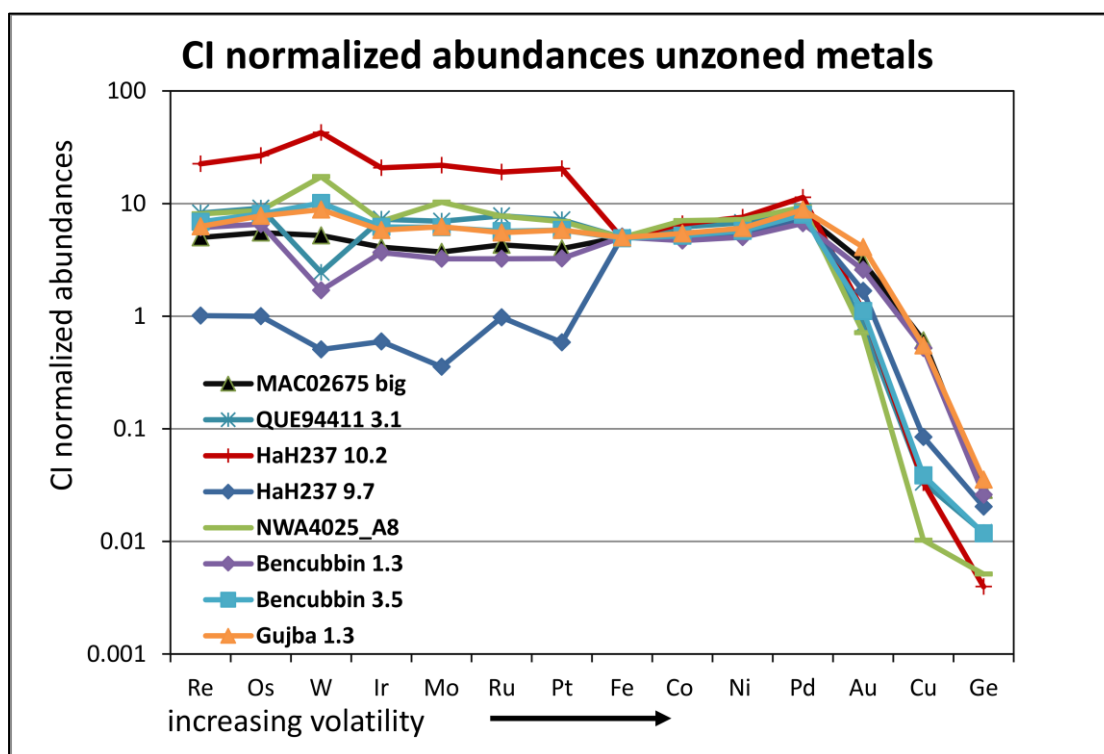


Figure 5: CI normalized abundances of individual trace element analyses in unzoned metal grains from CB_a and CB_b chondrites. Refractory elements are enriched by 4-9xCI in most of the grains. The exceptions, HaH237_9.7 and HaH237_10.2 show depletion or even higher enrichment (20-40 x CI), respectively. Moreover, Mo and W are not depleted in all of the grains relative to other refractory elements. Trace elements are sorted by volatility using 50% condensation temperatures from (Lodders et al., 2009).

Part II: Origin of metal from CB chondrites

Normalizing chemical composition to CI-values reveals an enrichment of refractory elements for the majority of unzoned metal grains of 4-9 times CI (Figure 5). There is only one grain that shows a depletion in elements more refractory than Ni (grain HaH 237_9.7). In contrast, Hammadah al Hamra 237 contains an unzoned metal grain that shows the other extreme, with an enrichment in refractory elements of 20-40 times CI (grains HaH 237_9.6 and HaH 237_10.2, see Figure 5).

Moreover, many unzoned metal grains show depletion in W relative to other refractory elements. However, some grains are enriched in W relative to other refractory elements. Gujba is the only sample that does not display significant depletion or enrichment in W in any of its metal grains, but rather show a slight enrichment relative to other refractory elements.

4.2.2 Isotopic composition

Figure 6 reveals that unzoned metal from CB_a and CB_b chondrites have variable isotope compositions with a total range of $\delta^{62}\text{Ni} \approx -2 \text{‰}$ up to $+ \sim 6 \text{‰}$, and $\delta^{56}\text{Fe} \approx -2 \text{‰}$ up to $\sim +2 \text{‰}$. Thus, Ni isotope values are more variable than Fe isotope compositions. Mean values for Fe and Ni isotope compositions of CB_a and CB_b are somewhat different: $\delta^{56}\text{Fe} = -0.17 \pm 0.65 \text{‰}$ and $\delta^{62}\text{Ni} = 0.51 \pm 0.90 \text{‰}$ (CB_a, errors = σ) and $\delta^{56}\text{Fe} = -0.24 \pm 0.87 \text{‰}$ and $\delta^{62}\text{Ni} = 1.46 \pm 2.14 \text{‰}$ (CB_b, errors = σ). Thus, CB_b and CB_a chondrites have quite similar Fe and Ni isotope compositions. The scatter in the Ni isotope composition within CB_b chondrites is larger than in CB_a chondrites. However, isotope compositions in CB_a and CB_b chondrites are overlapping. Values of Isheyevo fall into that range, with averages of $\delta^{56}\text{Fe} = 0.05 \pm 0.31 \text{‰}$ (σ) and $\delta^{62}\text{Ni} = 2.13 \pm 2.28 \text{‰}$ (σ). It can also be observed that the majority of grains have quite similar isotope compositions and that only a few individual grains are isotopically significantly heavier or lighter than the average. Scattering is differently strong pronounced in individual samples. For example, HaH 237 has the smallest spread among CB_b chondrites, especially in the Fe isotope composition (see Fig. 6).

Figure 6 also reveals that there is one grain each within the CB_a chondrite samples that has lighter Ni isotope compositions than the other ones. Moreover, some unzoned grains from MAC02675 and Isheyevo have significantly heavier Ni isotope composition than the majority of grains. Such hiatus cannot be observed for Fe isotope compositions.

Part II: Origin of metal from CB chondrites

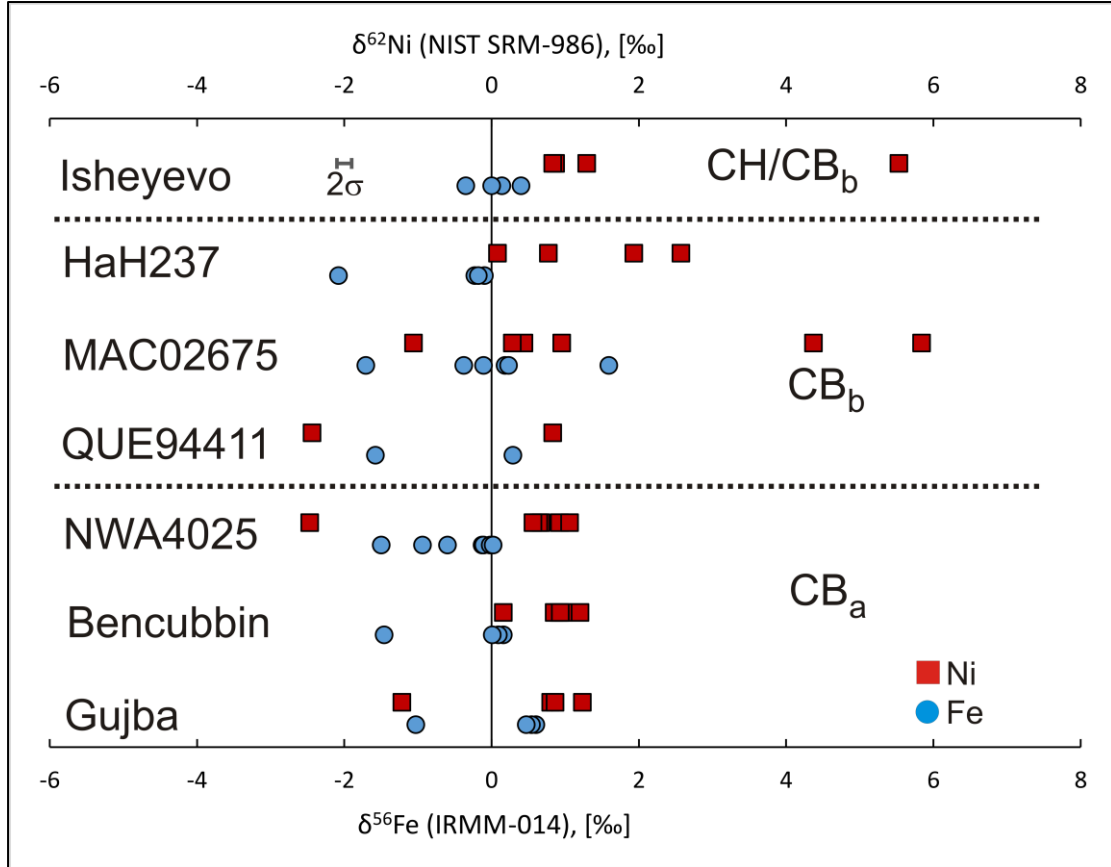


Figure 6: Fe (blue) and Ni (red) isotope composition of unzoned metal grains from the different examined CB chondrites. Error bar: $2\sigma = 0.1$ ‰.

5 DISCUSSION

5.1 Origin of zoning in metal

Since the first recognition of CB_b chondrites (Righter and Chabot, 1998; Zipfel et al., 1998), several models were proposed aiming to explain the origin of zoned metal in CB_b and CB_a chondrites (Meibom et al., 1999; Campbell et al., 2001; Meibom et al., 2001; Petaev et al., 2001; Campbell et al., 2002; Petaev et al., 2003; Campbell et al., 2005; Fedkin et al., 2015). These models consider compositional zonation profiles of major and minor elements as well as refractory siderophile elements of slightly different volatilities (Meibom et al., 2000; Petaev and Wood, 2000; Campbell et al., 2001; Meibom et al., 2001). Campbell et al. (2001) found that zoning patterns and abundances are broadly volatility controlled but cannot be explained by a simple equilibrium fractionation model under typical solar nebula conditions. Though refractory elements are enriched in grain centers, there is no spike of highly refractory siderophile elements (RSE) that would indicate sole condensation of RSE before condensation of Ni and Fe. The lack of a spike, as well as chondritic abundance of RSE at grain rims, are the

Part II: Origin of metal from CB chondrites

major evidence arguing against equilibrium condensation. Campbell et al (2001) explained their findings by two models either (1) fractional condensation from a supersaturated gas at high temperatures and cooling rates or (2) diffusive exchange between a RSE-rich core and RSE-poor rim.

Our data on the isotopic composition of Fe and Ni, however, allow to put further constraints on the origin of zoned metal grains. Zoning of Fe and Ni isotope compositions is largely parallel (Figs. 2c,f,i) and correlated to the zoning of RSE in zoned metal (Fig. 2). Both isotope systems are of lighter composition in the cores than in the rims. These findings exclude a dominant role of subsolidus exchange diffusion in response to, e.g., chemical gradients or changing oxygen fugacity, as such processes would generate reverse Fe and Ni isotope zoning (as e.g. observed for a kamacite-taenite interface in Chernozhkin et al. (2017); Weyrauch et al. (2017)). Thus, we conclude that zoning in metal grains originates in disequilibrium condensation.

The isotope fractionation of Fe and Ni of several permil, with extremely light Fe and Ni isotope ratios in the cores, strongly indicate kinetic isotope fractionation during grain growth by condensation. The average kinetic energy of all components in a gas at a given temperature can be expressed by the following equation $K_E = 1/2m \cdot v^2$, where m = mass, v = velocity. Therefore, lighter isotopes move faster than heavier isotopes, resulting in a higher collisional frequency of light isotopes (Schauble, 2004). In such a scenario, condensing metal incorporates preferentially light isotopes leaving the heavier isotopes in the gas phase. Accordingly, under conditions of fractional condensation from a finite gas reservoir, the gas becomes more and more enriched in heavy isotopes during progressive grain growth. This would result in isotopically heavy rims, assuming they formed late from a gas reservoir depleted in light isotopes. Such rapid compositional changes are more consistent with a confined gas reservoir, such as an impact-related vapor plume rather than solar nebula conditions.

The estimated highest possible mass-dependent fractionation of Fe and Ni isotopes from kinetic energy considerations of above (Schauble, 2004) is about 9 permil/amu and 8 permil/amu, respectively, which is about double of what we observe. However, this result may be considered as an endmember of such a condensation process. Several factors can explain a lower observed fractionation for both, Fe and Ni isotope systems: (1) the calculation does not take any back-reactions into account. Partial equilibration would lead to flattening of the isotope zoning since the condensate has the higher binding energy than the gas, and would primarily build in heavier isotopes under equilibrium conditions. (2) diffusion can also take place between the forming layers during condensation of the metal grains. (3) diffusion subsequent to grain growth would also flatten the Ni-isotope profile, however, steepen the Fe-isotope profile. Nevertheless, the fractionation of both isotope systems between core and rims

Part II: Origin of metal from CB chondrites

among zoned grains is quite similar. Thus, diffusion only played a minor role during formation of zoned metal and was outpaced by the fast growth of such grains. Moreover, the very rims of zoned grains do not show reversed zoning of Fe and Ni isotopes as may be expected if diffusion played a role. However, our measurements only allow limited spatial resolution of about 30 μm and most grains display frayed rims. Therefore, we cannot exclude minor diffusion effects.

5.2 Compositional variation of zoned metal

The core and rim isotope values among different zoned grains are varying strongly (e.g. core values of QUE 94411_3.3 with $\delta^{62}\text{Ni} = -2.31 \pm 0.18\text{‰}$ vs MAC 02675_4.4 with $\delta^{62}\text{Ni} = -10.85 \pm 0.26\text{‰}$). One factor that affects the rim compositions is the fragmented character of the grains. Most of the metal grains show frayed rims, and some grains even seem to be broken (Figure 1a). Varying core values could have several explanations. The most likely one are cutting effects, i.e. tangential cuts closer to grain rims that would result in a systematic shift towards heavier isotopes. Thus, all isotopic core composition of normally zoned grains are maximum values and the lightest isotopic core values (e.g.; grain MAC 02675_4.4 $\delta^{56}\text{Fe} = -7.41 \pm 0.07\text{‰}$ and $\delta^{62}\text{Ni} = -10.85 \pm 0.26\text{‰}$) are more likely to represent real core composition compared to grains with less pronounced zoning. Additionally, it needs to be taken into account that because of the width of the laser beam each individual measurement is integrating an area of 30-40 μm . Thus, in particular at the rims, but also potentially for some of the cores with steep zoning patterns, delta values represent mixed signatures and isotope fractionation between real cores and the very rim may be even larger than those observed. Furthermore, the formation of some of the zoned grains likely started at a time, when the gas reservoir was already depleted in light isotopes.

Finally, the factors (1) and (2) from above, which may have limited the overall extent of observed isotope fractionation, may also have generated additional variations between individual zoned grains.

5.3 Compositional variations of unzoned metal

Compared to zoned grains, unzoned grains display a more limited range and also heavier Fe and Ni isotope compositions, relatively close to chondritic values. Furthermore, they formed from a reservoir that remained chemically and isotopically constant during their formation. Such conditions are more consistent with equilibrium condensation.

Excluding some grains that are isotopically lighter than the majority, the ranges of Fe and Ni isotopic compositions displayed by unzoned metal grains within the CB_a chondrites are

Part II: Origin of metal from CB chondrites

relatively narrow, close to chondritic compositions ($\delta^{56}\text{Fe} = -0.6$ to 0.61 ‰ and $\delta^{62}\text{Ni} = 0.56$ to 1.23 ‰). However, all three investigated CB_a meteorites show one grain that is significantly lighter than the others in the Ni isotope composition, and also show the lightest Fe isotope compositions within those samples. The isotopically light grains from Gujba and Bencubbin have slightly higher concentrations of Si, P, and Cr than other metal in these meteorites. Some metal grains in CB_a chondrites have sulfide laths or show sulfide blebs, however, no correlation between isotope or chemical compositions and the occurrence of sulfides was observed. The isotope and trace element compositions of unzoned grains in CB_b chondrites vary more strongly (Figures 5 and 6). However, there is no correlation of the isotope composition with the chemical composition of the grains (Table S3, Fig. 6). For example, grain MAC 02675_6.3 has the heaviest Fe isotope composition ($\delta^{56}\text{Fe} = 1.59$ ‰) and grain HaH 237_10.4 has the lightest Fe isotope values ($\delta^{56}\text{Fe} = -2.08$ ‰), but both grains show very similar trace element compositions (Table S3). Furthermore, Ni isotope compositions show more variation towards heavier values than Fe isotopes ($\delta^{62}\text{Ni} = -2.44$ to 5.84 ‰ vs. $\delta^{56}\text{Fe} = -2.08$ to 1.59 ‰).

Assuming, unzoned metals formed generally under more equilibrium like conditions, chemical and isotopic signature of individual unzoned grain essentially reflect the local gas composition and thus, variations among unzoned metals most likely reflect heterogeneities in the gas reservoir. Considering condensation from an impact plume, isotopic variations around the chondritic compositions may be explained by a reservoir that was not completely mixed after evaporation. A possible explanation for grains with light isotope composition, could also be minor effects of kinetic isotope fractionation.

Heavier isotope compositions may be explained by the tendency of the condensate to bind heavy isotopes under equilibrium conditions (White, 2001). However, this effect might be too small to explain the observed values. Instead, heavier than chondritic isotope compositions may be related to turbulent mixing within an impact plume, resulting in mixing of gas that was depleted in light isotopes, possibly after formation of the isotopically light zoned metal and respective reservoir effects, into the source region of unzoned metal grains.

Campbell et al. (2002) and Fedkin et al. (2015) describe Pd/Fe and Ir/Fe ratios in unzoned metal from CB chondrites to be higher (up to two times) compared to the solar ratios (Pd/Fe = $3.0 \cdot 10^{-6}$ and Ir/Fe = $2.5 \cdot 10^{-6}$ (Lodders et al., 2009)). From the enrichment of Pd and Ir relative to Fe they conclude that the system must have been enriched in siderophiles and partial pressures of siderophiles were very high (Campbell et al., 2002; Fedkin et al., 2015). We find that unzoned grains from CB_a and CB_b chondrites have ranges of Pd/Fe and Ir/Fe ratios that are overlapping with each other and in average are somewhat higher than the solar ratios (Fig. 7).

Part II: Origin of metal from CB chondrites

Our ratios in combination with our observation that there are no significant trace element or isotope compositional differences between unzoned metal from CB_a and CB_b chondrites, indicate that all unzoned metals in both groups have formed by the same process and in the same reservoir.

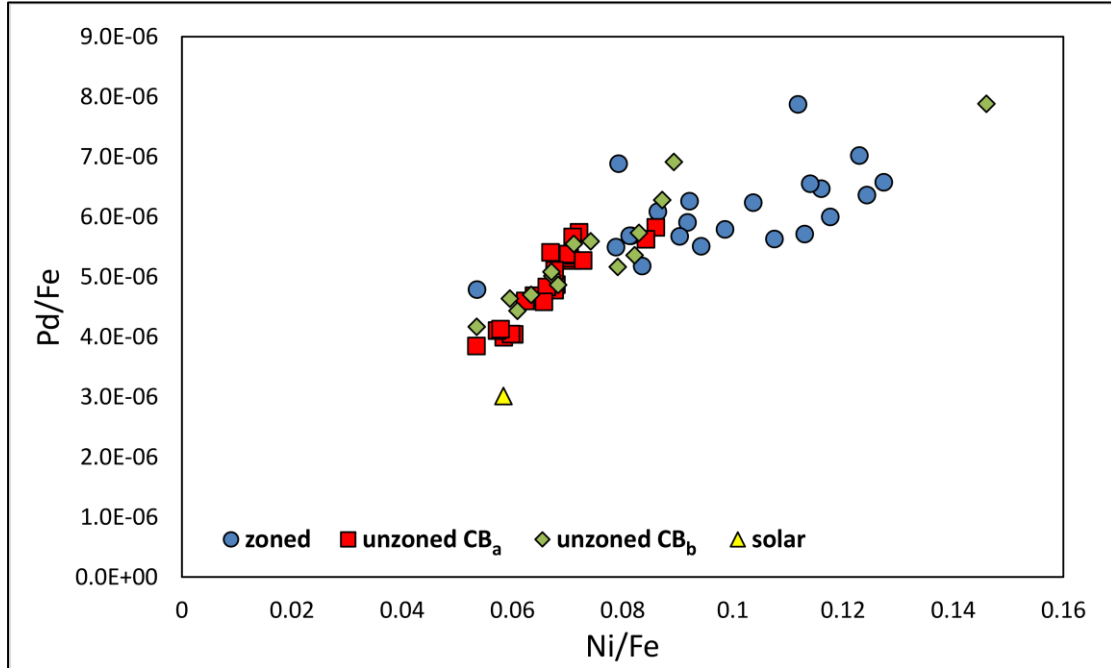


Figure 7: This plot demonstrates that Pd and Ni are enriched in CB_a and CB_b chondrites relative to the solar values (yellow triangle, Lodders et al., 2009). Such enrichment suggests enhanced abundances of siderophile elements within the gas reservoir and also increased partial pressures for siderophile elements (Campbell et al., 2002 and Fedkin et al., 2015). It becomes obvious that unzoned grains from CB_a and CB_b grains plot together, which indicates a common origin. Zoned metal from CB_b chondrites are even more enriched than unzoned grains.

5.4 Properties of the impact plume

5.4.1 Gas evolution during condensation of zoned and unzoned metal

Figure 8 displays the relationship of Fe isotope and Ni isotope compositions of unzoned grains, and cores and rims of zoned grains. Evidently, zoned metal cores are isotopically lighter than rims, and significantly lighter than most unzoned metal. Moreover, the majority of the unzoned grains scatters around delta values of 0 ‰. However, some unzoned grains have more variable isotope composition and plot within a similar range as the rims of zoned metal grains. Overall, there is a positive correlation of Fe and Ni isotope composition within the zoned and unzoned metals. Such a correlation supports a condensation origin in a similar environment for zoned and unzoned metal from CB chondrites. Additional information may be extracted from the relationship of isotope signatures and RSE, as shown in Figure 9.

Part II: Origin of metal from CB chondrites

Figure 9 displays the Ni isotope compositions of the analyzed metals plotted against the respective Ir concentrations. Replacing Ni with Fe isotopes would result in a similar plot due to the positive correlation of Fe and Ni isotope compositions (Fig. 8). In this plot (Fig. 9) zoned and unzoned metal grains show different trends, indicating that they did not form at a specific time during the formation of zoned grains, but rather formed simultaneously at different conditions and likely in a different environment. Cores of zoned metals show a positive correlation of Ir contents and Ni isotope compositions.

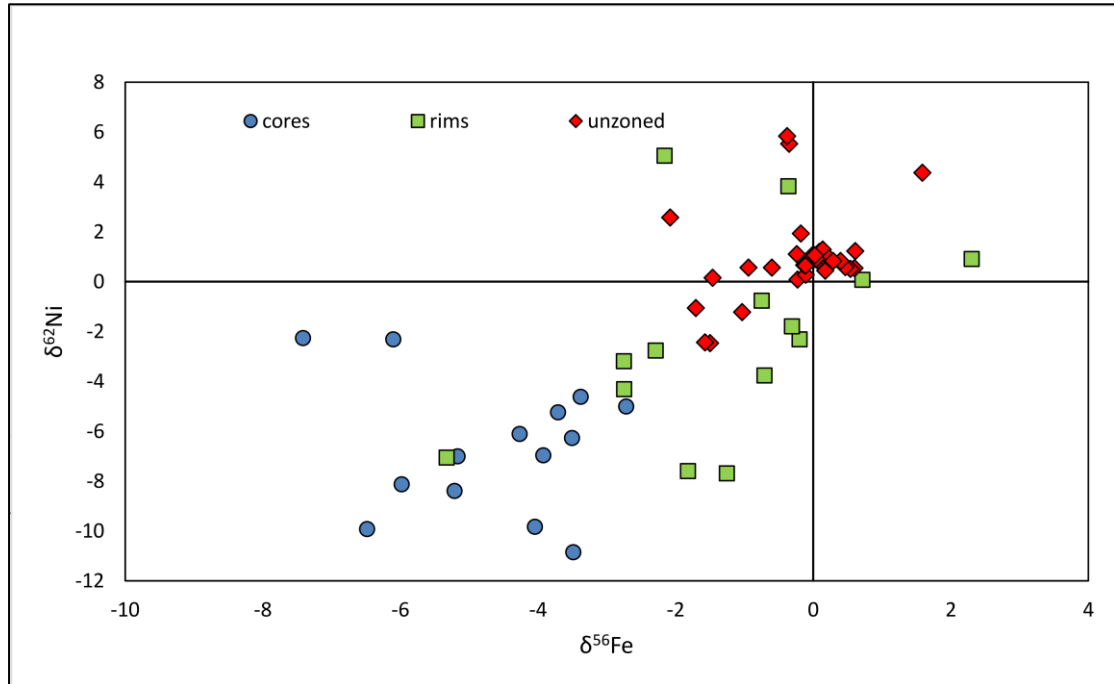


Figure 8: Nickel vs Fe isotope plot, revealing that cores of zoned metal grains are isotopically lighter than unzoned metal grains and rims of zoned metal. The rims of zoned metal grains overlap with unzoned metal grains. Those isotopic differences suggest different formation conditions for zoned and unzoned metal grains.

In more detail, two groups of zoned metal grains can be distinguished. Group I includes cores with the lightest isotope compositions and low concentrations in refractory elements and associated rims have similar RSE concentrations but significantly heavier isotopic compositions (arrow I in Fig. 9). Group II has cores with the highest concentration of refractory elements but have heavier isotope composition than group I cores, while associated rims have similarly low RSE concentrations and heavy isotope compositions as group I rims (arrow II in Fig. 9). The difference between the two groups may be related to their formation conditions. Group I grains with the lightest isotope composition probably formed in a rapidly cooling and supersaturated gas reservoir and are thus, more strongly affected by kinetic isotope fractionation compared to the cores of group II grains. As group II grain cores also display the highest Ir contents, they may have formed during a mixture of kinetic and more equilibrium-like conditions in a less rapidly cooling gas reservoir. Campbell et al. (2001) calculated the Ni

Part II: Origin of metal from CB chondrites

and Ir compositions that can be expected during equilibrium condensation of Fe,Ni-metal. Compositions of group II metal grains roughly correspond to those calculated values. Rims of zoned metal grains of both groups have variable Fe and Ni isotope compositions that do not correlate with the contents of refractory trace elements. In both groups, rims condensed from a reservoir that was variably depleted in light isotopes and refractory elements, as the result of progressive condensation of metal. Both grain populations can be found within a single meteorite.

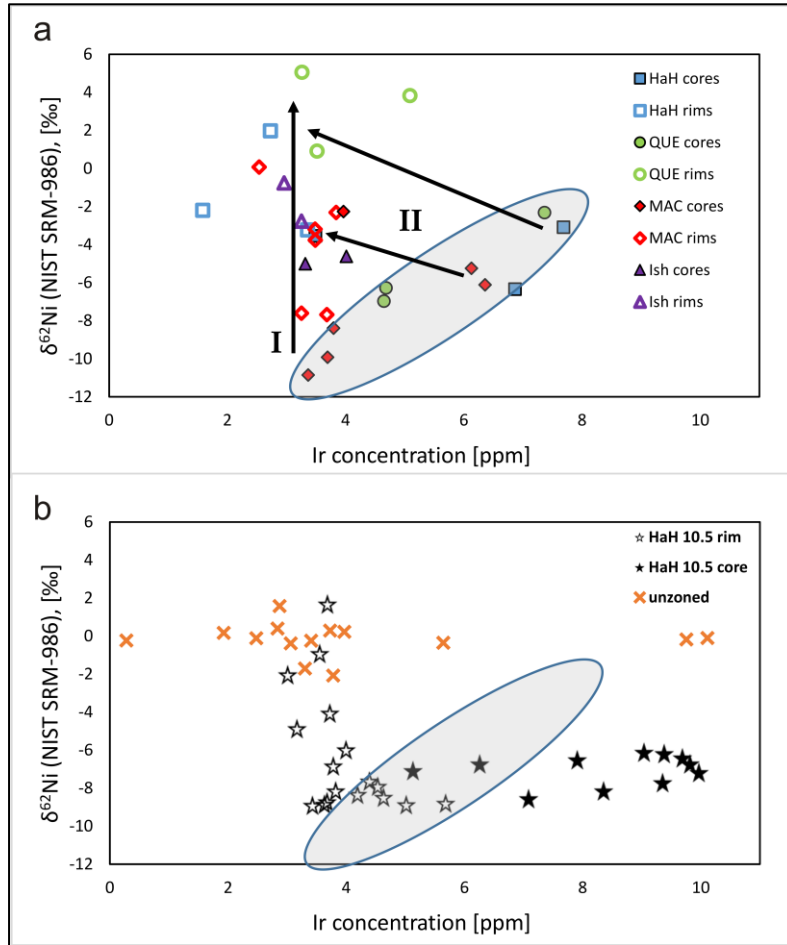


Figure 9: Ni isotope composition plotted against Ir content of zoned and unzoned grains from the herein examined samples. a) Only cores (filled symbols) and rims (open symbols) of zoned grains are shown. There are two different grain populations defined by the core composition and evolution trend of the grains. Group I has cores with light Ni isotope composition and rather low Ir concentrations and associated rims have about the same Ir concentration as cores, but heavier Ni isotope composition. Group II has cores with high Ir concentrations and associated rims become heavier in isotope composition and less enriched in Ir. The blue field underlines the positive correlation of Ni isotope composition and Ir concentration. b) unzoned grains are shown, as well as core and rim regions of the exceptional grain 10.5 from HaH 237. Unzoned metals mainly scatter around 0‰ and have variable Ir concentrations. The core region of HaH 237_10.5 depicts the whole range of core compositions from a) only the correlation trend of Ni isotope composition and Ir concentration is somewhat flatter.

Unzoned metal grains do not show a correlation between $\delta^{62}\text{Ni}$ and RSE (Fig. 9). The majority of the grains, display $\delta^{56}\text{Fe}$ and $\delta^{62}\text{Ni}$ around of 0 ‰ ($\pm 0.6\text{‰}$ and $\pm 1\text{‰}$, respectively), however, with highly variable contents of refractory elements. The low isotopic variability suggest that Ni and Fe of unzoned metal condensed from a less rapidly cooling gas at temperatures between 1360 and 1260 K (Campbell et al., 2001) under conditions with limited kinetic isotopic fractionation. Thus, unzoned metals most likely condensed in a slow-cooling gas reservoir and the variable RSE contents likely reflect variable RSE depletion of the gas reservoir at the time of their formation.

Part II: Origin of metal from CB chondrites

5.4.2 Oxidizing conditions in the impact plume: Evidence from Mo and W

Our data show strong enrichment in highly refractory siderophile elements with negative anomalies of W and Mo in the zoned grains. It is not expected that increasing oxygen fugacity would influence the general condensation behavior of RSE, except for W and Mo (Fegley and Palme, 1985). Both Mo and W are oxygen sensitive. Thus, the negative anomalies of Mo and W relative to other RSE indicate elevated oxygen fugacities in the gas reservoir. However, Mo is more oxygen sensitive than W during condensation and is expected to be stronger depleted than W. On the other hand, W is more oxygen sensitive than Mo during evaporation. Experimental data show that at higher temperatures and under solar nebula oxygen fugacity, W preferentially forms W-oxides in the gas phase, whereas molybdenum occurs as Mo (Fegley and Palme, 1985). Fast growth of metal from an oxidized gas reservoir could inhibit the equilibrium reaction of W with W-oxides in the gas phase and lead to a W depletion in the metal as most W would remain oxidized. Under the same disequilibrium conditions, Mo would then be incorporated as Mo-alloy into the metal grains. In fact, zoned metal exhibits a negative W anomaly and no or only a small Mo depletion compared to other refractory elements. These findings are in accordance with formation of metal under non-equilibrium conditions similar to those concluded from Fe and Ni isotopes.

Our Mo and W data indicate oxygen fugacities that exceed those of the solar nebula. Meibom et al. (2001) also state that metals have condensed under relatively oxidizing conditions, as Cr values are lower than in metals formed from a solar gas. They estimated dust/gas ratios from Cr compositions of zoned grains and gave values between $D/G = 10$ and $D/G = 30$.

Such an increased dust/gas ratio would lead to an oxygen fugacity higher than in the canonical solar nebula (Fedkin and Grossman, 2016). An impact of planetesimals is a likely event to form a vapour plume with such conditions. Therefore, we suggest that zoned and unzoned metal grains from CB chondrites both condensed from a confined reservoir with strong temperature gradients and variable cooling rates under non-equilibrium conditions, in accordance with conclusions drawn from the elemental and isotopic signatures of the metal grains.

In such a scenario zoned metal grains most likely formed in the fast-cooling outer shell region of an impact plume, while unzoned metal condensed in the inner slow-cooling region. This conclusion is consistent with earlier findings by Rubin et al. (2003), who concluded that unzoned and zoned metal formed in the same plume, but that unzoned metal condensed in a region of higher density than zoned metal. This conclusion is also consistent with the modelling

Part II: Origin of metal from CB chondrites

results of Fedkin et al. (2015) who found that total pressures during condensation were higher for unzoned grains ($P^{\text{tot}} 10^{-2}$ to 10^{-3} bar), than for zoned grains ($P^{\text{tot}} 10^{-5}$ to 10^{-8} bar).

The time-dependent evolution of an individual zoned grain may have started with condensation in a gas reservoir under conditions that resulted in either more equilibrium-like or dominantly kinetic isotope fractionation, depending on cooling rate, and ended in a gas reservoir that was depleted in light Fe and Ni isotopes, and RSE. In general, the condensation conditions for all zoned metals is dominated by kinetic fractionation. Grain HaH 237_10.5 is an exceptional grain. Isotopes and elemental composition of the grain center span the whole compositional range of the cores shown in Figure 9b. The observed w-shape isotope pattern and variable Ni isotope vs Ir signature of the core area of this grain may indicate its condensation under variable cooling rates, resulting in initially more equilibrium-like, followed by strongly kinetic isotope fractionation. Such trace element and isotope patterns in HaH 237_10.5 may have derived from local differences in the gas reservoir. In this scenario, the metal grain has likely moved through the gas reservoir during its growth, from more inner towards outer regions of the vapor plume. Or changes of the formation conditions have appeared locally during formation of grain HaH 237_10.5.

5.5 Possible formation processes of unusual zoning patterns in metal

5.5.1 Uncontinuous zoning and plessite

As described above some zoned metal grains show an uncontinuous chemical zoning (Fig. 2d). Those are also the ones displaying a different isotopic zoning (Fig. 2f). Closer optical examination reveals that these metals have a plessitic texture in their cores (Fig. 10). However, the rim regions do not show such a texture and zoning is obtained in there. The uncontinuous zoning may be explained by the plessite. The fine exsolution of kamacite and taenite in the core of the grain can be resolved with the small beam of the electron microprobe and gives a zig-zag pattern due to the different Ni contents of the two Fe,Ni-alloys. Trace element zoning, analyzed with LA-ICP-MS, seems continuous, as the laser beam is larger and cannot spatially resolve the small laths. The isotopic zoning shows a large flat plateau in the center (Fig. 2f). This homogeneous composition is also caused by the large laser spot which does not allow resolution of the single kamacite or taenite laths. The different shape of zoning (compared to the usual bowl-shape) is likely being related to the exsolution of kamacite and taenite and Fe and Ni isotope fractionation between both phases. Isotopic variability is stronger for Ni, as the relative change in the Ni concentration is higher than that of Fe, resulting in a stronger Ni

Part II: Origin of metal from CB chondrites

isotope fractionation between kamacite and taenite, as compared to Fe isotopes (Dauphas, 2007; Weyrauch et al., 2017).

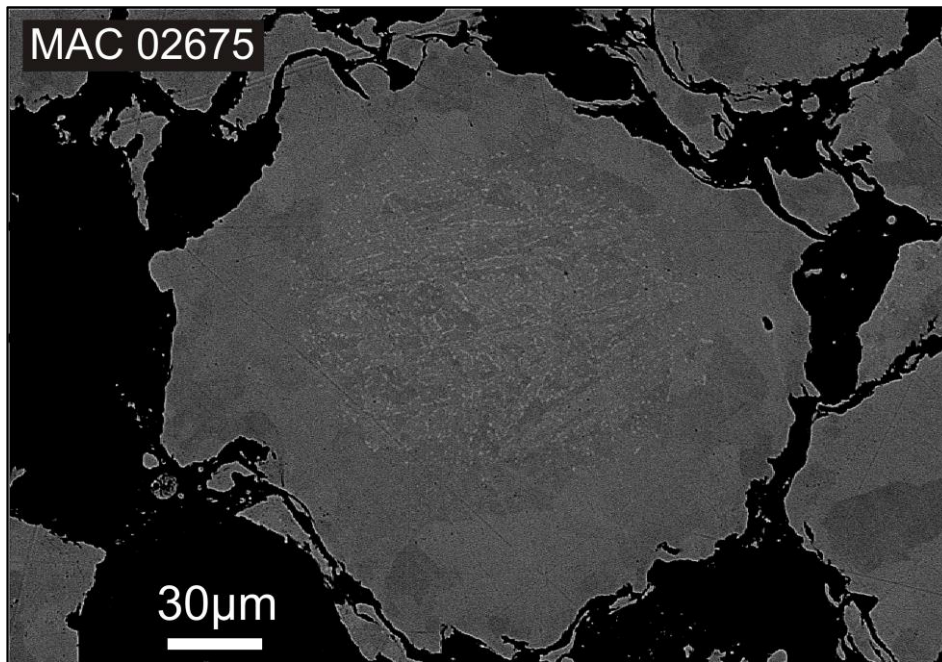


Figure 10: BSE image of grain MAC 02675_2.1 revealing plessitic texture in the core area.

There must have been a short reheating event that resulted in the exsolution of fine laths of taenite and kamacite in the core of such grains without disturbing the initial zoning. Such an event may have been shock reheating (Brearley and Jones, 1998). Since all CB_b chondrites have abundant shock veins it seems likely that plessite in combination with zoning originate in such shock reheating. However, Meibom et al. (2005) found that plessitic texture in the cores of metal grains, follow the distortion of the grains. Thus, they conclude that plessite must have formed prior to the shock event that caused distortion of the metal. If plessite really formed due to shock reheating, it needs to be considered that CB parent bodies experienced several shock events.

5.5.2 Reversed zoning in grains from Isheyev

Two of the examined zoned metal grains from Isheyev show a different isotopic zoning than all other examined zoned grains in the samples here. In these grains, Fe and Ni isotopes are only weakly, but reversely zoned (Fig. 4). Nickel has heavier composition in the core than in the rims, and Fe has lighter isotopic composition in the core than in the rims. Combining these results with the Fe and Ni concentrations of the grains indicates that the zoning was generated by chemical diffusion, i.e. Fe (and preferentially light Fe isotopes) diffused into-, and Ni (and preferentially light Ni isotopes) diffused out of these grains, resulting in the light Fe

Part II: Origin of metal from CB chondrites

and heavy Ni isotope compositions observed in the cores (Richter et al., 2003; Dauphas, 2007; Weyrauch et al., 2017). Since no other zoned metal grains were found in contact with grains Isheyevo 1.2 and 1.5, diffusion may have occurred during chemical re-equilibration of these metals with the surrounding gas. For those two grains, grain growth was apparently slow relative to Fe-Ni exchange diffusion.

6 CONCLUSION

This study of zoned and unzoned metal grains from CB chondrites demonstrates that metal in CB_a and CB_b chondrites most likely have formed by condensation from an impact-induced vapor plume. Combined results of isotope composition and refractory element concentrations show that the formation of zoned metal is dominated by kinetic isotope fractionation during condensation which can be achieved by fractional condensation in a fast-cooling reservoir. Thus, grains with the lightest isotopic core composition most likely have formed in the outer regions of the impact plume. Unzoned metal, however, have formed under more equilibrium-like conditions, and thus, most likely in the slow-cooling interior of the impact plume. Depletion of Mo and W relative to other refractory elements suggest elevated oxygen fugacities. We interpret these isotopic and RSE signatures in metal to be generated by condensation from a giant impact cloud. Compositional variabilities among, and in cases within individual metal grains may be caused by turbulences in the gas reservoir and transport of grains during growth. Those turbulences would allow grains to move within the vapor plume, thus sampling the chemically and isotopically heterogeneous gas reservoir, as it is indicated, e.g. by the complex zoning in one of the zoned grains from HaH 237.

Part III: Constraints on the relationship of CH, CB, and CR chondrites from metal grains

The MATLAB code, used for modelling in this chapter, kindly was written by Ralf Dohmen.

1 ABSTRACT

Due to similarities in chemical composition and common Cr, Ti, N and O isotope trends, the metal-rich CR, CH and CB chondrites are thought to be related with each other. This study aims to shed light on this relationship by the investigation of zoned and unzoned metal grains from CR and CH chondrites. Trace element and Fe and Ni isotope compositions were determined by *in situ* femtosecond (*fs*) LA-(MC-)ICP-MS analyses. Results from this study were compared to isotope and trace element compositions from CB chondrite metal.

Chemical compositions of unzoned metal from CR, CH, CB_a, and CB_b chondrites are very similar with enrichment in refractory elements and depletion of moderately volatile elements relative to the solar values. Such signatures are consistent with condensation from a gas with solar composition. However, the range in Fe and Ni isotope compositions of CR chondrite metal is much smaller than that displayed by CH and CB chondrite metal. This observation in combination with the significantly different textures of metal and chondrules, indicate different formation histories for CH and CB chondrites. Both zoned and unzoned metal from CH and CB chondrites display very similar trace element and isotope compositions, indicating they likely formed within the same event, during non-equilibrium fractional condensation from an impact-induced vapor plume. Zoned metal formed in the fast-cooling outer shell region of the plume and is dominated by kinetic fractionation, while unzoned metal condensed under more equilibrium-like conditions in the slow-cooling interior of the plume. Preliminary modelling of isotopic and chemical zoning in metal reveal cooling rates of 0.02 K/h. Variability in metal isotope composition among different unzoned grains may be explained by reservoir effects in the plume. Textural differences between CH and CB_b are most pronounced in the mean grain size, which may be attributed to grain-size sorting. Size sorting

Part III: Relationship of CH, CB, and CR chondrites

could also explain the lack of zoned metals in CB_a chondrites, as zoned metals in CB_b and CH chondrites are by a magnitude smaller than the mean metal grain size of CB_a chondrites.

In contrast, CR chondrite metal formation is best explained by condensation and subsequent heating events that caused equilibration of metal with the silicates. The narrow range in trace element, and Fe and Ni isotope compositions suggest that reservoir effects only played a very minor role during formation of CR chondrite metal.

Since CR chondrite metal has formed in a different process than that of CH and CB chondrites, the similarities in Cr, Ti, N and O isotope compositions of these meteorite groups need to be explained otherwise. Those similar isotope compositions of the different meteorite groups may (1) reflect the composition of a common accretion region (2) share common precursor materials, or (3) indicate that a CR chondrite body was involved in the impact event, CH and CB chondrites formed from and that isotope signatures of CH and CB chondrites were inherited from the CR impactor.

2 INTRODUCTION

CR, CH, and CB chondrites are joined as the CR clan chondrites due to similar chemical characteristics (Weisberg et al., 1995). All three chondrite groups have metal contents that are higher than in other chondrite groups. CB chondrites have the highest abundance with up to 70 vol% metal (Newsom and Drake, 1979; Righter and Chabot, 1998; Zipfel et al., 1998; Weisberg et al., 2001; Rubin et al., 2003), CH meteorites have up to 30 vol% (Krot et al., 2002), and CR chondrites have approximately 7-9 vol% metal (Bischoff et al., 1993; Weisberg et al., 1993; Krot et al., 2002). Moreover, they all form a mixing line regarding the oxygen isotope composition (Clayton, 1993; Clayton and Mayeda, 1999). Another similarity is the anomalously high ¹⁵N abundance (Franchi et al., 1986; Weisberg et al., 1995; Weisberg et al., 2001) and the occurrence of hydrous matrix in CR chondrites, and hydrous clasts in CH and CB chondrites (Weisberg et al., 1995; Greshake et al., 2002; Krot et al., 2002; Bonal et al., 2008). Another feature that differentiates CH, CB, and CR chondrites from other chondrite groups are the relatively young chondrule ages. Chondrules from CR chondrites formed ~3.6 Ma after CAIs (Budde et al., 2018) and those of CB ~5 Ma after CAIs (Kleine et al., 2005; Krot et al., 2005; Bollard et al., 2015). While CR clan chondrites are compositionally similar, their textures are significantly different. Metal in CR chondrites is apparent in three different types (1) inner chondrule metal, (2) metal in chondrule rims, and (3) isolated metal grains in the matrix (Krot et al., 2002). No metal is apparent in CB_b chondrules and occurrence of metal in chondrules from CH samples is rare (Krot et al., 2002). Probably the most striking feature of CH and CB_b chondrites are chemically and isotopically zoned metal grains (Meibom et al.,

Part III: Relationship of CH, CB, and CR chondrites

1999; Weisberg and Prinz, 1999; Alexander and Hewins, 2004; Zipfel and Weyer, 2007; Richter et al., 2014; and part II of this thesis), as well as the lack of matrix in CB_b and CB_a chondrites. In contrast, CB_a chondrites do not contain any zoned metal grains (Weisberg et al., 2001) and metal occurs as up to cm-sized aggregates, which can only occasionally be found in CB_b chondrites and not at all in CH chondrites (Weisberg et al., 1995; Rubin et al., 2003). The grain size is a general difference of these chondrite groups: CB_a chondrites are mostly coarse-grained with up to cm-sized metal aggregates and large silicate clasts or fragmented macro chondrules (mm to cm size; Rubin et al., 2003); CB_b chondrites have smaller metal grains (on average 200 μm and rare appearance of cm-sized aggregates) and chondrule sizes of 50-200 μm in diameter; CH chondrites have the smallest grain sizes with metal grains of mainly 80-150 μm in diameter and mean chondrule size of 90 μm (Weisberg et al., 1995). The dominating chondrule type in CH and CB_b chondrites is the cryptocrystalline texture, but also fine-grained barred olivine chondrules occur (Weisberg et al., 1995; Krot et al., 2002). In contrast to that, chondrules in CR chondrites are larger with average diameters of ~ 800 μm and textures are mainly porphyritic (Weisberg et al., 1995). The textural differences argue against a common formation process/origin (Weisberg et al., 1995; Krot et al., 2002). While condensation from an impact plume is suggested for components in CH and CB chondrites (see previous chapter of this study), there are several different models for the formation of CR chondrite constituents (Zanda et al., 1994; Conolly et al., 2001; Zanda et al., 2002; Jacquet et al., 2013). All these models find consensus in a close relation of metal and chondrule formation. However, some studies (e.g., Weisberg et al., 1993) suggest metal in CR chondrites to have formed by direct condensation from a gas of solar composition before formation of chondrules. Other studies propose that at least some of the metal within chondrules was formed due to reduction of FeO while chondrules were in a molten state, which would explain the loss of volatile elements in those metals (Conolly et al., 2001). In such a scenario, CR metal would have crystallized from an immiscible metal melt within the chondrules (Conolly et al., 2001). For chondrule rim metal and some of the isolated metals in the matrix a condensation origin was postulated which is related to the evaporation of volatile elements during the molten state of chondrules and inner-chondrule metal. Those rim and isolated metal grains would have condensed from the volatile-enriched gas (Conolly et al. 2001).

Due to the proposed different formation origins, the relationship of the different CR clan chondrite groups remains unclear. In this study, we want to unravel their relationship by *in situ* analyses of trace elements and Fe and Ni isotopes of the metal phases. Furthermore, we aim at gaining additional information on the formation conditions and timescales of metal growth applying chemical and isotopic modelling on zoned metal grains using a code based on MATLAB.

Part III: Relationship of CH, CB, and CR chondrites

3 SAMPLES AND METHODS

We examined polished sections of the CH chondrites Acfer 214, PAT 91546, and Sayh al Uhaymir 290 (SaU 290). For comparison, we studied the CR chondrite Northwest Africa 852 (NWA 852). Chemical and isotopic data of the CB chondrites are taken from part II of this thesis.

3.1 Petrographic description

In the following general petrographic descriptions of CR, CH, and CB chondrites are given based on the examined samples (see above and the previous chapter about CB chondrites). If features are special to only one of the samples, it is noted in the text.

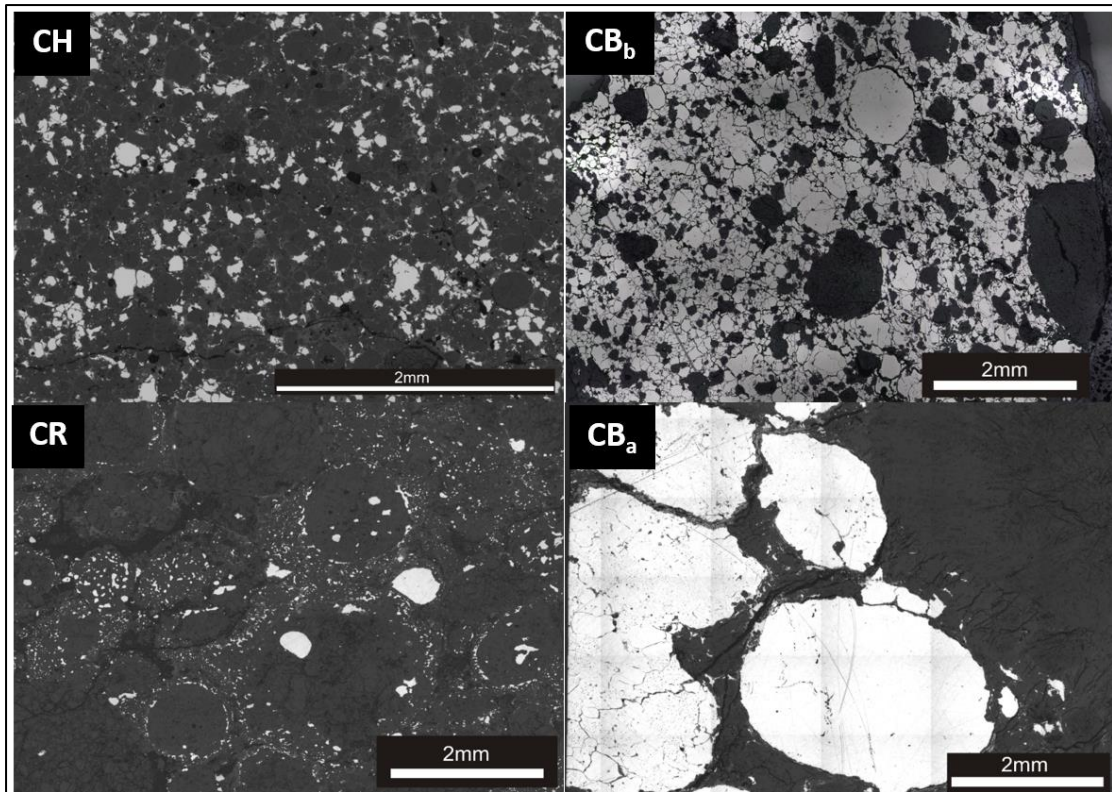


Figure 1: Reflected light images of the typical textures of the four different chondrite groups examined in this study. The main textural difference between CH, CB_a and CB_b is the abundance of metal and the mean grain size. CB_a chondrites have the largest mean grain size and metal is more abundant than in CH chondrites. CB_b chondrites have the same amount of metal as CB_a chondrites but have smaller mean grain sizes. CR chondrites have significantly lower modal abundance of metal than CH and CB chondrites, and metal appears in three different textural setting. As rims around chondrules, within chondrules or as isolated grains. Moreover, the most abundant chondrule type in CR chondrites is the porphyritic one while it is the cryptocrystalline texture in CH and CB_b chondrites. Additionally, CR chondrites contain matrix material, which is not abundant in CH and CB chondrites.

Part III: Relationship of CH, CB, and CR chondrites

3.1.1 CB_a (*Gujba, Bencubbin, NWA 4025*)

CB_a chondrites consist of about 70 vol% metal with grain sizes varying between hundreds of μm up to several mm. Metal grains are often elongated and show a preferred orientation (Rubin et al., 2003). Some cm-sized objects are present. Internal texture reveals that they are composed of several smaller metal grains (up to $600\mu\text{m}$), which are separated by sulfides often forming triple junctions. Those objects are called metal aggregates. Troilites are abundant as small blebs within metal grains, within aggregates as well as in isolated grains. However, sulfide-free metal grains are also present. Though no chondrules were found within the examined sections of CB_a chondrites, the presence of silicate globules within those samples was described in the literature (Weisberg et al., 1995). Such silicate globules were also described in (Rubin et al., 2003) with a maximum diameter of 10 mm and a radial pyroxene (RP) macrochondrule was reported in (Weyrauch and Bischoff, 2012). Rubin et al. (2003) also describe smaller silicate globules ($50\text{-}600\ \mu\text{m}$) with cryptocrystalline (CC), barred pyroxene (BP) or barred olivine (BO) textures. Interstitial to metal and silicates, CB_a chondrites contain some melt veins that are rich in silicate and contain small metal nodules. No fine-grained matrix material or dark inclusions can be found in CB_a chondrites (Weisberg et al., 1995).

3.1.2 CB_b (*HaH 237, QUE 94411, MAC 02675*)

CB_b chondrites mainly consist (up to 70 %) of fine-grained metal ($30\text{-}200\ \mu\text{m}$) that is flaky, crimped, and stacked onto each other. Additionally, some larger metal grains (up to 4mm) are present which constitute of several smaller metal grains (up to $600\ \mu\text{m}$) separated by sulfides. These objects are similar to the metal aggregates found in CB_a chondrites. Zoned metal grains occur in chains or in clusters, but also appear as isolated grains (on average $150\ \mu\text{m}$ in diameter). The modal abundance of zoned metal makes up 10-18 % of the metal fraction of HaH 237, the same can be assumed for other CB_b chondrites. In Ni element mappings, it can be observed that zoning often follows the crimped form of the grains. Moreover, back scattered electron (BSE) images reveal a fine-grained plessitic texture in the center of some zoned metal grains. Interstitial to metal and silicate phases are abundant shock veins and clasts of fine-grained material. Some are dominated by silicate melt and others are dominated by metallic melt. Chondrules are abundant and mainly have CC- and fine-grained barred textures. However, also coarse-grained barred olivine (BO) chondrules appear. Smaller CC chondrules ($20\ \text{to}\ 50\ \mu\text{m}$ diameter) are well rounded. Larger ones are more fragmented and show abundant cracks. The same can be observed for barred chondrules. The latter are larger than CC chondrules with diameters of $200\text{-}500\ \mu\text{m}$, while CC chondrules rarely reach sizes of up to

Part III: Relationship of CH, CB, and CR chondrites

200 μm . Moreover, some barred chondrules are crimped, as has been observed for the metal grains.

3.1.3 CH/CB_b breccia (Isheyevo)

The modal abundance of metal in Isheyevo is 7-90 % in (Ivanova et al., 2008). In our section from Isheyevo metal contents vary between 30 and 60 vol%. Evaluation of a Ni element map of Isheyevo (5*5 mm) revealed that zoned metal makes up about 9 % of the whole metal fraction. Areas with high metal contents (~60 vol%) are those of CB_b lithology. Metal is highly compacted, crimped, and stacked onto each other. Zoned metal is mainly present in clusters or as chains, with grain sizes up to ~300 μm . The dominating chondrule type is of cryptocrystalline texture with sizes of up to ~100 μm . However, rare CC chondrules of ~200 μm are present, too. The areas with metal contents about 30 vol% represent the CH lithology, which is more silicate-rich. Grain sizes of metal and chondrules are somewhat smaller than in CB_b chondrites. Though the mean chondrule size in CH chondrites is ~20 μm (Weisberg et al., 1995), also large silicate clasts of up to 1 mm in diameter are apparent in the CH lithology. There is no sharp boundary between the two different lithologies (Ivanova et al., 2008). Interstitial to the metal grains and chondrules, Isheyevo contains abundant shock veins and clasts of fine-grained material.

3.1.4 CH (Acfer 214, PAT 91546, SaU 290)

In CH chondrites the dominant phase are small rounded silicate grains which range in size between tens of microns up to ~100 μm . Metal mainly occurs as isolated grains but is also present in the form of clusters, wherein metal grains are sometimes loosely attached to each other. Grains are of amoeboid shape, mainly have frayed rims, and look heavily fragmented. Size of metal is up to 300 μm in diameter, average size is 80-100 μm (Bischoff et al., 1993). The modal abundance of zoned metal grains was determined from five Ni element mappings of Acfer 214. Those mappings revealed that zoned metal makes up 7-11 % of the metal fraction. BSE images revealed that a lot of zoned metals show plessitic texture within the centre (see also Goldstein et al., 2007). The most abundant chondrule type is the cryptocrystalline texture. Those chondrules range in sizes between 20 and 200 μm (Bischoff et al., 1993). Smaller ones are well preserved, larger ones (100 μm and larger) often show cracks or are only present as fragments. Barred chondrules are also quite abundant, they are larger (up to 300 μm) than the majority of CC chondrules and mainly are fragmented. Some of those seem to be crimped, like it can be observed for some metal grains. In the examined thin section of PAT 91546 one porphyritic chondrule with a metal ring was observed (Fig. 2), such objects were not found in

Part III: Relationship of CH, CB, and CR chondrites

the other two CH chondrite samples. PAT 91546 is also slightly different from Acfer 214 and SaU 290 in its general texture. Metal in PAT 91546 seems to be more equally distributed than in the other two samples, and also seems to be more frequent. Interstitial to isolated chondrules, sulfides, and metal grains are melt areas of varying sizes. Those are siliceous melts with tiny well-rounded metal blebs inside. Moreover, all CH samples show areas of fine-grained matrix like material (Fig.2).

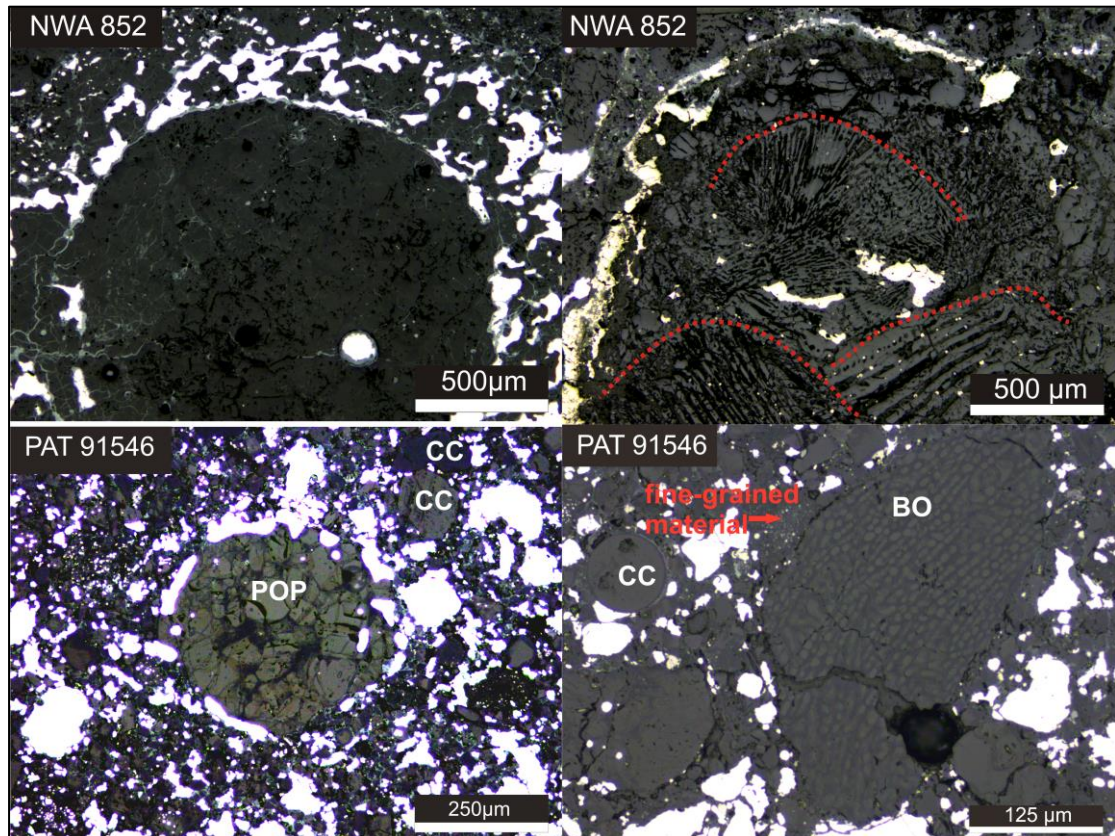


Figure 2: Reflected light images of chondrules from CR chondrite NWA 852 (upper two) and CH chondrite PAT 91546 (lower two). Upper left: A porphyritic chondrule with a metal ring of multiple layers and a metal grain within the chondrule. Upper right: A compound chondrule consisting of at least three radial chondrules with a sulfide rim around. Dashed red lines indicate boundaries of the individual chondrules. Lower left: a rare porphyritic chondrule (POP) with a metal rim from CH chondrite. Cryptocrystalline chondrules (CC) are also apparent. Lower right: a typical cryptocrystalline chondrule (CC) and a fine-grained barred olivine chondrule (BO) from a CH chondrite. Fine-grained matrix-like material is attached to the surface of the deformed BO chondrule.

3.1.5 CR (NWA 852)

CR chondrites have about 7-9 vol% metal (Bischoff et al., 1993; Weisberg et al., 1993). Metal occurs as isolated grains in the matrix, as rims around chondrules or within chondrules (Krot et al., 2002, Fig. 1). Grain sizes are varying strongly. While most metal grains are in μm range, some of the isolated metals can be up to 2 mm in diameter. The majority of the larger isolated grains is rounded. Smaller (tens of microns) isolated metal grains and metal in chondrule rims are of amoeboid shape. Most metal rims around chondrules are simple rings

Part III: Relationship of CH, CB, and CR chondrites

around these spherules. However, some rings are more complex and seem to have some kind of layers (Fig. 2). In the examined section of NWA 852 a multi compound chondrule was found, which consists of at least three chondrules with radial texture and a porphyritic area in the rim region (Fig. 2). Around this object is a sulfide-metal ring (Fig. 2). Such sulfide rims were also described for ordinary chondrites (Merrill, 1920; El Goresy et al., 1981). Metal within chondrules is always well rounded and reaches sizes of $\sim 150 \mu\text{m}$. Chondrules are well preserved and range from $\sim 200 \mu\text{m}$ to mm - size. The most abundant chondrule type is the porphyritic texture (also see Weisberg et al., 1995), but radial and barred chondrules are also present. Interstitial to chondrules and isolated metal grains is fine-grained matrix material.

3.2 Analytical Procedure

In a first step samples were examined optically with a Zeiss Axiophot microscope (Frankfurt) and with a Leica DM4-M microscope (Hannover). For quantitative analyses of the chemical composition of the metal grains in the CH and CR samples, a JEOL Superprobe JXA-8900 electron microprobe was used at the Goethe Universität in Frankfurt. Metals were examined for their Si, Fe, Cr, Ni, S, Co, and P contents at 20 nA and 20 kV with a focused beam. Pure element metal standards were used for Si, Fe, Cr, and Ni. Calibration of P, S, and Co was done with KTiO_2PO_4 , FeS, and CoO, respectively. Matrix correction was made according to CITZAF procedure of (Armstrong, 1995). Element mappings were performed for determination of zoned metal grains. Iron, Mg, Al, Ca, and Ni were mapped on WDX detectors at 60 nA and 20 kV with a dwelltime of 10 ms and an interval of $3 \times 3 \mu\text{m}$.

Metal grains were also examined for their Fe and Ni isotope, and trace element composition. Analyses were performed *in situ* (in Hannover). For isotope analyses a Solstice femtosecond laser was connected to a Thermo Scientific Neptune Plus MC-ICP-MS, for trace elements the laser was connected to a Thermo Element XR SF-ICP-MS. Measurements were performed the same way as described in Part II of this study. Analyses for both isotope systems have accuracy and precision better than 0.1 ‰.

4 RESULTS

4.1 Chemical and isotopic characteristics of metal from CH chondrites

CH chondrites contain zoned and unzoned Fe,Ni-metal grains. In the following chemical and isotopic characteristics of metal are described separately for zoned and unzoned ones.

Part III: Relationship of CH, CB, and CR chondrites

4.1.1 Zoned metal

For Acfer 214 and PAT 91546 three zoned grains each were analyzed for their Fe and Ni isotope compositions. Regarding trace elements, only one zoned grain from Acfer 214 was analyzed because of the small grain size in this sample. In SaU 290 two zoned metals were examined for their isotope and trace element compositions.

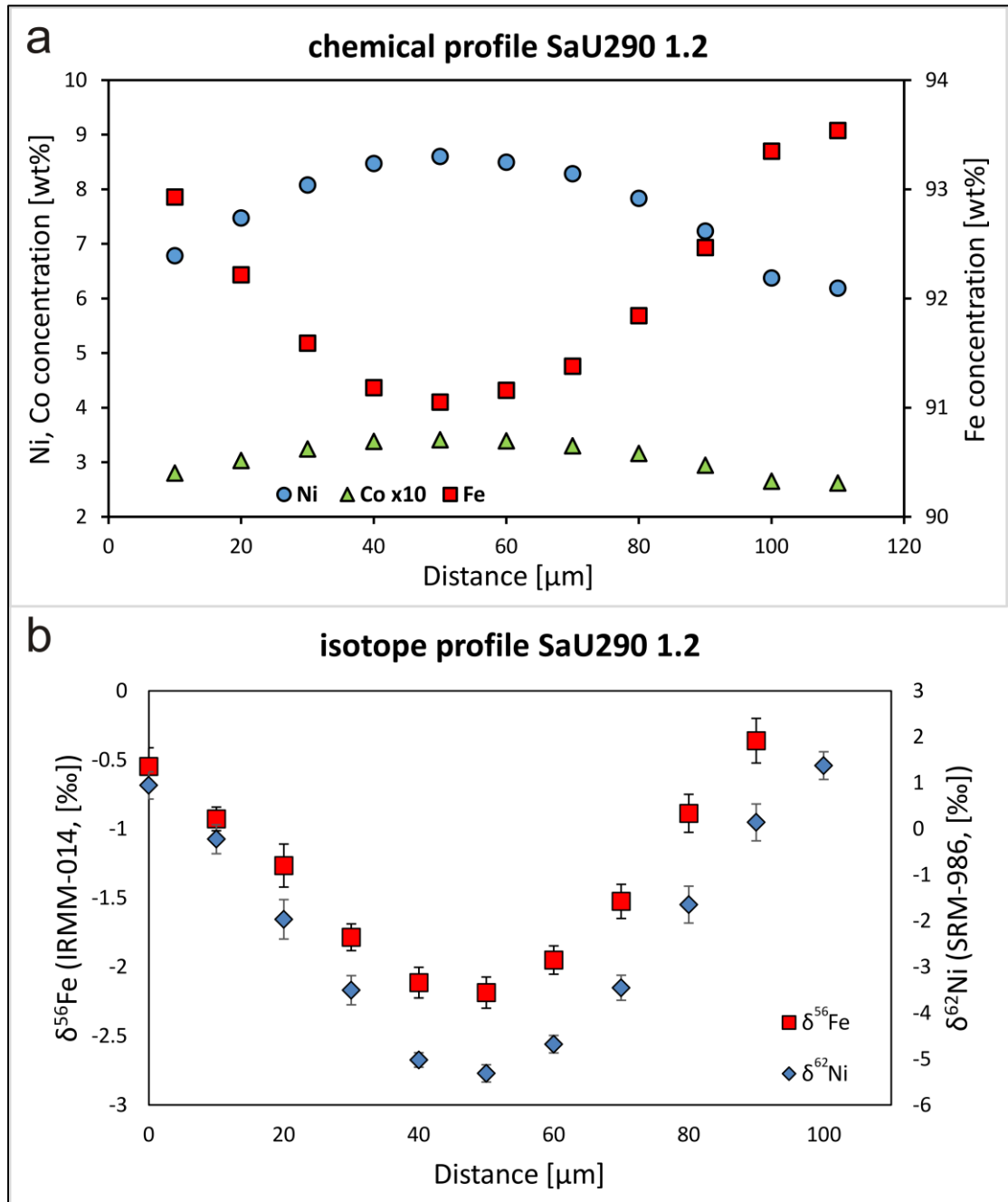


Figure 3: Chemical (a) and isotopic (b) profile of a typical zoned metal grain from CH chondrites. a) major element composition of zoned metal grain SaU290_1.2 with Ni concentration being high in the center of the grain and decreasing towards the rims. Cobalt is following the trend of Ni and Fe is zoned reversely with low concentration in the center and high contents in the rims. b) isotope profile of grain SaU290_1.2, Fe and Ni are zoned parallel to each other with light compositions in the center and heavier composition in the rims.

Part III: Relationship of CH, CB, and CR chondrites

Similar to zoned metal in CB_b chondrites (see part II), zoned metals in CH chondrites have higher Ni contents in the center than in the rims, Cr and Fe concentrations are vice versa with lower values in the core than in rims (Fig. 3a). Refractory elements and Co follow the trend of Ni with higher concentrations in the cores than in the rims. Normalizing trace element compositions to CI values reveals that zoned metals are enriched in refractory elements by a factor of ~10 (Fig. 4). Cores are more enriched than rims. Zoned grains are generally strongly depleted in moderately volatile elements (Au, Cu, Ge). CI-normalized trace element patterns reveal a depletion of Mo and W relative to other highly refractory elements (Fig. 4), with depletion of W being much more pronounced than that of Mo. Those patterns are uniform for all examined zoned grains from the three studied samples.

Isotope composition profiles reveal that Fe and Ni isotopes are lighter in the core regions than in the rims (Fig. 3b). This is consistent with isotope profiles from zoned metal in CB_b chondrites described in part II. The grains with the largest isotope fractionation between rims and core are SaU290_1.1 with ~6 ‰ for $\delta^{56}\text{Fe}$ and ~9 ‰ for $\delta^{62}\text{Ni}$, and grain Acfer_5.3 with ~6 ‰ fractionation for both isotope systems.

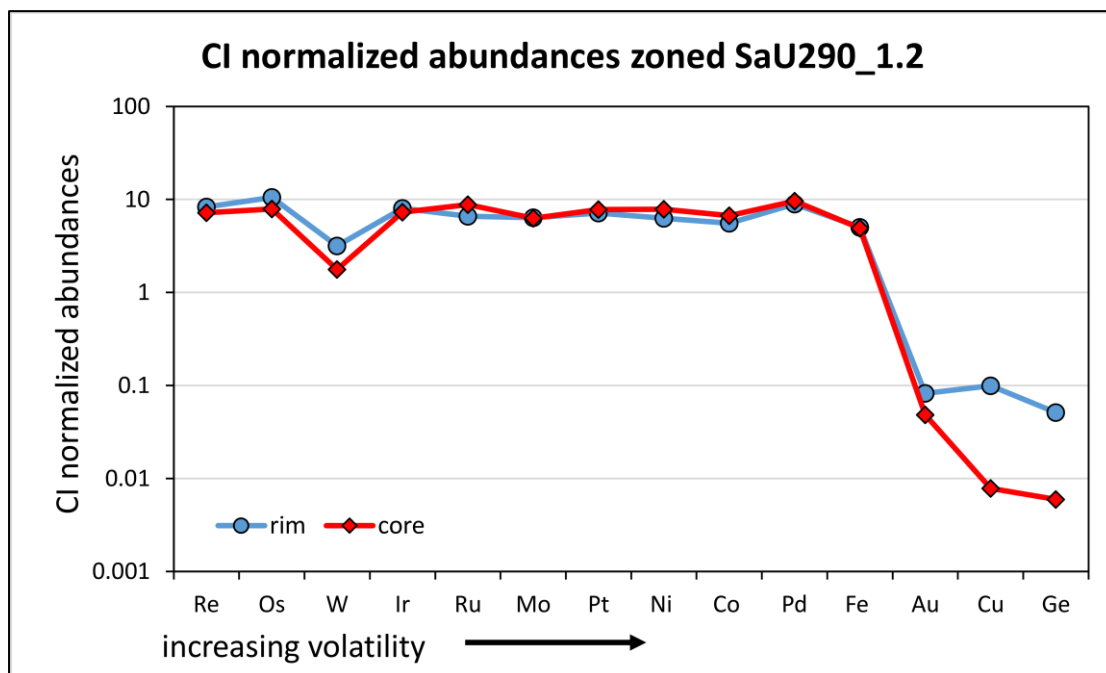


Figure 4: CI normalized values of zoned metal grain SaU290_1.2. Refractory elements are enriched by 7-10 times CI, while moderately volatile elements (Au, Cu, Ge) are depleted relative to solar values. A depletion of W relative to other refractory elements is observable in this grain. This pattern is representative for all zoned metal grains in CH chondrites. Elements are sorted by their 50% condensation temperatures according to (Lodders et al., 2009).

Part III: Relationship of CH, CB, and CR chondrites

4.1.2 Unzoned metal

In SaU 290 six unzoned metals were examined. In Acfer 214 and PAT 91546, four and three grains were analyzed for their Fe and Ni isotope compositions, respectively. However, trace element analyses were only performed on two of the metals from Acfer 214 due to the small metal grain size. Isotope composition in CH chondrite unzoned metal is largely varying (Fig. 5). It seems that PAT 91546 tends to have lighter Fe and Ni isotope compositions than the other two CH chondrites.

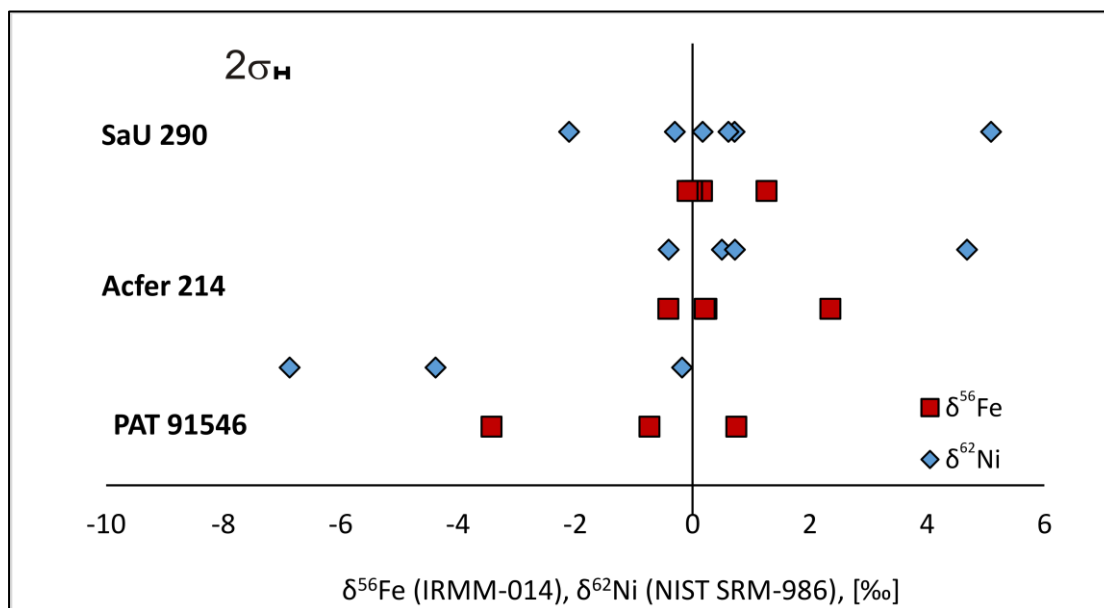


Figure 5: Isotope values of unzoned metal grains from CH chondrites. $2\sigma=0.1\%$.

Trace element compositions normalized to CI values show that unzoned metals are enriched in refractory elements by ~7-10 times the CI values and strongly depleted in moderately volatile elements with the exception of Au. In sample PAT 91546, Au concentrations show a wide range and are enriched by 6-38 times CI, while sample SaU 290 only shows Au contents of 0.5-3 times CI. The two grains examined from Acfer 214 show very similar trace element patterns. Gold contents are 1xCI and 2.5xCI, while their refractory element contents are enriched by 5-7xCI. Grain PAT 91546_4.3 is the only grain depleted in highly refractory elements (Os and Re). This grain also has the highest Au contents and also shows strongly positive anomalies of Mo and W, with an enrichment of 63xCI and 151xCI, respectively. Molybdenum and W concentrations are varying in SaU 290, some grains show a depletion relative to other refractory elements, while others show flat patterns or slight enrichments in those elements relative to other refractory elements. While the majority of the grains show uniform patterns, except for Mo and W, one grain stands out. Grain SaU 290_1.3

Part III: Relationship of CH, CB, and CR chondrites

is depleted in the refractory elements Re, Os, Ir, and Pt but shows higher abundances of the elements Mo, W, and Ru.

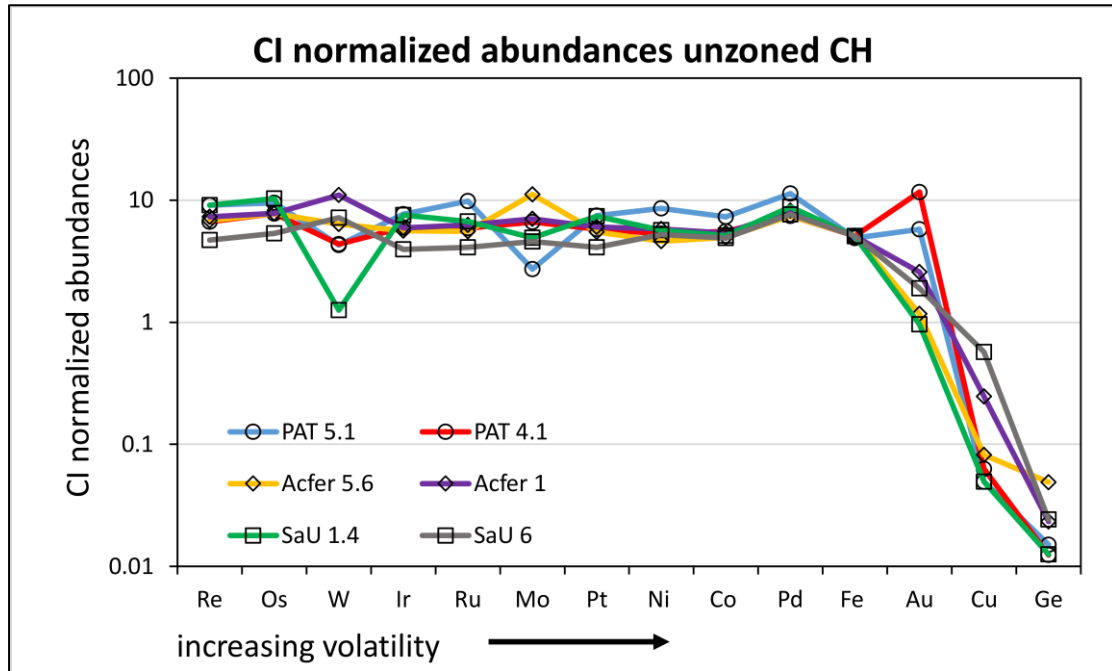


Figure 6: CI normalized values of a selection of “common” unzoned metal grains from CH chondrites. The grey line represents grain PAT_4.3, which shows divergent element abundances. It appears that refractory elements are enriched by 7-10 times the solar value, and that moderately volatile elements are depleted. It is also obvious that trace element compositions are variable among the metal grains, as some grains show higher Au values than others, and since some unzoned metal grains are depleted in W and Mo relative to other refractory elements. Other grains do not show such a depletion or are even enriched in W and Mo relative to other refractory elements. Elements are sorted by their 50% condensation temperatures according to (Lodders et al., 2009).

4.2 Chemical and isotopic characteristics of metal from CR chondrites

CR chondrites only contain unzoned metal. Since we only had one CR chondrite sample available, supporting data from the literature are added for trace element composition of metal from CR chondrites. No Fe isotopic data for CR chondrite metal were found in the literature, thus we present the first Fe isotope data for CR chondrite metal. Nickel isotope data were only found for Renazzo (Cook et al., 2007; bulk metal data).

Seven metal grains in NWA 852 were examined for both, Fe and Ni isotope compositions as well as for trace element concentrations. The investigated metals are either inclusions in chondrules, or isolated grains. Additionally, two small grains could only be analyzed for their Fe (NWA 852_11) or Ni (NWA 852_12) isotope composition, respectively. Both grains are located in a complex cauliflower-like metal ring around a chondrule.

Both, $\delta^{62}\text{Ni}$ (0.16 to 1.09 ‰) and $\delta^{56}\text{Fe}$ (-0.34 ‰ to 0.64 ‰) show, compared to unzoned grains from CB and CH chondrites, limited, but still significant variability in the metal from NWA 852. Figure 7 reveals that Ni concentrations are highest in inner chondrule metals. Those

Part III: Relationship of CH, CB, and CR chondrites

also tend towards heavier Fe isotope compositions. However, all metal, except one, overlap within uncertainties in Fe isotope values. Nickel isotope composition of the metals is more variable than Fe isotope composition and no correlation with the Ni concentration can be observed. There is no correlation of the isotopic composition with the textural setting of the metal grains (Table 1). However, Figure 7 also shows that the isotope composition in isolated metal seems to be related with the Ni content. Fe isotope composition is heavier in the grains with high Ni contents than in those with lower Ni concentrations. The correlation of the Ni isotope composition with the Ni concentration is not as pronounced as the correlation with the Fe isotope composition. Nonetheless, it appears that $\delta^{62}\text{Ni}$ values are lighter in the grains with high Ni concentrations.

Table 1: Isotope composition and major element concentrations of metals from CR chondrite NWA 852. It appears that the isotopic composition is not correlated with the textural setting. However, metal that sits within chondrules has higher Ni and Co values than isolated metal. NA = data not available.

Grain	Textural setting	$\delta^{56}\text{Fe}$ [‰]	$\delta^{62}\text{Ni}$ [‰]	Ni [wt%]	Co [wt%]
NWA1	in chondrule	0.64	0.17	7.73	0.36
NWA2	Isolated	-0.33	1.01	5.76	0.27
NWA3	isolated	-0.25	0.55	5.51	0.26
NWA5	Isolated	-0.17	0.60	6.10	0.28
NWA6	Isolated	-0.23	0.16	6.17	0.28
NWA7	in chondrule	-0.10	0.23	8.24	0.36
NWA8	Chondrule rim	NA	NA	5.34	0.24
NWA9	Isolated	-0.34	1.09	5.22	0.25

Literature data for Ni isotope composition of CR chondrite metal is only available for Renazzo (Cook et al., 2007) with $\delta^{62/58}\text{Ni} = 0.58$ ‰ (which corresponds to $\delta^{62/60}\text{Ni} = 0.29$ ‰), this value is in the range of Ni isotope values measured for NWA 852 and may suggest that CR chondrites have only limited isotopic variation between the single meteorites.

Major and trace element analyses, were performed on nine metal grains from NWA 852. Nickel content in the grains is varying from 4.9 wt% up to 8.2 wt%, Co ranges between 0.24 wt% and 0.36 wt%. Nickel and Co commonly are positively correlated. Grains with high Ni concentrations also have high Co contents. The two grains from within chondrules (NWA852_1 and NWA852_7) have significantly higher Co and Ni contents than the majority of the chondrule rim or isolated grains of this chondrite. Normalizing element contents to CI values (Figure 8) reveals that refractory elements are enriched in the majority of grains by a factor of ~5-7xCI. However, two grains show a somewhat different pattern in refractory elements: NWA852_1 (within chondrule) shows an enrichment in refractory elements by a factor of ~23, and in NWA852_8 (chondrule rim) those elements are only enriched by a factor of ~3.

Part III: Relationship of CH, CB, and CR chondrites

Additional data for metal grains from ten CR chondrites were taken from Jacquet et al. (2013). Nickel contents from NWA 852 fall into the same range that was observed in the literature. Most grains from the literature are also consistent with the trace element abundances found in NWA 852, significantly higher contents are the exception.

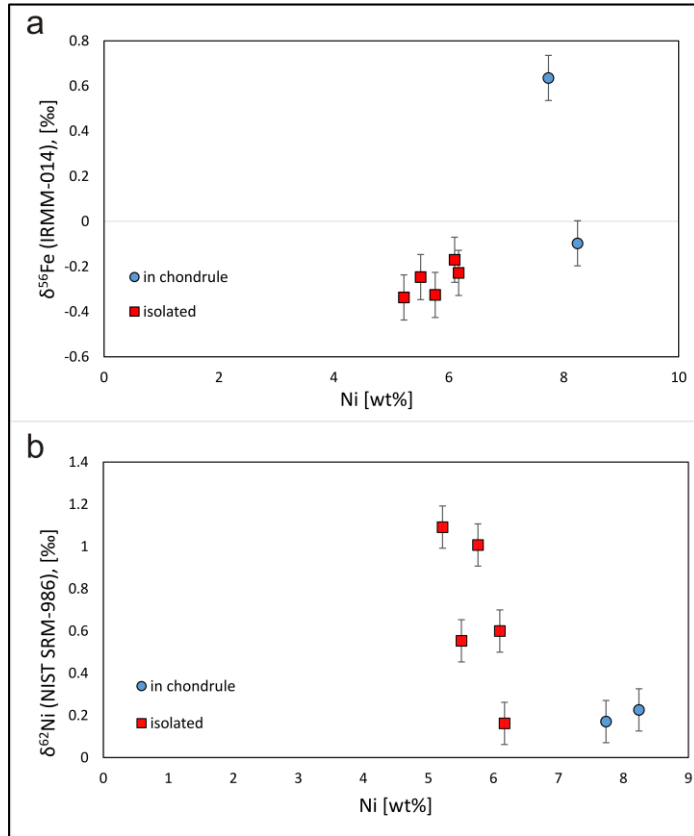


Figure 7: Fe isotope composition (a) and Ni isotope composition (b) plotted against the Ni element content of metal from CR chondrite NWA 852. The range of Fe isotope compositions is very narrow, only one inner-chondrule metal grain shows significantly heavier compositions. However, there seems to be no general correlation of the textural setting and the composition of the metal. Only Ni contents appear to be higher in inner-chondrule metal than in isolated metal.

CI normalized abundances of the data from Jacquet et al. (2013) show similar patterns as the data derived for NWA 852. In the majority of metal grains, the refractory elements are enriched by about $\sim 5\text{-}7\times\text{CI}$ (Fig. 8). However, there are some exceptions with significantly higher or lower contents in refractory elements (see supplement of Jacquet et al., 2013).

Part III: Relationship of CH, CB, and CR chondrites

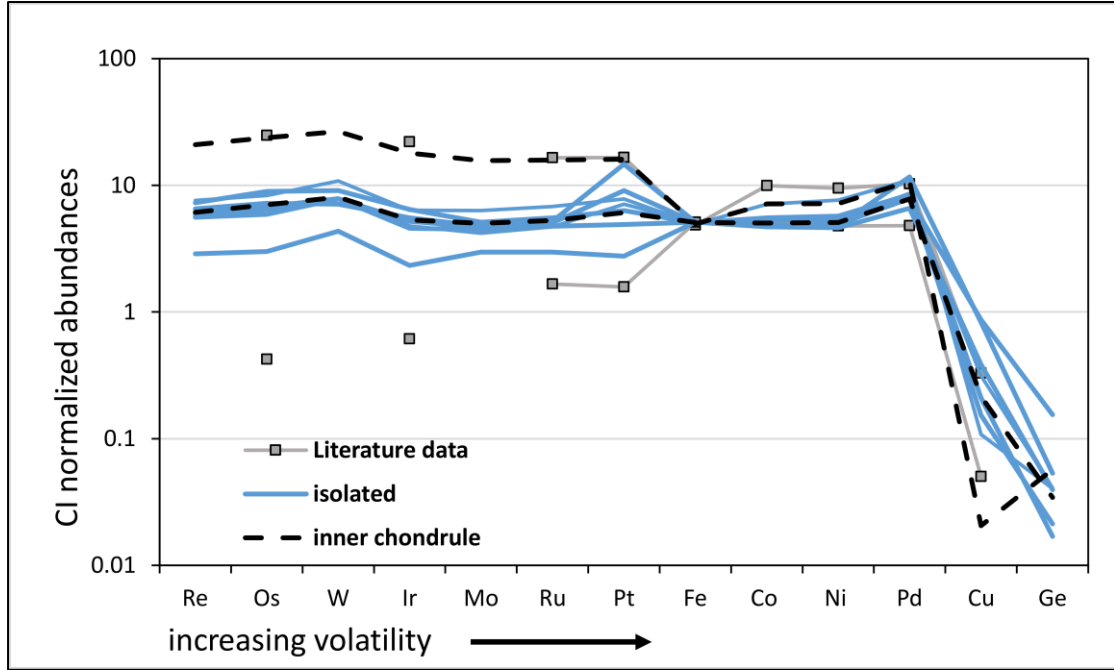


Figure 8: CI normalized abundances of metal from CR chondrite NWA852. Dashed lines represent metal that is located within a chondrule, blue lines represent isolated metal. Grey squares represent the most extreme abundance patterns for CR chondrites found in Jacquet et al. (2013). Values from the literature and from this study show that metal from CR chondrites is enriched in refractory elements by 5-10 times CI and depleted in moderately volatile elements (Au, Cu, Ge). It seems that trace element variability of metals within an individual sample is similar to that observed among the different CR group meteorites. Unlike commonly observed in CB and CH chondrites, W and Mo (only this study, a) do not show a depletion relative to other refractory elements, but rather W shows a slight enrichment. Elements are sorted by the 50% condensation temperature according to (Lodders et al., 2009).

4.3 Isotopic and chemical similarities and differences of CR, CB, and CH chondrites' metal

Zoned metal from CB_b and CH chondrites are isotopically similar to each other. In both chondrite types Fe and Ni isotope zoning is parallel with lighter composition in the cores than in the rims. Plotting core and rim compositions ($\delta^{62}\text{Ni}$ vs Ir, Fig. 9a) of CB_b and CH together, reveals that cores and rims have variable compositions. Two evolution trends of zoned metal grains in CB_b chondrites were found in part II of this thesis. Group I has cores with lower Ir concentrations and light Ni isotope compositions and evolve towards heavier isotope compositions while Ir content is scarcely changing. Cores of CB_b grains display a significant positive correlation of $\delta^{62}\text{Ni}$ and Ir ($R^2 \approx 0.8$, excluding 2 of 12 cores that may not reflect real core values due to cutting effects). Group II metal grains have higher Ir and heavier Ni isotope compositions in the cores than associated rims. Rim compositions are similar to the rims of group I grains. Examined zoned grains from CH chondrites mainly follow the evolution trend of group I. However, Ni isotope compositions of the cores of CH grains are slightly heavier than those of group I cores from CB_b chondrites and are more similar to the isotope compositions of group II cores from CB_b chondrites. The evolution trend of group I grains

Part III: Relationship of CH, CB, and CR chondrites

suggest formation by fractional condensation in a fast-cooling reservoir leading to predominantly kinetic condensation causing high degrees of isotope fractionation towards negative $\delta^{62}\text{Ni}$ and $\delta^{56}\text{Fe}$ (higher than in group II). The dominance of group I zoned metal in CH chondrites, may indicate that formation of zoned metal under rapid cooling rates was favored contrary to formation of zoned group II metal which likely represent a mixture of equilibrium and kinetic condensation.

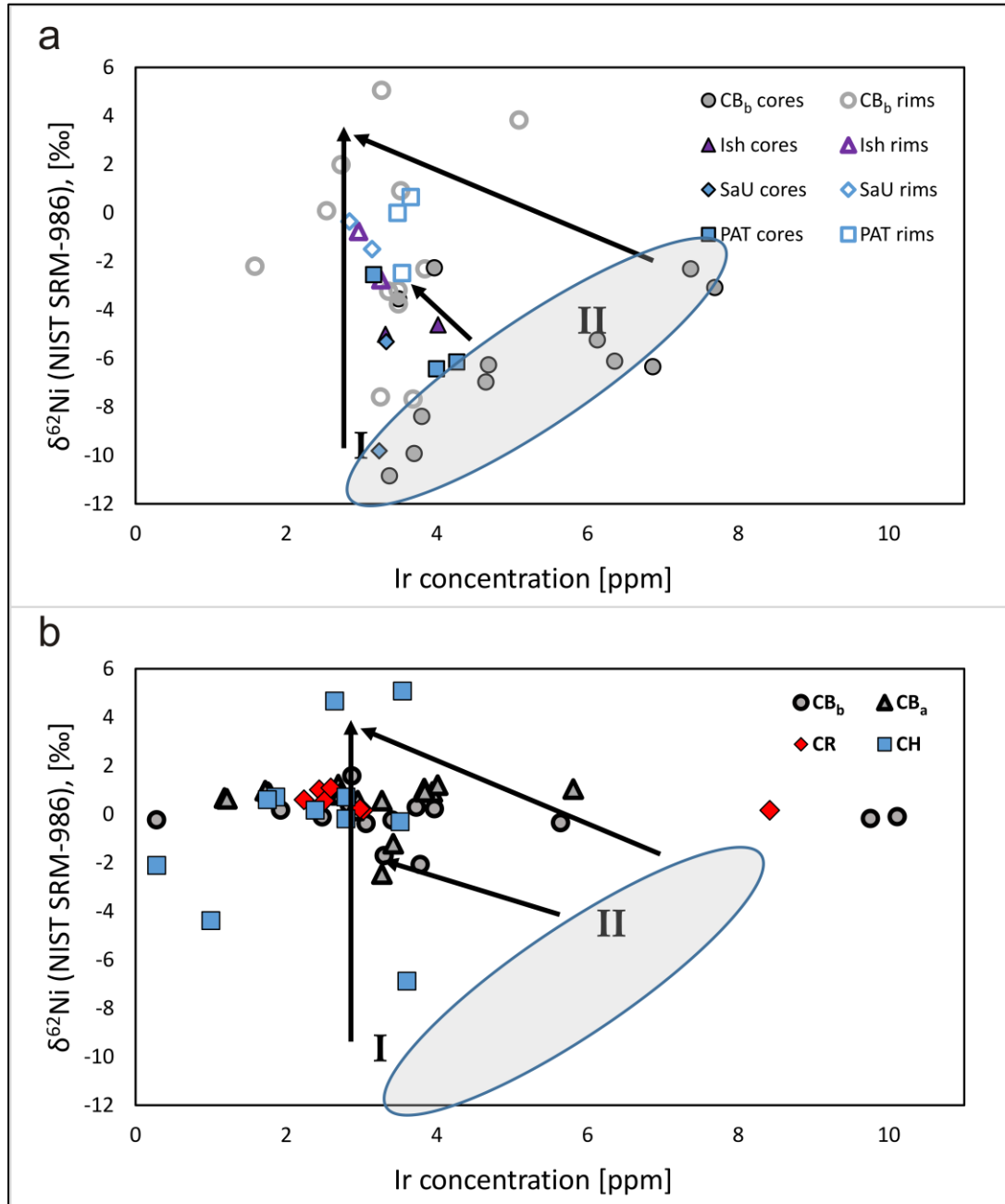


Figure 9: Plots of Ni isotope composition vs Ir concentrations of (a) zoned metal grains from CH and CB_b chondrites and (b) unzoned metals from CH, CB, and CR chondrites. a) shows that zoned metal from CH chondrites rather fall into group I while CB_b zoned metals fall into both groups. b) reveals that unzoned metal from CH chondrites show larger isotopic variations than CB and CR chondrite metal, but that the majority of unzoned metal from all three meteorite groups plot in a relatively narrow range of 0 ± 2 ‰ (with two exceptions lying at 4.4 ‰ and 5.8 ‰). Blue fields show the correlation trend of Ir concentration and Ni isotope composition of the cores of zoned metal.

Part III: Relationship of CH, CB, and CR chondrites

Unzoned metal from CH, CB, and CR chondrites show different variability in their isotopic and chemical composition (Fig. 9b). CR chondrite metal display a much smaller range than unzoned metal from CH or CB_b chondrites both in the isotope composition (Fig. 10) and in the Ir content (Fig. 9b). Only one metal grain from NWA 852 shows significantly higher Ir concentrations than the rest of metal from that sample. This is grain NWA852_1, which also has the heaviest Fe isotope composition (Figs. 7a and 10) and is located within a chondrule. Though CB_a metal has also quite narrow isotope compositions, Ir contents are more varying. Unzoned metal from CH and CB_b chondrites fall in about the same range of isotopic values. Zoned metal grains from CH and CB_b chondrites, as well as the majority of unzoned grains from those meteorites, and the unzoned grains from CB_a chondrites, display a positive correlation of Fe and Ni isotope composition (Fig. 10). Such correlation of the two isotope systems is not observed for metal from CR chondrites.

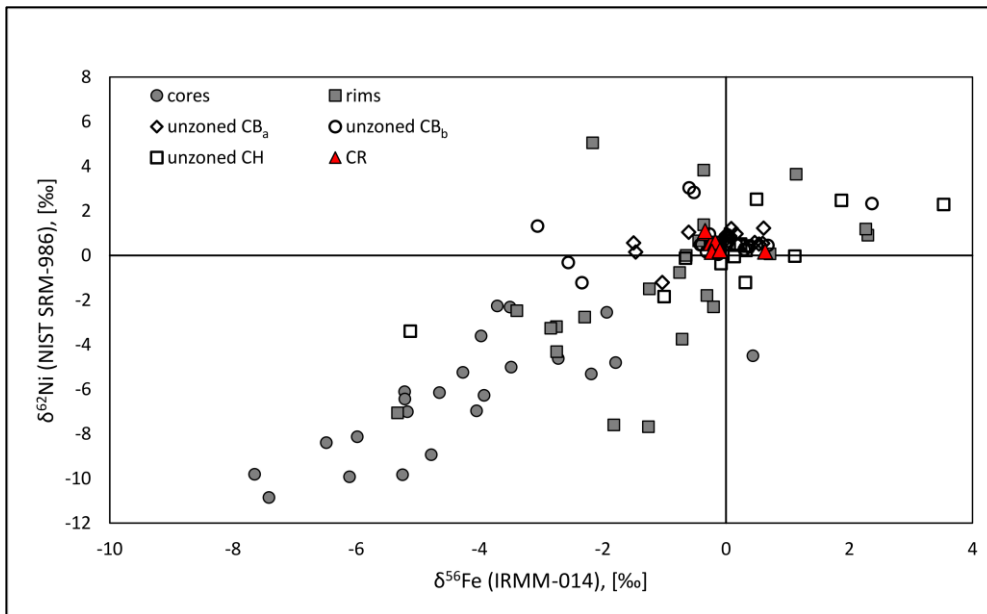


Figure 10: Plot of Ni isotope composition vs Fe isotope composition of examined metal from CH, CB, and CR chondrites. Zoned metals from CH and CB_b chondrites (in particular the cores) display a positive correlation. Unzoned metal from CH and CB chondrites crudely follow this trend. Such correlation is not observable for metal from CR chondrites.

Zoned metal grains from CH and CB_b chondrites show the same zoning patterns of highly siderophile refractory elements (HSRE) with mainly higher concentrations in the grain center and decreasing contents towards the rims. In both meteorite types also rather flat patterns appear. Those mainly affect Ir and Os, Ru mostly keeps following the zoning of Ni and Co, with high contents in the center and lower ones at the rims. Zoned metal from both CH and CB_b chondrites are enriched by 7-15 times CI in refractory elements, and are depleted in moderately volatile elements such as Ge, Cu, and Au. Cores are more enriched in refractory elements than rims. For zoned metal from CB_b chondrites a relative depletion of W and Mo relative to other

Part III: Relationship of CH, CB, and CR chondrites

refractory elements was observed, which is more pronounced for W than for Mo (see part II). Such a negative W and weaker negative Mo anomalies are also apparent in zoned metal from CH chondrites.

Unzoned metal from CH, CB and CR chondrites are very similar in their major element composition. They all display a positive correlation of Co and Ni with solar ratio. Moreover, trace element compositions in unzoned metals from the different meteorite groups show similar CI normalized abundance patterns: with enrichment of refractory elements by 5-10 times and depletion of moderately volatile elements. The depletion of Mo and W relative to other refractory elements observed in zoned metals from CH and CB_b chondrites, is rarely apparent in unzoned metal from CH, CB and CR chondrites. Molybdenum and W sometimes even show a slight enrichment relative to other refractory elements.

5 DISCUSSION

For metal from CH and CB chondrites a condensation origin was suggested (Meibom et al., 1999; Weisberg and Prinz, 1999; Campbell et al., 2005). The setting for such a condensation process is highly debated as some groups propose condensation in the solar nebula (Weisberg and Prinz, 1999) and others set condensation within an impact-induced vapor plume (Wasson and Kallemeyn, 1990; Fedkin et al., 2015). The Fe and Ni isotope composition, and trace element concentration in metal of CB chondrites were analyzed in part II, and results support an origin of CB chondrite metal in an impact plume. Other studies also suggest a condensation origin from a gas of solar composition for CR chondrite metal, based on the depletion in moderately volatile elements and the Ni-Co correlation (Weisberg et al., 1993; Campbell et al., 2005). However, this is controversially discussed as other research groups (Lee et al., 1992; Zanda et al., 1994) interpret these characteristics to be due to redox processes. In contrast to CH and CB metal, CR chondrite metal formation is proposed to be closely linked to chondrule formation.

In the following we discuss the possible formation models and relationship of the CR clan chondrites.

5.1 Formation conditions and relationship of CB and CH chondrite metal

Former studies already discussed that isotopic and chemical composition of zoned and unzoned metal from CB and CH chondrites are consistent with a condensation origin (Campbell et al., 2005). It was previously shown that compositional data of CH and CB chondrites suggests condensation from an impact-induced vapor plume (Wasson and Kallemeyn, 1990; Kallemeyn et al., 2001; Fedkin et al., 2015; and part II of this thesis). In such a scenario, zoned metal

Part III: Relationship of CH, CB, and CR chondrites

condensed in the outer shell of the plume under fast cooling rates with dominantly kinetic isotope fractionation. Unzoned metal formed in the slow-cooling interior of the plume under more equilibrium-like conditions (see part II). Since zoned and unzoned metal from CH chondrites are very similar to CB chondrite metal, both in their isotopic and chemical composition, a common formation process for metals from CH, CB_a, and CB_b chondrites can be postulated (Figures 8, 9, 10). The main textural difference between CH, CB_b and CB_a chondrites is the mean grain size. This could be caused by grain size sorting, which could have occurred due to interstellar shock waves (Clayton, 1980) or X-winds (Krot et al., 2001) that pushed material out of the formation region. In this scenario, small grains would have been transported further than large grains. Grain size sorting would also explain the lack of zoned metal grains in CB_a chondrites, as zoned metal grains are rather small with 80-300 μm in diameter. This is by more than a magnitude smaller than the mean grain size in CB_a chondrites (0.4-7mm, Rubin et al., 2003). Another difference between CH and CB_b chondrites is, that plessitic textures in the cores of zoned grains are more abundant in CH than in CB_b chondrites. This suggests different shock histories of CH and CB_b chondrites and may indicate that CH and CB_b chondrites do not derive from a common parent body.

5.2 Modelling of formation conditions of zoned metal from CH and CB_b samples

To gain more information on the conditions and timescales of zoned metal formation in CH and CB_b chondrites, modelling of isotope and chemical zoning were performed with a MATLAB code specifically written for that purpose. Conditions and time scales of metal growth are estimated by fitting chemical and isotopic zoning profiles, that were modeled with variable boundary conditions, to those observed in the samples. The algorithm includes cooling constant (1/s), the volume (m³) of the gas the grain formed from, the total pressure of the gas (bar), and beginning (1473 K, condensation temperature of Fe,Ni-metal (Krot et al., 2009)) and end temperature (400 K) of the condensation process. The partial pressure of Fe and Ni isotopes is being newly calculated for every time step (deltat=10000 s) of the formation process. This is done by mass balance calculation of the gas reservoir and the increasing radius of the growing grain. Calculations are only considering growth of one grain from a specific volume. A gas of solar composition is assumed from which one grain grows from a nuclei of 1 nm. The three factors mostly controlling the shape of the modeled zoning profiles are the volume of the gas, the total pressure of the gas and the cooling constant.

First results reveal that the first condensates show a strong Ni concentration peak in the center of the grain and evolve into a small plateau area before they decrease (Fig. 11a). Fe and Ni isotope patterns start with values below 0 ‰ evolving to lighter values and getting heavier

Part III: Relationship of CH, CB, and CR chondrites

in the rim regions. (Fig. 11b). This evolution is similar to the trends observed in grain HaH237_10.5 which is also the largest zoned grain found in this study. Thus, this grain may represent the earliest metal that formed from the impact plume. The other zoned grains, which have bowl-shaped isotope patterns, with light isotopes in the cores and heavier ones in the rims, may represent later condensates. They are congruent with the evolution of the zoning found in the flanks and rims of HaH237_10.5.

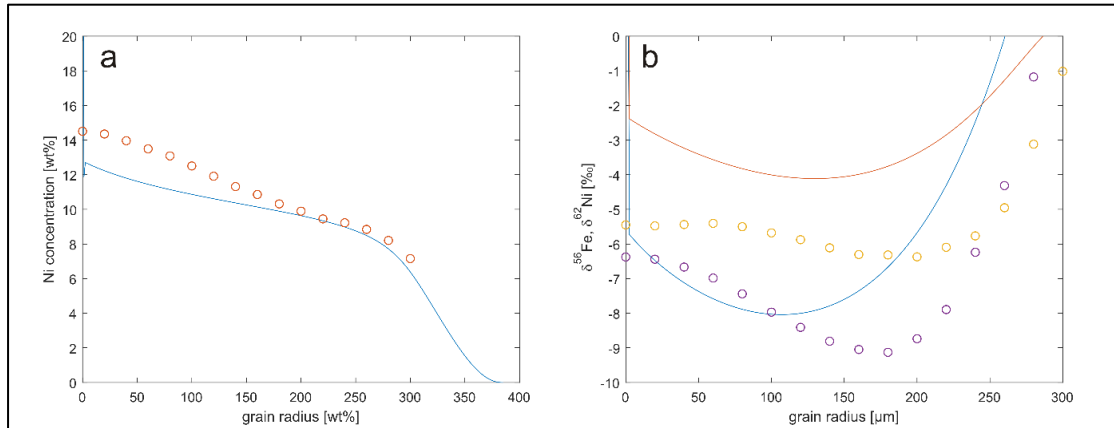


Figure 11: Modeled and measured chemical (a) and isotopic (b) zoning of zoned metal plotted against the grain radius with 0 μm denoting the grain center. a) circles represent the measured Ni concentration zoning in metal grain HaH_10.5, the blue line represents the fitted model. b) circles represent measured isotope values (yellow = $\delta^{56}\text{Fe}$, purple = $\delta^{62}\text{Ni}$), lines represent modeled isotope zoning (red = $\delta^{56}\text{Fe}$, blue = $\delta^{62}\text{Ni}$). Modeled and measured values do not perfectly fit due to the lack of diffusive changes during grain growth in the model algorithm. However, Fe isotopes are less strongly fractionated than Ni isotopes in measured and modelled zoning and show overlapping in the rim regions. For the fitted model a total pressure of $1 \cdot 10^{-3} \text{ bar}$, a total volume of 55 m^3 , a cooling constant of $1 \cdot 10^{-8} \text{ (1/s)}$, and $\text{deltat} = 10000 \text{ (timestep in s)}$ were assumed.

Since the MATLAB algorithm does not include diffusion processes yet, it is not possible to fit the model well enough with the measured zoning patterns to give substantiated information on the formation conditions of zoned grains, such as cooling rates. However, the here fitted model gives a cooling rate of 0.02 K/h (Fig. S1). This rate may change after inclusion of diffusion into the calculation.

5.3 Possible formation conditions of CR chondrite metal

Chemically, unzoned metal from CR chondrites is very similar to unzoned metal from CH and CB chondrites (Figures 5, 8, 9, 10). The depletion of moderately volatile elements relative to the solar value and the enrichment in refractory elements relative to CI, as well as the Ni-Co correlation, is consistent with a condensation origin (Weisberg et al., 1993; Campbell et al., 2005) as it was suggested for metal from CB and CH chondrites. However, it was also proposed that those signatures might be caused by redox processes (Lee et al., 1992; Zanda et al., 1994). In contrast to unzoned metal from CH and CB chondrites, metal grains from CR chondrites show rather homogenous isotopic values that scatter closely around 0 ‰. This

Part III: Relationship of CH, CB, and CR chondrites

indicates that reservoir effects did not play such a significant role during formation of the metal, as it was the case in the formation of CH and CB chondrite metal. The isotopic differences in combination with the textural differences, suggest that CR metal had a different origin than CH and CB chondrite metal. The majority of metal in CR chondrites is associated with chondrules, either as metal inclusions or as rims around chondrules. Thus, metal formation in CR chondrites was likely coupled with chondrule formation, as it was already discussed in former studies (Campbell et al., 2005, and references herein).

Depletion in moderately volatile elements and enrichment in refractory elements is best explained by fractional condensation, at high temperatures. Since metal in CR chondrites is closely associated with chondrules, it seems likely that the metal was already present in chondrule precursor material, or was incorporated during melting of chondrule precursors, in which metal and silicate melts would have been immiscible (see also Conolly et al., 2001). The well-rounded shape of metal inclusions in chondrules, and the lower Fe content compared to that in isolated metals, may be explained by metal-silicate equilibration. Zanda et al. (2002) observed a positive correlation between the melting degree of the chondrules and the Ni content of the metal inclusions. Thus, a heating event could be responsible for this process, as earlier proposed by Jacquet et al. (2013). During that phase, oxidation and evaporative loss of Fe is assumed to occur in the chondrules (Jacquet et al., 2013).

This model does not only explain the chemical signature of CR metal, which is consistent with a condensation origin, but also provides an explanation for the association of metal with chondrules and the equilibrated isotope composition of metal.

Variability of trace element and isotope compositions of CR chondrite metal grains may derive from minor reservoir effects during the condensation of the precursor material, or for inner chondrule metal from metal-silicate equilibration. Thus, condensation occurred more likely in the solar nebula than being associated with an impact induced vapor plume, as reservoir effects are large in the latter (see variability in CH and CB chondrite metal).

5.4 Possible relationship of CR, CB, and CH chondrites

Though constituents of CR chondrites have a different origin than those of CH and CB chondrites, similarities in Cr, N and O isotope composition (Weisberg et al., 1995; Clayton and Mayeda, 1999; Krot et al., 2002; Warren, 2011), and the occurrence of hydrated clasts (Weisberg et al., 1995; Greshake et al., 2002) within the meteorites imply a relationship between the different chondrite groups. Chromium and Ti isotope compositions reveal a dichotomy between carbonaceous meteorites and non-carbonaceous meteorites (Trinquier et al., 2009; Warren, 2011). Due to that, formation of carbonaceous chondrites is supposed to have

Part III: Relationship of CH, CB, and CR chondrites

occurred in the outer solar system, farther out than formation of other chondrite groups (Warren, 2011). In an $\epsilon^{54}\text{Cr}$ vs. $\Delta^{17}\text{O}$ space (Fig. 2 in Warren (2011)), CB chondrites plot closest to CR and CM chondrites, while other carbonaceous chondrites plot towards heavier or lighter values on the carbonaceous trend line. The isotopic similarities of CB and CR chondrites are further supported by N isotope compositions, which separate the metal-rich chondrite groups from other chondrites, including CM chondrites. The N isotope composition of CH ($\delta^{15}\text{N}\approx 550\text{-}850\text{‰}$) and CB ($\delta^{15}\text{N}\approx 500\text{-}1000\text{‰}$) chondrites is more similar than that of CR chondrites ($\delta^{15}\text{N}\approx 150\text{-}200\text{‰}$), which is isotopically lighter than that of CH and CB chondrites (Fig. 6 from Weisberg et al., 1995). Nonetheless, all three meteorite groups have significantly heavier N isotope composition than other chondrite groups ($\delta^{15}\text{N}$ up to 100‰, Weisberg et al., 1995). Moreover, due to Cr-Mg isotope systematics in metal-rich carbonaceous chondrites (CH, CB, CR), it is postulated that they were isolated from other carbonaceous chondrites during their formation (Van Kooten et al., 2016).

Since it is unlikely that CR chondrite components have formed in the same process as constituents of CB and CH chondrites, the isotopic similarities may derive from accretion in areas with akin compositions. Heavy N isotope composition of CH, CB and CR chondrites may support this, as those are supposed to be preserved by colder conditions as present in the outer solar nebula (Van Kooten et al., 2016) where metal-rich chondrites may have accreted. Another possible explanation for the isotopic similarities of CH, CB, and CR chondrites is, that their precursor material was formed in the same region. It is also possible that a CR chondrite was one of the impactors causing the vapor plume. In this scenario, isotopic similarities would be inherited from the impactor by CH and CB chondrites. As reported ages for CR chondrites are older than those for CB chondrites (Kleine et al., 2005; Budde et al., 2018), this might be a possible scenario. Fedkin et al. (2015) also suggest a CR chondrite-like body to be involved in the formation process of CH and CB constituents.

6 CONCLUSION

Isotopic and trace element compositions of zoned and unzoned metal grains from CH and CB chondrites are very similar and suggest a common formation origin. This most likely is condensation from an impact-induced vapor plume, whereas zoned metal formed in the fast-cooling outer regions and unzoned metal under more equilibrium-like conditions in the slow-cooling inner regions. Main differences between CH and CB chondrites are the different mean grain sizes. Those most likely originate in grain size sorting, which would also explain the lack of zoned metal in CB_a chondrites, as zoned metal grains are much smaller than the mean grain size of that meteorite group. For CR chondrite metal, a different formation process needs to be

Part III: Relationship of CH, CB, and CR chondrites

assumed, as isotopic composition is much more homogeneous in CR chondrites than in CH and CB chondrites. The variations in unzoned metal from the latter groups, can be explained by reservoir effects that are likely to appear in an impact plume. As CR chondrite metal lack such variation, a nebular condensation origin is being proposed. Small isotopic variations may be explained by metal-silicate equilibration reactions during heating events associated with chondrule formation.

Considering such different formation processes for CH and CB chondrites, and CR chondrites, the similarities in the Cr, Ti, N and O isotope compositions and other compositional similarities must be unrelated to the formation process of the metals, but rather related to a common precursor material. We suggest that similarities may derive from accretion of those meteorite types in a region of the solar nebula with similar Cr, Ti, N and O isotope composition or that those isotope signatures in CH and CB chondrites are inherited from a CR chondrite impactor.

Part IV: Evidence for the formation conditions of cryptocrystalline chondrules from CH and CB_b chondrites from their trace element composition

Trace element data for this chapter were obtained in the course of the project thesis of Max Winkler.

1 ABSTRACT

CB and CH chondrites are special among the undifferentiated meteorites due to characteristics that hint towards formation in an impact-induced vapor plume rather than a solar nebula process. Metal from these chondrite groups is already well examined and their chemical and isotopic compositions support formation from an impact plume. Chondrules from CB chondrites were found to be younger than chondrules from other meteorite types. Moreover, a condensation origin is proposed for those chondrules, and some studies suggest an impact plume to be the setting for the formation of those chondrules. Here, we examine cryptocrystalline chondrules from two CH and three CB_b chondrites, as well as from CH/CB_b breccia Isheyevo. Trace element abundances were determined by LA-SF-ICP-MS, and Si isotope compositions of eight chondrules were also determined in situ, by LA-MC-ICP-MS. CI normalized trace elements show abundance patterns with volatile elements being generally depleted. Refractory element abundances, however, reveal two different populations among the CC chondrules. One population has superchondritic abundances with flat patterns of refractory elements. The other population, shows generally subchondritic element abundances and fractionated refractory element patterns. The enrichment in refractory elements in superchondritic chondrules suggests a condensation origin as it was already proposed for barred olivine (BO) chondrules in the literature. Those BO chondrules and the superchondritic CC chondrules condensed early from an unfractionated gas reservoir. CC chondrules with chondritic to subchondritic refractory element abundances show fractionated patterns that are

Part IV: Formation conditions of CC chondrules

related to “group II” patterns known from refractory inclusions in carbonaceous chondrites. The latter formed from a depleted gas reservoir after condensation of an Al- and Ca-bearing ultrarefractory component. Most likely, both chondrule populations condensed from very localized gas compartments. Silicon isotope compositions of CC chondrules are heavier than the chondritic average and in parts also than BSE. This indicates loss of light Si isotopes prior to formation of those chondrules, which may be caused due to early condensation of BO chondrules and/or CAIs. All examined CC chondrules show an enrichment in Cr composition relative to CI. Such high Cr concentrations hint towards oxygen fugacities that were higher than in the solar nebula and are characteristic for an impact-induced vapor plume. This observation, in combination with the occurrence of CC chondrules within zoned metal, that was proposed to have formed from an impact plume, indicates that CC chondrules have formed from the same vapor plume as metal, and that CC chondrules condensed prior to the rims of zoned metal. Moreover, Mo and W abundances are in good agreement with the formation scenario discussed (part II of this study) for metal of CH and CB_b chondrites. Thus, metal and chondrules from CH and CB_b chondrites likely formed in a closed system.

2 INTRODUCTION

Chondrules are a major constituent in primitive chondritic meteorites that are least altered by either thermal or aqueous alteration. Therefore, chondrules are important objects to be studied to unravel processes in the early solar system. Though it is consensus that chondrules formed by fast-cooling from siliceous melt droplets, the heating process and the precursor material are still being controversially discussed. Some research groups suggest that precursor material were dust grains from the solar nebula and that they were heated by shock waves or solar winds (e.g., Shu, 2001). Other groups propose that chondrules formed in the event of colliding planetesimals which caused splashing of melt droplets that subsequently crystallized at fast cooling rates (e.g., Sanders and Scott, 2012).

CH and CB chondrites are special among the chondrites due to their high metal content (~30 vol% and 70 vol%, respectively). In those meteorite groups, chondrules are not the main constituent. Moreover, the most abundant chondrule type is of cryptocrystalline (CC) texture (60%, Krot et al., 2001). These are thought to have formed by condensation due to the depletion in moderately volatile elements (Wasson and Kallemeyn, 1990; Russell et al., 2000; Krot et al., 2001; Jacquet et al., 2012). Chondrules from CB_b chondrites do not show evidence for remelting, as they lack metal particles and relics of early chondrule generations inside, and also lack of porphyritic textures (Krot et al., 2001). All these observations support a condensation origin (Krot et al., 2001). Furthermore, Krot et al. (2001) suggest that the dominance of CC

Part IV: Formation conditions of CC chondrules

chondrules and the lack of porphyritic textures, are caused by formation of CH and CB_b chondrules from a reservoir that was free of particles that would function as crystallization nuclei. Such a reservoir is likely consistent with a giant vapor cloud that formed by complete evaporation of solid constituents of the impact plume. This is also supported by the FeO contents of CC and barred olivine (BO) chondrules within CH and CB_b chondrites, which indicate more oxidizing conditions than was inferred for the solar nebula (Krot et al., 2001). Additionally, Cr contents of chondrules and metal grains also indicate oxidizing conditions and are related with each other. This suggests that both constituents formed in the same closed system (Krot et al., 2001). Thus, it was proposed that CC chondrules condensed from an impact-induced gas (Krot et al., 2001). The inferred elevated dust/gas ratios are in favor of gas-liquid condensation rather than heating of gas-solid precursors above their liquidus (Krot et al., 2001).

Evidence for a condensation origin of silicates from an impact plume is also given for CB_a silicates. Oulton et al. (2016) report Ce anomalies that indicate complete evaporation and subsequent re-condensation. Moreover, Pb-Pb dating of chondrules from Gujba (CB_a) (Bollard et al., 2015) revealed that chondrules are ~2 Ma younger than chondrules from other chondrite groups. Such young ages are consistent with the existence and collision of planetesimals and thus support an origin of chondrules from CH and CB carbonaceous chondrites from an impact plume.

In the previous chapters, we have shown that both zoned and unzoned metals from CH and CB_b chondrites most likely formed during condensation from an impact induced vapor plume. Here we perform *in situ* trace element and Si isotope analyses on CC chondrules from the same chondrites to draw conclusions on their formation conditions. These data allow to test whether CC chondrules formed by condensation from an impact induced vapor plume and allow to set results into context with the formation models proposed for associated metal (parts II and III).

3 SAMPLES AND METHODS

We investigated CC chondrules from several CH chondrites (Sayh al Uhaymir 290, PAT 91546), CB_b chondrites (Hammadah al Hamra 237, MAC 02657, QUE 94411), and the CH/CB_b breccia Isheyevo.

Major and minor element composition of 50 chondrules (10 in each sample) were analyzed with a Cameca SX 100 electron microprobe. Measurements were performed at 15 nA and 15 kV with a focused beam. Table S1 lists the examined elements, their detection limits, analytical errors, and standards used for calibration. Matrix corrections were carried out using the PAP procedure (Pouchon and Pichoir, 1984).

Part IV: Formation conditions of CC chondrules

Trace element analyses of 26 CC chondrules in total from MAC 02675 (5), QUE 94411 (4), SaU 290 (10), and Isheyevo (7) were executed via fs-LA-SF-ICP-MS. Number in parenthesis denotes the number of examined chondrules in the sample. A Spectraphysics Laser system was connected to a Thermo Scientific Element XR. Measurements of chondrules were performed with spiral laser patterns. Those were measured using a fast moving sample stage connected to a self-built XYZ-controller unit, which is operated by the open-source programme *Linux CNC*. Spot size of the laser was 30 μm . The basaltic glass BCR-2G was used as external standard, Mg values from electron microprobe analyses were used as internal standard. In each analysis, background was measured for 40 s, before signal was measured for ~2 minutes. Table S1 lists the measured elements with their detection limits and analytical uncertainties.

We also analyzed Si isotope compositions of CC chondrules from HaH 237 (4) and Isheyevo (4). However, those chondrules are not the same that were analyzed for trace element composition as grain sizes are too small to perform both measurements on a single chondrule. Isotope measurements were performed *in situ*, connecting the Spectraphysics Laser system with a Thermo Scientific Neptune Plus (MC-ICP-MS). A cone combination of a Ni X-Skimmer cone and a Ni sample cone were used. A 0.5 mm spacer was added to this setup. Measurements were performed with dry plasma and a reduced laser output energy (9 mV vs. 13 mV prior to reduction). Chondrules were analyzed in sample-standard bracketing for mass-bias correction, using the JER-Diopside Glass as standard. The background signal for Si isotope measurements was initially 45 mV on ^{28}Si and slightly increasing during the measurement day. No measurements were performed with a background signal higher than 70 mV, the signal on ^{28}Si was ~9V during measurements. The relatively high background values are probably due to the usage of a glass torch. Analytical uncertainties for $\delta^{30}\text{Si}$ values are 0.3‰ (mean deviation from the reported standard value) calculated by repeated measurements (n=6) of the standard IRMM-017. The analytical uncertainty is consistent with values given for *in situ* measurements in the literature (0.24‰ in Chmeleff et al., 2008). The laser spot was 30 μm in diameter and chondrules were analyzed in spiral patterns with a *Linux CNC* controlled sample stage. The integration time between two cycles was ~1 s. At the beginning of each analysis 30 s background were measured before starting the laser. One analysis consisted of 180 cycles, thus signal was measured for about 2 minutes.

Part IV: Formation conditions of CC chondrules

4 RESULTS

4.1 Chemical composition of CC chondrules

All CC chondrules from CH and CB_b chondrites, that were analyzed in the case of this study, have low FeO contents with a maximum of ~3.5 wt%. Thus, they are all type I chondrules. Moreover, they are all enstatite normative in composition with low chemical variation. Chromium contents vary between 0.2 up to 0.77 wt% within most chondrules, on average 0.4 ± 0.06 wt% (SD). Only two chondrules, one in PAT 91546 and one in HaH 237, have significantly higher Cr concentrations with ~1.1 wt%. These values lie at the upper end of the Cr contents that are usually found in enstatite from primitive meteorites (0.3-0.5 wt%, see Brearley and Jones (1998) and references therein). Element ratios show that some elements are strongly differing from solar abundances: Cr/Mn ratios vary between 1.38 and 7.97 (on average ~5, see Fig. 1) and are significantly higher than the solar ratio (1.37 (Lodders et al., 2009)). Moreover, Mg/Cr ratios are much higher than the solar ratio (~50 vs 36 (Lodders et al., 2009), respectively).

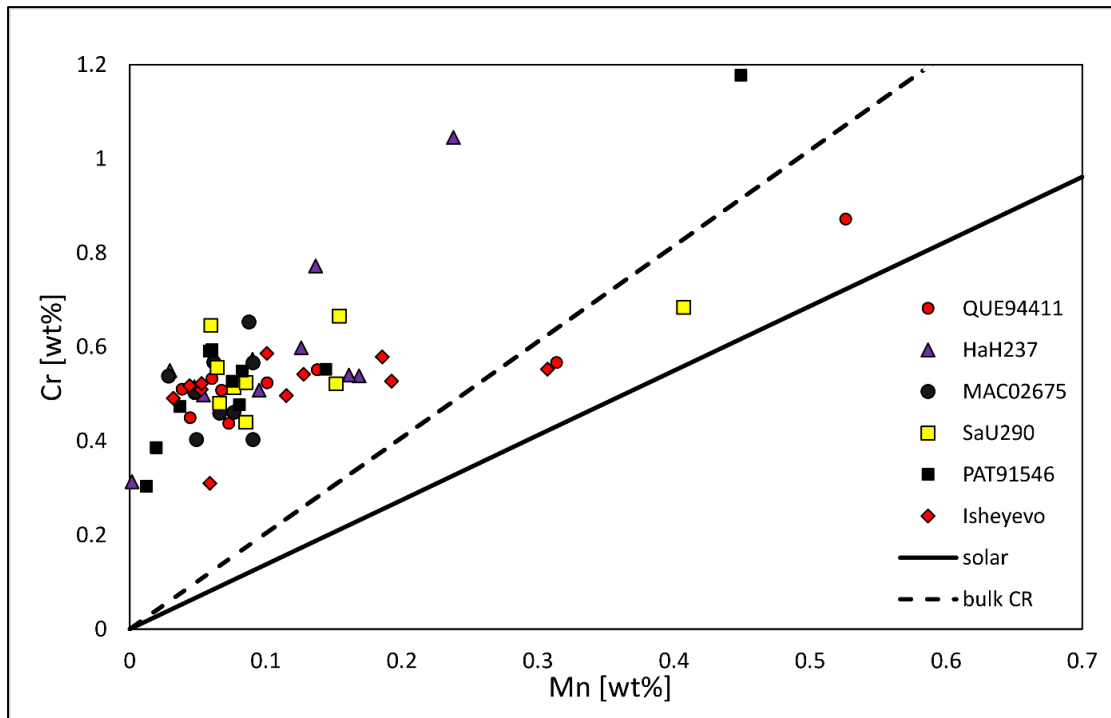


Figure 1: Cr concentrations of examined chondrules plotted against respective Mn contents. It becomes obvious that Cr/Mn ratios are higher than solar proportions (black solid line) of these elements. The dashed line represents the bulk Cr/Mn ratio of CR chondrites, and is the mean value of the three samples analyzed in (Weisberg et al., 1993). Chondrule compositions are mainly quite uniform and compositional differences are not correlated with the meteorite type.

Part IV: Formation conditions of CC chondrules

Major and trace element analyses reveal that the chondrules have quite variable abundances of trace elements. However, CI normalized patterns show that they all have some features in common (Figs 2 and 3). Those are, that Cr and V are enriched in all chondrules relative to CI (1.3-1.7xCI and 1.7-2.1xCI, respectively), a general enrichment of Mg (2.1-2.7xCI), and a depletion in Fe relative to CI (0.02-0.15xCI).

It appears that most of the analyzed chondrules show a small deviation in Ce abundance compared to neighboring elements of similar 50 % condensation temperature. Cerium anomalies were examined as described in Oulton et al. (2016). Both, positive and negative anomalies were found. The highest positive anomaly is +127 % and the strongest negative anomaly -55 %. Both values exceed the anomalies described in the literature (+22 % and -25 % (Oulton et al., 2016)).

Generally, two groups of chondrules can be distinguished: one group has superchondritic (Fig. 2) abundances of refractory elements and the other one has subchondritic to chondritic (Fig. 3) concentrations of those elements.

4.1.1 Superchondritic chondrules

Seven of the analyzed chondrules have superchondritic abundances of refractory elements, and they can be found in all meteorite types examined in this study (Fig. 2). Three are found in MAC 02675, two in SaU 290 and one is found in QUE 94411 as well as in Isheyevo. They all have in common that they are enriched in elements more refractory than Fe. Patterns of refractory elements are rather flat with some smaller peaks or dips. Exceptions to that are Mo concentrations, which show a large depletion relative to other refractory elements in five of the discussed chondrules. Additionally, there seems to be a difference in the W abundance of the superchondritic chondrules in CB_b in comparison with those in SaU 290 and Isheyevo. Tungsten seems to be generally enriched relative to CI within CB_b chondrules, while W concentrations are depleted in chondrules from CH sample SaU 290 and the CH/CB_b breccia Isheyevo. Apart from that, no correlation between chemical anomalies and the meteorite type can be observed. Chondrules from MAC 02675 show constant W abundances, while this element is more strongly enriched within the superchondritic CC chondrule from QUE 94411.

Part IV: Formation conditions of CC chondrules

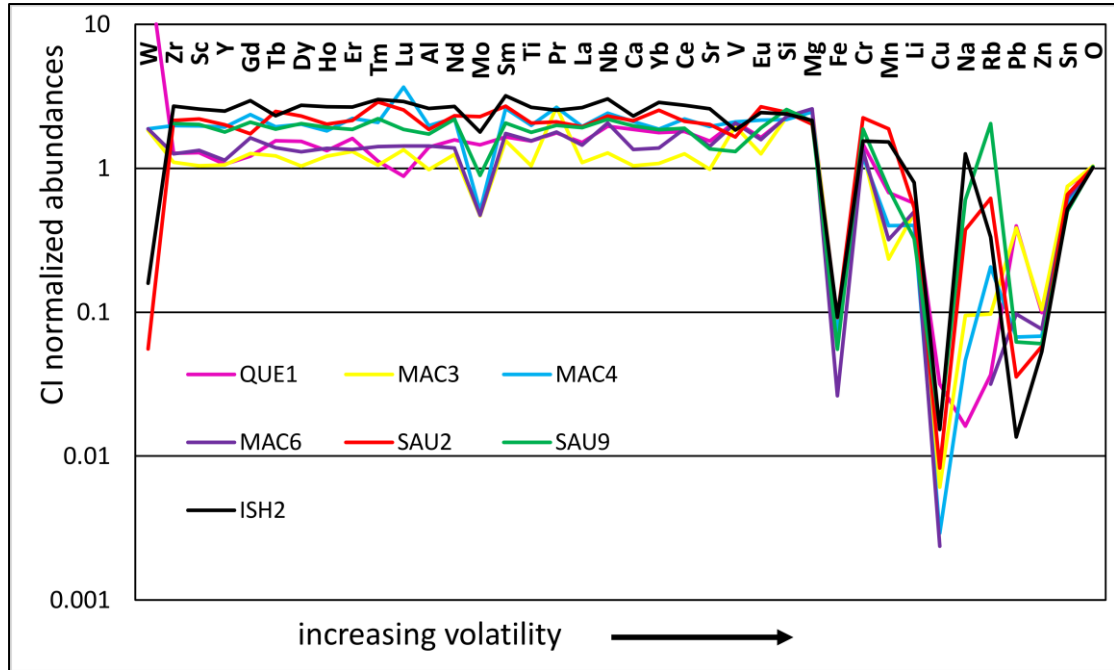


Figure 2: CI normalized element abundances of CC chondrules with superchondritic refractory element compositions.

4.1.2 Subchondritic chondrules

The majority of the here examined chondrules have subchondritic to chondritic refractory element concentrations. Though abundances of refractory elements are highly variable, W concentrations in subchondritic chondrules are quite constant in the majority and reach superchondritic values (1.2-1.8xCI, Fig. 3). The Mg/Si ratios in subchondritic chondrules are unfractionated from the solar one.

Part IV: Formation conditions of CC chondrules

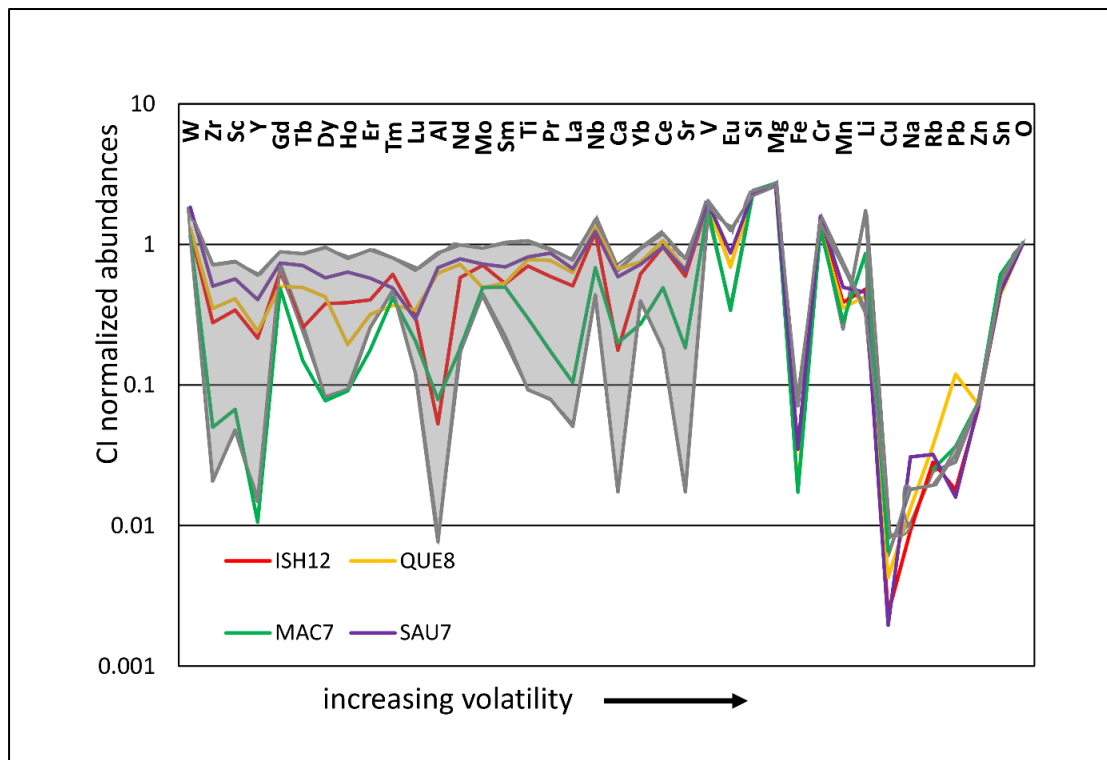


Figure 3: Cl normalized abundances of chondrules with overall subchondritic to chondritic element abundances. Grey area represents the range of element abundances. It becomes obvious that volatile element abundances are much more uniform than refractory elements. An abundance pattern of a chondrule from each examined sample is also represented. The W abundances are quite constant despite the variable concentrations of other elements.

Rare earth elements in the subchondritic CC chondrules reveal two different kinds of patterns (Fig. 4). One group of subchondritic chondrules show flat REE patterns, without systematic fractionation between LREE and HREE (e.g., .SaU7 and Ish6).

However, the REE abundance patterns of some chondrules (e.g., MAC2 and MAC7) exhibit features related to group II patterns in CAIs found in CH chondrites (Kimura et al., 1993). Gadolinium in CC chondrules is the only element not following the pattern of the described group II pattern, as it is more enriched than in the samples from Kimura et al. (1993). Those patterns are associated with depletion in the refractory major and minor elements Al, Ca, and Ti.

Part IV: Formation conditions of CC chondrules

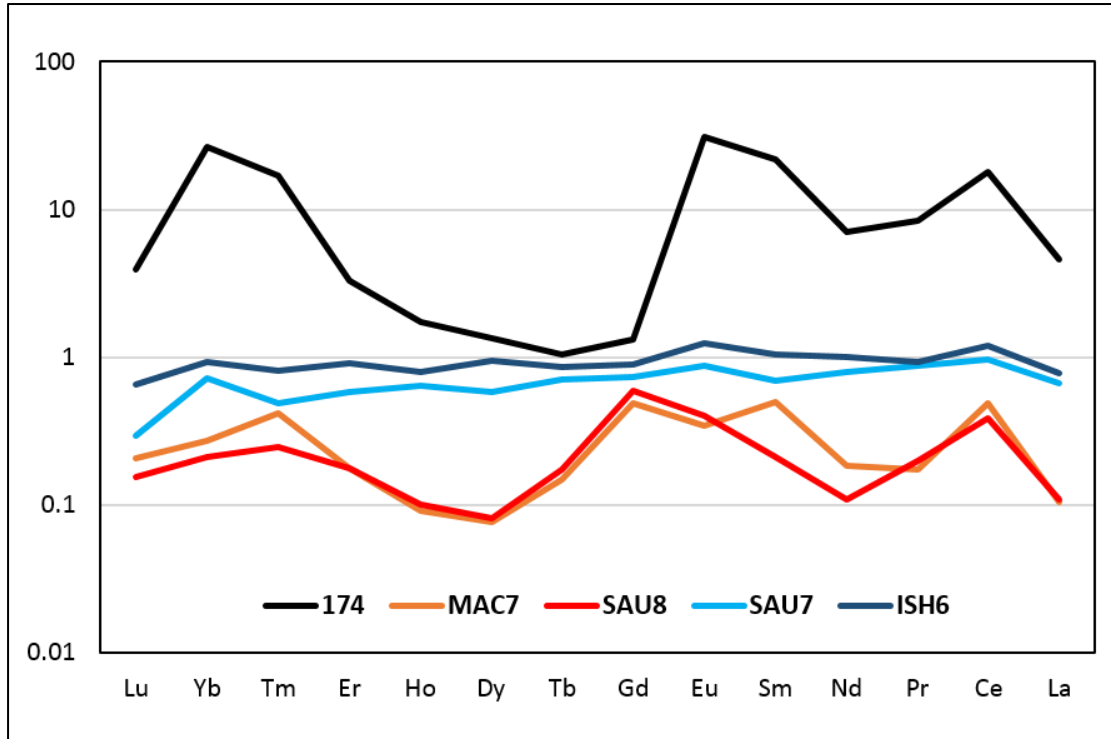


Figure 4: REE patterns of subchondritic CC chondrules. Representative flat REE patterns in blue (SaU7 and Ish6), and group II-like patterns in red/orange (MAC7, SaU8). The black line (174) represents the group II like pattern found in a CAI in ALHA85085 by Kimura et al. (1993).

4.2 Si isotope composition

Silicon isotope compositions were analyzed for 8 CC chondrules, 4 in Isheyev and 4 in HaH 237. Unfortunately, no trace element data are available for those chondrules, as grain sizes are too small to measure both Si isotope and trace element compositions of the same chondrule. Though some individual chondrules of the two samples overlap within analytical uncertainties (0.3‰ on $\delta^{30}\text{Si}$), average $\delta^{30}\text{Si}$ values for both are isotopically slightly different. Isheyev chondrules tend to have somewhat heavier Si isotope composition than chondrules from HaH237 ($0.14 \pm 0.16\%$ vs $-0.23 \pm 0.1\%$, respectively; errors are 2SD). However, this difference does not seem to be related to the meteorite type. Isheyev contains CB_b and CH lithologies, two chondrules were examined in each lithology. Both CB_b chondrules overlap in their Si isotope composition within uncertainties with the two chondrules from the CH lithology. The latter, however, tend to plot towards heavier isotope composition. Figure 5 shows that CC chondrules from Isheyev are isotopically heavier than the bulk composition of carbonaceous chondrites and the BSE (Pringle et al., 2013). Chondrules from HaH 237 plot together with the heavy end of the BSE, and are somewhat heavier than literature values for carbonaceous chondrites. However, they overlap within the analytical uncertainty.

Part IV: Formation conditions of CC chondrules

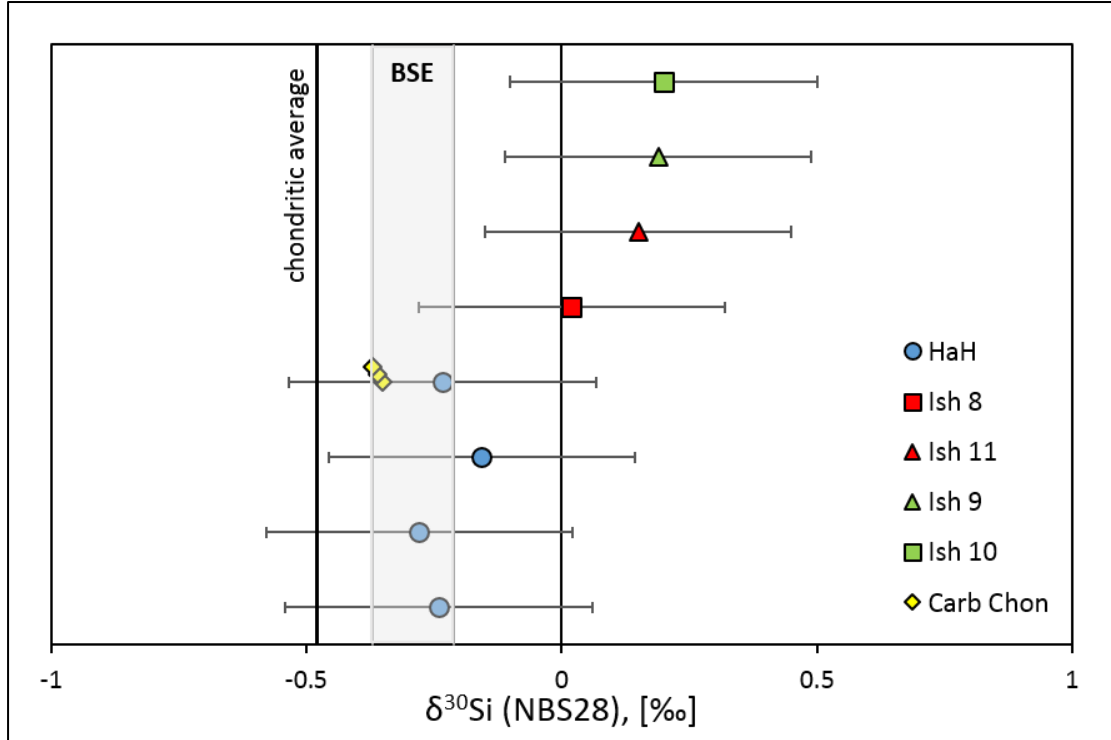


Figure 5: Silicon isotope data of chondrules from Isheyevo and HaH237 plotted with the chondritic average value (solid line), the BSE (grey field), and Si isotope composition of carbonaceous chondrites (yellow diamonds). Values of the chondritic average, carbonaceous chondrites and the BSE are taken from Pringle et al. (2013). Green chondrules from Isheyevo are located in the CH lithology, red chondrules in the CB_b lithology. Isheyevo chondrules seem to be somewhat heavier than BSE and chondrules from HaH237. However, values overlap within the error ($\sigma=0.3\text{‰}$).

5 DISCUSSION

5.1 Formation conditions of CC chondrules in CH and CB_b chondrites

Two CC chondrule populations were found among our samples, one with superchondritic and one with subchondritic refractory element abundances. Both groups are very similar in the relative abundances of volatile elements which are strongly depleted.

Trace element abundances of the superchondritic CC chondrules indicate a condensation origin for those chondrules, since abundance patterns follow the cosmochemical behavior of the elements (Fig. 2). Elements more refractory than Fe are enriched over CI with flat and unfractionated patterns (except for depletion in Mo), this indicates that formation of those chondrules was finished before the gas reservoir cooled down to the condensation temperature of elements more volatile than Fe and that metal had already started to condense. Similar abundance patterns were also reported for barred olivine (BO) chondrules from CB_b chondrites (Krot et al., 2001). Therefore, a common formation process can be assumed for these chondrule populations. Compositional similarities of BO and superchondritic CC chondrules also indicate

Part IV: Formation conditions of CC chondrules

that both formed simultaneously from the same unfractionated reservoir. Chromium contents in the chondrules are higher than usually reported for enstatite-normative compositions (Brearley and Jones, 1998). Krot et al. (2001) also report FeO contents (Fa_{2-4}) in BO chondrules, from CB_b chondrites, that are higher than expected for condensates from the solar nebula, which would be pure forsteritic olivines (Lodders et al., 2009). These element enrichments indicate elevated oxygen fugacities relative to the solar nebula. Elevated oxygen fugacities are a characteristic of an impact vapor plume (Fedkin and Grossman, 2016). Another feature that supports the assumption that those chondrules have formed in an impact plume, are the unusually young ages that were reported for chondrules from CH and CB meteorites in the literature (Krot et al., 2001; Bollard et al., 2015). Elevated dust/gas ratios are related with an impact setting (Meibom et al., 2001; Fedkin and Grossman, 2016), and favor gas-liquid condensation (Krot et al., 2001). Since high pressures are needed for gas-liquid condensation, it is likely that chondrules formed in the inner regions of the impact plume as it was also suggested for unzoned metal from CH and CB chondrites (see parts II and III).

Subchondritic CC chondrules, both with flat REE patterns and group II-like patterns, also show enrichments in Cr and V relative to solar values, and also display Ce anomalies (both positive and negative) as described for the superchondritic chondrules. Due to these similarities, a common formation process can be suggested for superchondritic and subchondritic chondrules. Subchondritic CC chondrules were also described in the literature (Krot et al., 2001) and were proposed to have formed a condensation sequence with BO chondrules, which resemble the superchondritic CC chondrules. However, the highly fractionated refractory element patterns cannot be explained by simple depletion of a gas reservoir by formation of unfractionated superchondritic CC and BO chondrules. Instead, the REE patterns, especially of MAC7 and MAC2, are rather similar to the group II pattern previously described from CAIs in CH chondrite ALH 85085 (Kimura et al. 1993). This pattern is characterized by depletion of ultrarefractory elements Gd to Er, and Lu compared to more volatile REE, such as La, Sm, and Tm. Other indicators for group II pattern are depletions in Zr, Y, Sc relative to less refractory Nb. Group-II patterns are generally thought to reflect condensates from a gas reservoir that was previously depleted by loss of an ultrarefractory component (Boynton, 1975). This component was likely Ca, Al, and Ti-rich. Such an ultrarefractory component, not yet identified in our samples, must have fractionated the gas reservoir prior to formation of subchondritic CC chondrules.

Subchondritic chondrules with flat REE patterns are also unlikely to have formed within a condensation sequence together with superchondritic CC and BO chondrules, as the subchondritic chondrules are also depleted in Al, Ti, and Ca. However, these elements are not enriched relative to other refractory elements in superchondritic chondrules. Thus, formation

Part IV: Formation conditions of CC chondrules

of superchondritic chondrules cannot have fractionated the reservoir in those elements, and cause the observed depletions in the subchondritic chondrules with flat REE patterns. Thus, the latter must have condensed from a reservoir that was fractionated in refractory elements by early condensation of a refractory phase that is rich in Al, Ti, and Ca.

Regarding the Ce anomalies in the examined CC chondrules, it can be noted that subchondritic chondrules with group II like patterns, show high positive anomalies, while superchondritic chondrules all show negative anomalies and subchondritic chondrules with flat patterns show negative to weakly positive anomalies. Thus, Ce anomalies may not indicate evaporation (negative) and re-condensation (positive) as suggested by Oulton et al. (2016), but simply reflect different degrees of fractionation of gas volumes.

In summary, these observations described above suggest that CC chondrules likely condensed in highly localized compartments of gas volumes, which remained either unfractionated or fractionated. In this case, only the fractionated gas regions were depleted to variable degrees by early condensation of ultrarefractory element enriched inclusions containing e.g., Ca-dialuminate, hibonite, and perovskite (e.g., Bischoff et al., 1992).

5.2 Constraints on the formation of CC chondrules from their Si isotope compositions

Silicon isotope composition was shown to be quite homogeneous among meteorites. Chondrite groups such as carbonaceous chondrites and ordinary chondrites are indistinguishable from each other and also from the achondrite groups of ureilites and HED meteorites (Pringle et al., 2013). Thus, it was proposed that the protoplanetary accretion disk was homogeneous at the time of planet formation (Pringle et al., 2013). However, the Si isotope composition of the bulk silicate Earth (BSE) is somewhat heavier than the chondritic average. Moreover, Angrites are the only meteorites that plot with BSE (Pringle et al., 2014) and thus, are heavier than other meteorite groups. The CC chondrules analyzed in this study also show rather heavy isotope composition, which overlap with, or are even heavier than, BSE and Angrite values. Since a homogeneous composition of the solar nebular is proposed (Pringle et al. 2013), heavier isotope compositions were likely produced by processes, such as evaporation, condensation or planetary differentiation, that resulted in fractionation relative to the primordial composition of the protoplanetary disk. For the heavy Si isotope composition of the BSE Fitoussi and Bourdon (2012) proposed core formation as a possible cause. In this scenario Si migrated from the silicates into the metal core. This would generate a core with a light Si isotope composition and leave a BSE with a heavy Si isotope composition behind. To reach Si isotope values reported for BSE, it was calculated that ~7 wt% of Si must be present in Earth's core

Part IV: Formation conditions of CC chondrules

(Javoy et al., 2010). Since our samples are chondritic, core formation can be excluded as explanation for heavy Si isotope composition. Considering heavy Si isotope compositions of Angrites, Pringle et al. (2014) proposed loss of light isotopes due to an impact event during accretion. To verify such a process for our samples, it is necessary to measure bulk Si isotope compositions. This would reveal if heavy Si isotope composition is only typical for CC chondrules or if the depletion in light Si isotopes is a general characteristic of CH and CB_b chondrites. Alternatively, the slightly heavier Si isotope composition of the CC chondrules may be a result of sequential (and localized) condensation of the silicates. Examined CC chondrules are enstatite normative in composition, forsterite and melilite both condense prior to enstatite (see Fig.4b in Dauphas et al., 2015). Thus, condensation of BO chondrules or CAIs prior to condensation of CC chondrules, from the same reservoir, would lead to Si isotope fractionation. Likely, light isotopes would go into the early condensates (BO or CAI, assuming kinetic isotope fractionation during condensation, as observed for the metal) and CC chondrules would condense from a gas that is enriched in heavy Si isotopes. In this scenario, the superchondritic (as well as BO) chondrules should display lighter Si isotope compositions than the subchondritic chondrules. In order to test this hypothesis, it would be necessary to have combined trace element and Si isotope data of individual chondrules, which was not possible within the term of this study. Combined trace element and Si isotope data of CC chondrules may thus further help unraveling their formation in highly localized compartments of the gas reservoir.

5.3 Relation of chondrules and metal in CH and CB chondrites

The Cr contents of CC chondrules and zoned metal from CH and CB_b chondrites indicate a connection of those constituents, as both formed at elevated oxygen fugacities. Concentrations of Cr in chondrules is higher than expected at solar oxygen fugacity, and lower in coexisting metal than expected at solar oxygen fugacity (Krot et al., 2001; Petaev et al., 2003). The accordance of this fO_2 indicator within chondrules and metals, demonstrate that metal and chondrules of CH and CB_b chondrites have formed in the same reservoir. The majority of the examined chondrules (16), both superchondritic and subchondritic, have quite constant W abundances with ~1.2-1.8xCI. Molybdenum concentrations in those chondrules are also quite constant with 0.4-0.9xCI (only exception: SaU8). Such superchondritic W abundances and subchondritic Mo contents, are in good agreement with the formation scenario discussed for metal from CH and CB_b chondrites. In part II we discuss, that W is depleted relative to other refractory elements in zoned metal, but also in some unzoned metal grains. Molybdenum on the other hand does not show any depletion or a less-pronounced depletion

Part IV: Formation conditions of CC chondrules

than W. This is explained by fast disequilibrium condensation of the metal under oxidizing conditions (relative to solar nebula). In this scenario W occurs in the gas as W-oxides and is thus less abundant in metal. The enrichment of W in chondrules is in accordance with this scenario. This is also the case for Mo abundances, which is incorporated as alloys into metal, and thus should be less abundant in the silicates, which was observed for our chondrules. These observations support the conclusion that metal and chondrules formed during the same event in a closed system. However, not all of the chondrules show the same Mo and W abundance patterns. If real, such variable Mo and W contents may reflect local differences in the gas due to variably strong non-equilibrium conditions, or are an indicator for an imperfectly closed system. Alternatively, they may be artificially produced by contamination of the chondrules during their analyses by simultaneous ablation of small amount of adjacent or subjacent metal. Various analyses showed wavy signals for Ni and Co. However, no strong correlation between high Ni and Co values and the Mo and W concentrations was observed.

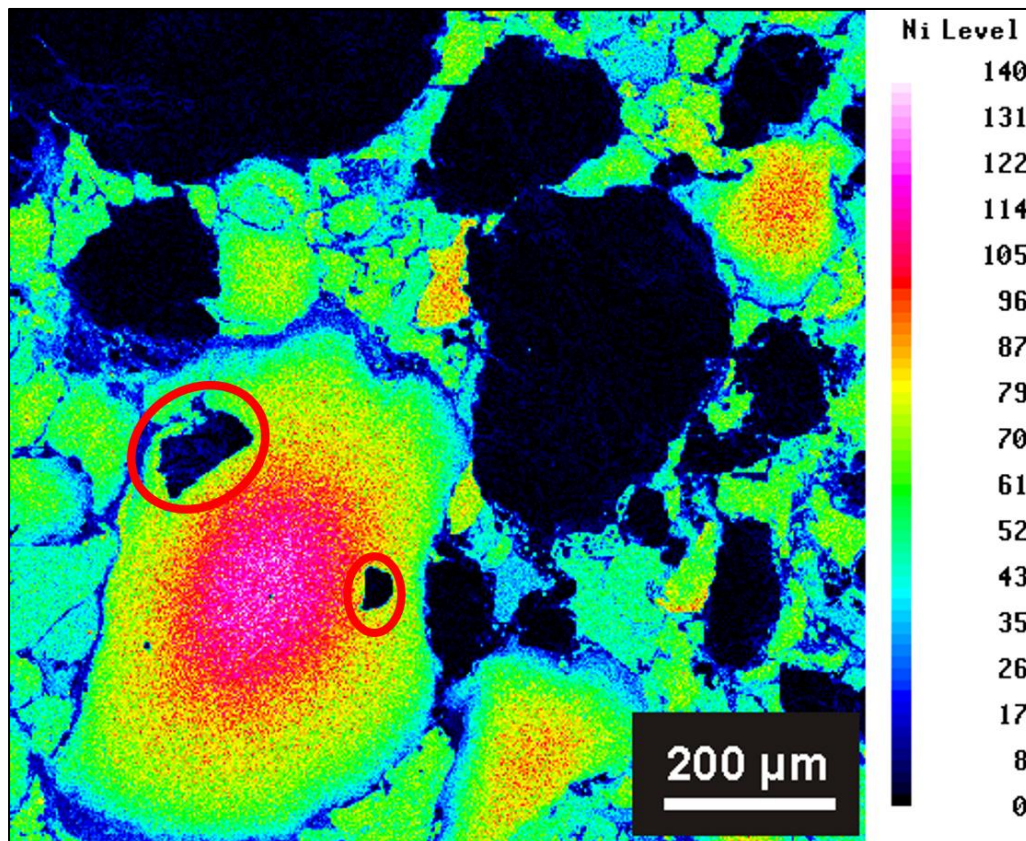


Figure 6: Ni element distribution map of metal in HaH237 (pink/white = high contents, blue/green = low contents). A large zoned metal grain is apparent that incorporates fragments of CC chondrules (circled in red) within its rim region.

An additional important observation, regarding the order of chondrule and metal condensation, is that CC chondrules can be found within zoned metal grains (Fig. 6), while no metal is found within CC chondrules. This suggests that CC chondrules have formed prior to

Part IV: Formation conditions of CC chondrules

zoned metal. As discussed in parts II&III of this thesis, zoned metal most likely formed in the fast-cooling shell region of the impact plume. Thus, it is likely that CC chondrules were incorporated into zoned metal during its formation, when chondrules were migrating out of their formation region, which was probably in the inner region of the plume. As CC chondrules are found in the rim regions of zoned grains, it is possible that metal formation already started during chondrule condensation, and that metal and chondrules were formed simultaneously over a short period of time. This can also explain the depletion of Fe in CC chondrules. Unfortunately, no data is available for such incorporated chondrules, to further support the described relationship.

6 CONCLUSION

Chemical and isotopic investigation of cryptocrystalline chondrules revealed two chemically distinct populations of CC chondrules, one population being enriched and the other one being depleted in refractory elements relative to CI abundances. Enrichment in refractory and depletion of moderately volatile elements indicates a condensation origin. This is supported by the lack of evidence for reheating of chondrules (Krot et al., 2001). Relatively high Cr contents in CC chondrules indicate oxygen fugacities that were higher than in the solar nebula, and are in favor of formation of chondrules from an impact-induced vapor plume. The chondrule population with superchondritic refractory element abundances is compositionally similar to BO chondrules examined in the literature (Krot et al., 2001), which are proposed to be the first chondrules to condense. Cryptocrystalline chondrules with subchondritic composition are consistent with findings in the literature that proposed them to have formed subsequently to BO chondrules (Krot et al., 2001). These findings indicate that superchondritic CC chondrules have formed simultaneously with BO chondrules. In contrast, since some of the subchondritic CC chondrules have fractionated refractory trace elements, not reflected in the unfractionated patterns of the superchondritic chondrules, these chondrules cannot have condensed from the same gas reservoir. Rather, condensation from confined gas compartments can be suggested for the different chondrule populations. In this scenario, subchondritic CC chondrules with group-II related patterns of refractory trace elements must have formed after condensation of an ultrarefractory-rich component that resulted in depletion and fractionation of refractory elements. Chromium, W, and Mo abundances of chondrules and metal are in accordance with each other and thus indicate formation of both phases within a closed system. Therein, elevated oxygen fugacities and fast disequilibrium condensation of metal leads to favored incorporation of W and Cr into chondrules rather than into metal, and favored incorporation of Mo into metal rather than into chondrules.

Part IV: Formation conditions of CC chondrules

The Si isotope compositions of CC chondrules from HaH 237 and Isheyevo did not correlate with the meteorite type. However, both samples show rather heavy Si isotope compositions that only overlap slightly or do not overlap with the chondritic value. Since a homogeneous composition of Si isotopes was suggested for the solar nebula (Pringle et al., 2013), the gas reservoir from which CC chondrules formed must have been depleted in light Si isotopes. This can be achieved by condensation of forsterite or melilite prior to condensation of the enstatite-normative CC chondrules. Thus, we suggest that BO chondrules or CAIs formed prior to the CC chondrules we analyzed for Si isotope composition. To further support this proposal, it is necessary to perform trace element analyses and isotope measurements on the same chondrules. The occurrence of CC chondrules within zoned metal grains, which is supposed to have formed in the shell region of an impact plume (Part II&III), suggests that CC chondrules have formed prior to metal, probably in the inner regions of the plume, and were incorporated into the metal on their way out. Since CC chondrules are located in the rim regions of the zoned grains it is possible that chondrules and metal rims formed simultaneously.

Conclusion and Outlook

Results of this study confirm a condensation origin for metal and chondrules from CH and CB chondrites. Linked Mo, W, and Cr compositions of metal and chondrules suggest that those constituents formed in a closed system. Since those element abundances are indicative for oxygen fugacities higher than those in the solar nebula, a formation origin in an impact-induced vapor plume is in favor rather than a nebular origin. Such a formation scenario is also supported by the remarkably young chondrule ages of CB chondrites (Kleine et al., 2005; Krot et al., 2005; Bollard et al., 2015). Data of this study also suggest that zoned metal has been formed with high cooling rates, which favor kinetic fractionation. First modeling was performed. However, obtained cooling rates contain errors, as it was not possible to fit the model well enough to measured values due to the lack of diffusion processes in the MATLAB code. Thus, it is necessary to include diffusion parameters to gain a better fit and thereby get more reliable information on cooling rates.

Based on combined data from Ni isotopes and Ir contents, two groups of zoned metal were identified, which may have formed under the influence of different cooling-rates. To support this observation it would be necessary to also include Ir concentration into the model. By that, it would become obvious if deviating Ir patterns are correlated with different cooling rates. Moreover, different formation conditions were suggested for unzoned and zoned metal grains. Thus, modeling of both metal types would provide further information on the formation processes.

Cryptocrystalline chondrules from CH and CB_b chondrules were found to be chemically divided into two groups. One with superchondritic refractory element abundances and depletion in volatile elements, and one with generally subchondritic element abundances. The superchondritic ones are thought to condense simultaneously with BO chondrules. Subchondritic CC chondrules are unlikely to have formed in a condensation sequence with the before mentioned chondrules, as subchondritic refractory element patterns are fractionated in a way that cannot be caused by preceding formation of BO and superchondritic CC chondrules. To be able to draw further constraints on chondrule formation histories, it is necessary to perform Si isotope and trace element analyses on the same chondrule to gain further information on possible condensation sequences. Moreover, such measurements should also be done on BO chondrules. Due to the heavy Si isotope compositions of CC chondrules it was suggested that light Si isotopes were extracted from the gas by condensation of forsterite or melilite, which are abundant in BO chondrules or CAIs, respectively. Thus, Si isotope analyses of those phases

Conclusion and Outlook

may support or refute the proposed formation process. As evaporative loss of light Si isotopes due to the impact event is also a possible explanation for heavy Si isotope contents of CC chondrules, bulk Si isotope data for the samples would reveal if heavy Si isotope compositions are a general characteristic of CH and CB chondrites, or if this feature is typical for CC chondrules.

Concerning the relationship of the different metal-rich carbonaceous chondrite groups, this study showed that CH and CB chondrite metal and chondrules most likely formed in the same event, due to the many chemical and isotopic similarities. However, there are some features that set CH chondrites apart from CB chondrites. In CH chondrites metal with high Si contents (11 wt% (Weisberg et al., 1988; Goldstein et al., 2007)) and also with high Ni contents (>20 wt% (Goldstein et al., 2007; Ivanova et al., 2008)) were found. Akin grains were not described for CB_a or CB_b chondrites. As those metal grains are only about 20 µm in diameter, it was not possible to perform laser ablation analyses on them. Investigation of those metals may deliver information about their formation and reveal if their origin is related to other metal grains found in CH chondrites, or if they were somehow collected in the accretion process.

Another open question is the fractured characteristic of constituents in CH and CB chondrites. Metals and larger chondrules show frayed rims and thus need to have been degenerated by some process. This process must have taken place when metal and chondrules were already in a solid state. However, it is unclear which process led to this. Accretion may not have been energetic enough to cause such heavy fracturing of metals and chondrules. Multiple collision events may be an explanation for those features and may also be able to explain the different meteorite lithologies in some of the CB_a chondrites.

Regarding the relationship of CH and CB chondrites with CR chondrites, there is evidence that CR chondrites did not form in the same event as CH and CB chondrites. Chondrule ages are older than those of CH and CB chondrites (Budde et al., 2018) and metal is closely associated with those chondrules, and as old or even older than those chondrules. However, features like bulk isotope similarities in N, O, Cr, and Ti (Krot et al., 2002; Trinquier et al., 2009; Van Kooten et al., 2016) are in favor of a relationship of the different meteorite groups. Beside those isotopic similarities hydrated clasts can be found in CH and CB_b chondrites, which are compositionally akin to matrix material from CR chondrites (Greshake et al., 2002; Leitner et al., 2018). Nonetheless, those clasts were also described to be similar to CM chondrite material (Greshake et al., 2002; Leitner et al., 2018). Thus, the origin of hydrated clasts is still unclear and may not directly be linked to a relationship between CH, CB_b and CR chondrites. However, those clasts cannot have formed together with the high-temperature phases (metal and chondrules) from CH and CB_b chondrites, and thus are unlikely to have formed within an impact plume. A possible scenario would be that CH and CB_b chondrites

Conclusion and Outlook

collected hydrated clasts during accretion. To unravel the origin of the hydrated clasts, it may be necessary to also investigate similarities between CH, CB, and CM chondrites, and CR and CM chondrites.

Data of this study allow drawing constraints on the formation of the constituents of CH, CB and CR chondrites, and on the relationship of those metal-rich carbonaceous chondrites. However, there are still many details that need to be looked into, which may support the here drawn conclusions.

References

References

- Alexander C. M. O. and Wang J. (2001) Iron isotopes in chondrules: Implications for the role of evaporation during chondrule formation. *Meteorit. Planet. Sci.* **36**, 419–428.
- Alexander C. M. O. and Hewins R. H. (2004) Mass fractionation of Fe and Ni isotopes in metal in Hammadah al Hamra 237. *Meteorit. Planet. Sci.* **39** #5080.
- Armstrong J. T. (1995) CITZAF: A package of correction programs for the quantitative electron microbeam X-ray analysis of thick polished materials, thin films, and particles. *Microbeam Anal.* **4**, 177–200.
- Bigalke M., Weyer S., Kobza J. and Wilcke W. (2010) Stable Cu and Zn isotope ratios as tracers of sources and transport of Cu and Zn in contaminated soil. *Geochim. Cosmochim. Acta* **74**, 6801–6813.
- Bischoff A., Beckerling W., Weber D. and Zinner E. (1992) Calcium-dialuminate-bearing inclusions from the Saharan meteorites Acfer 182, Acfer 087 and El Djouf001: An ion probe study. *Meteoritics* **27**, 204.
- Bischoff A., Palme H., Schultz L., Weber D., Weber H. W. and Spettel B. (1993) Acfer 182 and paired samples, an iron-rich carbonaceous chondrite: Similarities with ALH85085 and relationship to CR chondrites. *Geochim. Cosmochim. Acta* **57**, 2631–2648.
- Bollard J., Connelly J. N. and Bizzarro M. (2015) Pb-Pb dating of individual chondrules from the CB a chondrite Gujba: Assessment of the impact plume formation model. *Meteorit. Planet. Sci.* **1216**, 1197–1216.
- Bonal L., Huss G. R., Krot A. N. and Nagashima K. (2008) Lithic clasts of CB/CH-like carbonaceous chondrite Isheyevo: Diversity revealed by mineralogy. structure of organic matter and oxygen isotopic composition of carbonates. In *Lunar and Planetary Science Conference* pp. 5–6.
- Boynton W. V. (1975) Fractionation in the solar nebula: Condensation of yttrium and the rare earth elements. *Geochim. Cosmochim. Acta* **39**, 569–584.
- Brearely A. J. and Jones R. H. (1998) Chondritic Meteorites. In *Planetary Materials, Reviews in Mineralogy 36* (ed. J. J. Papike). Mineralogical Society of America. pp. 3, 1–398.
- Budde G., Kruijer T. S. and Kleine T. (2018) Hf-W chronology of CR chondrites: Implications for the timescales of chondrule formation and the distribution of Al in the solar nebula. *Geochim. Cosmochim. Acta* **222**, 284–304.
- Campbell A. J., Humayun M. and Weisberg M. K. (2000) Siderophile element distributions in zoned metal grains in Hammadah al Hamra 237. In *Meteoritical Society Meeting* p. 5291.
- Campbell A. J., Humayun M., Meibom A., Krot A. N. and Keil K. (2001) Origin of zoned metal grains in the QUE94411 chondrite. *Geochim. Cosmochim. Acta* **65**, 163–180.
- Campbell A. J., Humayun M. and Weisberg M. K. (2002) Siderophile element constraints on the formation of metal in the metal-rich chondrites Bencubbin, Weatherford, and Gujba. *Geochim. Cosmochim. Acta* **66**, 647–660.
- Campbell A. J., Humayun M. and Weisberg M. K. (2005) Compositions of unzoned and zoned metal in the CBb chondrites Hammadah al Hamra 237 and Queen Alexandra Range 94627. *Meteorit. Planet. Sci.* **40**, 1131–1148.
- Campbell A. J., Zanda B., Perron C., Meibom A. and Petaev M. I. (2005) Origin and Thermal History of Fe-Ni Metal in Primitive Chondrites. In *Chondrites and the Protoplanetary Disk* pp. 405–431.
- Chernozhukhin S. M., Weyrauch M., Goderis S., Oeser M., Mckibbin S. J., Horn I., Hecht L., Weyer S., Claeys P. and Vanhaecke F. (2017) Thermal equilibration of iron meteorite and pallasite parent bodies recorded at the mineral scale by Fe and Ni isotope systematics. *Geochim. Cosmochim. Acta* **217**, 95–111.
- Chmeleff J., Horn I., Steinhoefel G. and von Blanckenburg F. (2008) In situ determination of precise stable Si isotope ratios by UV-femtosecond laser ablation high-resolution multi-

References

- collector ICP-MS. *Chem. Geol.* **249**, 155–166.
- Clayton R. N. (1980) Chemical and isotopic fractionation by grain size separates. *Earth and Planet. Sci. Lett.* **47**, 199–210.
- Clayton R. N. (1993) Oxygen isotopes in meteorites. *Annu. Rev. Earth Planet. Sci.* **21**, 115–149.
- Clayton R. N. and Mayeda T. K. (1999) Oxygen isotope studies of carbonaceous chondrites. *Geochim. Cosmochim. Acta* **63**, 2089–2104.
- Conolly H. J., Huss G. R. and Wasserburg G. J. (2001) On the formation of Fe-Ni metal in Renazzo-like carbonaceous chondrites. *Geochim. Cosmochim. Acta* **65**, 4567–4588.
- Cook D. L., Wadhwa M., Janney P. E., Dauphas N., Clayton R. N. and Devis A. M. (2006) High precision measurements of non-mass-dependent effects in nickel isotopes in meteoritic metal via multicollector ICPMS. *Anal. Chem.* **78**, 8477–8484.
- Cook D. L., Wadhwa M., Clayton R. N., Dauphas N., Janney P. E. and Davis A. M. (2007) Mass-dependent fractionation of nickel isotopes in meteoritic metal. *Meteorit. Planet. Sci.* **42**, 2067–2077.
- Dauphas N. (2007) Diffusion-driven kinetic isotope effect of Fe and Ni during formation of the Widmanstätten pattern. *Meteorit. Planet. Sci.* **42**, 1597–1613.
- Dauphas N., Poitrasson F., Burkhardt C., Kobayashi H. and Kurosawa K. (2015) Planetary and meteoritic Mg/Si and delta Si-30 variations inherited from solar nebula chemistry. *Earth Planet. Sci. Lett.* **427**, 236–248.
- Dauphas N., John S. G. and Rouxel O. (2017) Iron Isotope Systematics. In *Non-traditional stable isotopes, Reviews in Mineralogy&Geochemistry* 82 pp. 415–510.
- El Goresy A., Lin Y., Miyahara M., Gillet P., Ohtani E., Trierloff M., Simionovici A., Lemelle L., Feng L. and Zhang J. (2016) Metal nodules in EL3 and EH3 primitive chondrites: Conglomerates of micro pebble metals with a menagerie of sulfide assemblages; graphite feathers and various sinoite morphologies, metal clasts. No evidence for melting. In *Meteoritics and Planetary Science Meetings* p. #6144.
- El Goresy A., Ramdohr P. and Rambaldi E. R. (1981) Sulfide-rich chondrule rims in Bishunpur (L3) chondrite: types, textures, mineralogy and genetic implications. In *Lunar and Planetary Science Conference XII* pp. 254–256.
- Elliot T. and Steele R. C. J. (2017) The Isotope Geochemistry of Ni. In *Non-traditional stable isotopes, Reviews in Mineralogy&Geochemistry* 82 (eds. F.-Z. Teng, J. Watkins, and N. Dauphas). Mineralogical Society of America, Geochemical Society. pp. 511–542.
- Fedkin A. V and Grossman L. (2016) Effects of dust enrichment on oxygen fugacity of cosmic gases. *Meteorit. Planet. Sci.* **51**, 843–850.
- Fedkin A. V., Grossman L., Humayun M., Simon S. B. and Campbell A. J. (2015) Condensates from vapor made by impacts between metal-, silicate-rich bodies: Comparison with metal and chondrules in CB chondrites. *Geochim. Cosmochim. Acta* **164**, 236–261.
- Fegley B. and Palme H. (1985) Evidence for oxidizing conditions in the solar nebula from Mo and W depletions in refractory inclusions in carbonaceous chondrites. *Earth Planet. Sci. Lett.* **72**, 311–326.
- Fernández B., Claverie F., Pécheyran C., Donard O. F. X. and Claverie F. (2007) Direct analysis of solid samples by fs-LA-ICP-MS. *TrAC - Trends Anal. Chem.* **26**, 951–966.
- Fitoussi C. and Bourdon B. (2012) Silicon Isotope Evidence Against an Enstatite Chondrite Earth. *Science* **335**, 1477–1480.
- Fitoussi C., Bourdon B., Kleine T., Oberli F. and Reynolds B. C. (2009) Si isotope systematics of meteorites and terrestrial peridotites : implications for Mg / Si fractionation in the solar nebula and for Si in the Earth ' s core. *Earth Planet. Sci. Lett.* **287**, 77–85.
- Franchi I. A., Wright I. P. and Pillinger C. (1986) Heavy nitrogen in Bencubbin - A light-element isotopic anomaly in a stony-iron meteorite. *Nature* **323**, 138–140.
- Georg R. B., Halliday A. N., Schauble E. A. and Reynolds B. C. (2007) Silicon in the Earth's core. *Nature* **447**, 1102–1106.
- Gilbert S., Danyushevsky L., Robinson P., Wohlgemuth-Ueberwasser C., Pearson N., Savard

References

- D., Norman M. and Hanley J. (2013) A Comparative Study of Five Reference Materials and the Lombard Meteorite for the Determination of the Platinum-Group Elements and Gold by LA-ICP-MS. *Geostand. Geoanalytical Res.* **37**, 51–64.
- Goldstein J. I., Jones R. H., Kotula P. G. and Michael J. R. (2007) Microstructure and thermal history of metal particles in CH chondrites. *Meteorit. Planet. Sci.* **42**, 913–933.
- Greshake A., Krot A. N., Meibom A., Weisberg M. K., Zolensky M. E. and Keil K. (2002) Heavily-hydrated lithic clasts in CH chondrites and the related, metal-rich chondrites Queen Alexandra Range 94411 and Hammadah al Hamra 237. *Meteorit. Planet. Sci.* **37**, 281–293.
- Grossman L. and Zipfel J. (2001) The Meteoritical Bulletin , No . 85 , 2001 September. **322**.
- Grossman L., Rubin A. E. and MacPherson G. J. (1988) ALH85085 " a unique volatile-poor carbonaceous chondrite with possible implications for nebular fractionation processes. *Earth Planet. Sci. Lett.* **91**, 33–54.
- Horn I. and von Blanckenburg F. (2007) Investigation on elemental and isotopic fractionation during 196 nm femtosecond laser ablation multiple collector inductively coupled plasma mass spectrometry. *Spectrochim. Acta Part B At. Spectrosc.* **62**, 410–422.
- Horn I., von Blanckenburg F., Schoenberg R., Steinhöfel G. and Markl G. (2006) In situ iron isotope ratio determination using UV-femtosecond laser ablation with application to hydrothermal ore formation processes. *Geochim. Cosmochim. Acta* **70**, 3677–3688.
- Horstmann M., Humayun M. and Bischoff A. (2014) Clues to the origin of metal in Almahata Sitta EL and EH chondrites and implications for primitive E chondrite thermal histories. *Geochim. Cosmochim. Acta* **140**, 720–744.
- Ivanova M. A., Nazarov M. A., Kononkova N. N. and Brandstätter F. (2005) Isheyev: a new CB chondrite. In *Meteoritical Society Meeting* p. 5073.
- Ivanova M. A., Kononkova N. N., Krot A. N., Greenwood R. C., Franchi I. A., Verchovsky A. B., Tieloff M., Korochantseva E. V. and Brandstätter F. (2008) The Isheyev meteorite: Mineralogy, petrology, bulk chemistry, oxygen, nitrogen, carbon isotopic compositions, and 40 Ar- 39 Ar ages. *Meteorit. Planet. Sci.* **43**, 915–940.
- Jackson S. (2008) LAMTRACE Data Reduction Software for LA-ICP-MS. In *Laser Ablation ICP-MS in the Earth Sciences: Current Practices and Outstanding Issues, Mineralogical Association of Canada Short Course Series, vol. 40* (ed. P. Sylvester). Mineralogical Association of Canada. pp. 305–307.
- Jacquet E., Gounelle M. and Alard O. (2012) Trace element microdistribution in carbonaceous chondrite chondrules. In *Lunar and Planetary Science Conference* pp. 2–3.
- Jacquet E., Paulhiac-Pison M., Alard O., Kearsley A. T. and Gounelle M. (2013) Trace element geochemistry of CR chondrite metal. *Meteorit. Planet. Sci.* **48**, 1981–1999.
- Javoy M., Kaminski E., Guyot F., Andrault D., Sanloup C., Moreira M., Labrosse S., Jambon A., Agrinier P., Davaille A. and Jaupart C. (2010) The chemical composition of the Earth: Enstatite chondrite models. *Earth Planet. Sci. Lett.* **239**, 259–268.
- Kallemeyn G. W., Rubin A. E. and Wasson J. T. (2001) Compositional studies of Bencubbin dark silicate host and an OC clast: Relationships to other meteorites and implications for their origin. In *Lunar and Planetary Science Conference* p. 2070.
- Kimura M., El Goresy A., Palme H., and Zinner E. (1993) Ca-, Al-rich inclusions in the unique chondrite ALH85085: Petrology, chemistry, and isotopic compositions.
- Kita N. T., Togashi S., Terashima S., Morishita Y. and Yurimoto H. (1997) In situ Ni isotopic analyses for ureilitic olivine using ion probe. *Lunar Planet. Sci. Conf.* **XXVIII**, 1052.
- Kleine T., Mezger K., Palme H., Scherer E. E. and Münker C. (2005) Early core formation in asteroids and late accretion of chondrite parent bodies: Evidence from 182 Hf- 182 W in CAIs , metal-rich chondrites , and iron meteorites. *Geochim. Cosmochim. Acta* **69**, 5805–5818.
- Krot A. N., Meibom A., Petaev M. I., Zolensky M. E., Saito A., Mukai M. and Oshumi K. (2000) Ferrous silicate spherules with euhedral iron-nickel metal grains from CH carbonaceous chondrites: Evidence for supercooling and condensation under oxidizing

References

- conditions. *Meteorit. Planet. Sci.* **35**, 1249–1258.
- Krot A. N., Meibom A., Russell S. S., Alexander C. M. O. D., Jeffries T. E. and Keil K. (2001) A New Astrophysical Setting for Chondrule Formation. *Science* **291**, 1776–1780.
- Krot A. N., Meibom A., Weisberg M. K. and Keil K. (2002) The CR chondrite clan: Implications for early solar system processes. *Meteorit. Planet. Sci.* **37**, 1451–1490.
- Krot A. N., Amelin Y., Cassen P. and Meibom A. (2005) Young chondrules in CB chondrites from a giant impact in the early Solar System. *Nature* **436**, 989–992.
- Krot A. N., Amelin Y., Bland P., Ciesla F. J., Connelly J., Davis A. M., Huss G. R., Hutcheon I. D., Makide K., Nagashima K., Nyquist L. E., Russell S. S., Scott E. R. D., Thrane K., Yurimoto H. and Yin Q.-Z. (2009) Origin and chronology of chondritic components: A review. *Geochim. Cosmochim. Acta* **73**, 4963–4997.
- Lazarov M. and Horn I. (2015) Matrix and energy effects during in-situ determination of Cu isotope ratios by ultraviolet-femtosecond laser ablation multicollector inductively coupled plasma mass spectrometry. *Spectrochim. Acta Part B At. Spectrosc.* **111**, 64–73.
- Lee M. I. N. S., Rubin A. E. and Wasson J. T. (1992) Origin of metallic Fe-Ni in Renazzo and related chondrites. *Geochim. Cosmochim. Acta* **56**, 2521–2533.
- Leitner J., Hoppe P. and Zipfel J. (2018) A study of presolar material in hydrated lithic clasts from metal-rich carbonaceous chondrites. *Meteorit. Planet. Sci.* **53**, 204–231.
- Lodders K., Palme H. and Gail H. (2009) Abundances of the elements in the Solar System. In *Solar System* pp. 1–59.
- Meibom A., Petaev M. I., Krot A. N., Wood J. a. and Keil K. (1999) Primitive FeNi metal grains in CH carbonaceous chondrites formed by condensation from a gas of solar composition. *J. Geophys. Res. Planets* **104**, 22053–22059.
- Meibom A., Desch S. J., Krot A. N., Cuzzi J. N., Petaev M. I., Wilson L. and Keil K. (2000) Large-Scale Thermal Events in the Solar Nebula : Evidence from Fe , Ni Metal Grains in Primitive Meteorites. *Science* **288**, 839–842.
- Meibom A., Desch S. J., Petaev M. I., Krot A. N., Cuzzi J. N., Wood J. A. and Keil K. (2000) An astrophysical model for the formation of zoned Fe,Ni metal grains in the Bencubbin/CH-like chondrites QUE94411 and Hammadah al Hamra 237. In *Meteoritical Society Meeting* p. 5268.
- Meibom A., Petaev M. I., Alexander N., Keil K. and Wood J. A. (2001) Growth mechanism and additional constraints on FeNi metal condensation in the solar nebula. *J. Geophys. Res.* **106**, 797–801.
- Meibom A., Righter K., Chabot N., Dehn G., Antignano A., McCoy T. J., Krot A. N., Zolensky M. E., Petaev M. I. and Keil K. (2005) Shock melts in QUE 94411, Hammadah al Hamra 237, and Bencubbin: Remains of the missing matrix? *Meteorit. Planet. Sci.* **40**, 1377–1391.
- Merrill B. G. P. (1920) On Chondrules and Chondritic Structure in Meteorites. In *Proceedings of the National Academy of Sciences of the USA* pp. 449–472.
- Narayan C. and Goldstein J. I. (1985) A major revision of iron meteorite cooling rates - An experimental study of the growth of the Widmanstätten pattern. *Geochim. Cosmochim. Acta* **49**, 397–410.
- Newsom H. E. and Drake M. J. (1979) The origin of metal clasts in the Bencubbin meteoritic breccia. *Geochim. Cosmochim. Acta* **43**, 689–707.
- Oeser M., Weyer S., Horn I. and Schuth S. (2014) High-precision Fe and Mg isotope ratios of silicate reference glasses determined in situ by femtosecond LA-MC-ICP-MS and by solution nebulisation MC-ICP-MS. *Geostand. Geoanalytical Res.* **38**, 311–328.
- Oeser M., Dohmen R., Horn I., Schuth S. and Weyer S. (2015) Processes and time scales of magmatic evolution as revealed by Fe – Mg chemical and isotopic zoning in natural olivines. *Geochim. Cosmochim. Acta* **154**, 130–150.
- Oulton J., Humayun M., Fedkin A. and Grossman L. (2016) Chemical evidence for differentiation , evaporation and recondensation from silicate clasts in Gujba. *Geochim. Cosmochim. Acta* **177**, 254–274.

References

- Petaev M. I. and Wood J. A. (2000) The condensation origin of zoned metal grains in Bencubbin/CH-like chondrites: thermodynamic model. In *Lunar and Planetary Science Conference* p. 1608.
- Petaev M. I., Meibom A., Krot A. N. and Wood J. A. (2001) The condensation origin of zoned metal grains in Queen Alexandra Range 94411 : Implications for the formation of the Bencubbin-like chondrites. *Meteorit. Planet. Sci.* **36**, 93–106.
- Petaev M. I., Wood J. A., Meibom A., Krot A. N. and Keil K. (2003) The ZONMET thermodynamic and kinetic model of metal condensation. *Geochim. Cosmochim. Acta* **67**, 1737–1751.
- Poitrasson F. (2017) Silicon Isotope Geochemistry. In *Non-traditional stable isotopes, Reviews in Mineralogy & Geochemistry* 82 pp. 289–344.
- Poitrasson F., Mao X., Mao S. S. and Russo R. E. (2003) Comparison of Ultraviolet Femtosecond and Nanosecond Laser Ablation Inductively Coupled Plasma Mass Spectrometry Analysis in Glass, Monazite, and Zircon. *Anal. Chem.* **75**, 6184–6190.
- Poitrasson F., Levasseur S. and Teutsch N. (2005) Significance of iron isotope mineral fractionation in pallasites and iron meteorites for the core-mantle differentiation of terrestrial planets. *Earth Planet. Sci. Lett.* **234**, 151–164.
- Pouchon J. L. and Pichoir F. (1984) A new model for quantitative X-ray microanalysis. Part 1: application to the analysis of homogenous samples. *Rech. Aerosp.* **3**, 13–38.
- Pringle E. A., Savage P., Jackson M., Barrat J. and Moynier F. (2013) Si isotope homogeneity of the solar nebula. *Astrophys. J.* **779**, 123–127.
- Pringle E. A., Moynier F., Savage P., Badro J. and Barrat J. (2014) Silicon isotopes in angrites and volatile loss in planetesimals. *PNAS* **111**, 17029–17032.
- Reed S. J. B. (1965) Electron-probe microanalysis of the metallic phases in iron meteorites. *Geochim. Cosmochim. Acta* **29**, 535–549.
- Richter F. M., Liang Y. and Davis A. M. (1999) Isotope fractionation by diffusion in molten oxides. *Geochim. Cosmochim. Acta* **63**, 2853–2861.
- Richter F. M., Davis A. M., DePaolo D. J. and Watson E. B. (2003) Isotope fractionation by chemical diffusion between molten basalt and rhyolite. *Geochim. Cosmochim. Acta* **67**, 3905–3923.
- Richter F. M., Dauphas N. and Teng F. Z. (2009) Non-traditional fractionation of non-traditional isotopes: Evaporation, chemical diffusion and Soret diffusion. *Chem. Geol.* **258**, 92–103.
- Richter F. M., Huss G. R. and Mendybaev R. A. (2014) Iron and nickel isotopic fractionation across metal grains from three CBb. *Lunar Planet. Sci. Conf.* **XLV**, 1346.pdf.
- Righter K. and Chabot N. (1998) Silicate and metal phases in the Queen Alexandra Range 94411 iron meteorite. *Meteorit. Planet. Sci.* **33**, A129.
- Rubin A. E., Kallemeyn G. W., Wasson J. T., Clayton R. N., Mayeda T. K., Grady M. and Verchovsky A. B. (2001) Gujba: a new Bencubbin-like meteorite fall from Nigeria. In p. 1779.
- Rubin A. E., Kallemeyn G. W., Wasson J. T., Clayton R. N., Mayeda T. K., Grady M., Verchovsky A. B., Eugster O. and Lorenzetti S. (2003) Formation of metal and silicate globules in Gujba: A new Bencubbin-like meteorite fall. *Geochim. Cosmochim. Acta* **67**, 3283–3298.
- Russell S. S., Krot A. N., Meibom A., Alexander C. M. O. D. and Jeffries T. E. (2000) Chondrules of the first generation? Trace element geochemistry of silicates from Bencubbin/CH-like meteorites. In *Meteoritical Society Meeting* p. 5249.
- Sanders I. S. and Scott E. R. D. (2012) The origin of chondrules and chondrites: Debris from low-velocity impacts between molten planetesimals? *Meteorit. Planet. Sci.* **47**, 2170–2192.
- Savage P. and Moynier F. (2013) Silicon isotopic variation in enstatite meteorites: Clues to their origin and Earth-forming material. *Earth Planet. Sci. Lett.* **361**.
- Schauble E. A. (2004) Applying Stable Isotope Fractionation Theory to New Systems. *Rev.*

References

- Mineral. Geochemistry* **55**, 65–111.
- Shu F. H. (2001) The X-Wind Theory for the Origin of Chondritic Meteorites. In *Goldschmidt Conference* p. 3700.
- Sio C. K. I., Dauphas N., Teng F., Chaussidon M., Helz R. T. and Roskosz M. (2013) Discerning crystal growth from diffusion profiles in zoned olivine by in situ Mg – Fe isotopic analyses. *Geochim. Cosmochim. Acta* **123**, 302–321.
- Steinhoefel G., Horn I. and von Blanckenburg F. (2009) Micro-scale tracing of Fe and Si isotope signatures in banded iron formation using femtosecond laser ablation. *Geochim. Cosmochim. Acta* **73**, 5343–5360.
- Trinquier A., Elliott T., Ulfbeck D., Coath C., Krot A. N. and Bizzarro M. (2009) Origin of Nucleosynthetic Isotope Heterogeneity in the Solar Protoplanetary Disk. **324**, 374–377.
- Van Kooten E. M. M. E., Wieland D., Schiller M., Nagashima K., Thomen A., Larsen K. K., Olsen M. B., Nordlund A., Krot A. N. and Bizzarro M. (2016) Isotopic evidence for primordial molecular cloud material in metal-rich carbonaceous chondrites. *PNAS* **113**, 2011–2016.
- Warren P. H. (2011) Stable-isotopic anomalies and the accretionary assemblage of the Earth and Mars : A subordinate role for carbonaceous chondrites. *Earth Planet. Sci. Lett.* **311**, 93–100.
- Wasson J. T. and Kallemeyn G. W. (1990) Allan Hills 85085: A subchondritic meteorite of mixed nebular and regolithic heritage. *Earth Planet. Sci. Lett.* **101**, 148–161.
- Weisberg M. K. and Prinz M. (1999) Zoned metal in the CR clan chondrites. In *24th Symposium on Antarctic Meteorites* pp. 187–189.
- Weisberg M. K., Prinz M., Clayton R. N. and Mayeda T. K. (1993) The CR (Renazzo-type) carbonaceous chondrite group and its implications. *Geochim. Cosmochim. Acta* **57**, 1567–1586.
- Weisberg M. K., Prinz M., Clayton R. N., Mayeda T. K., Grady M. and Pillinger C. (1995) The CR Chondrite Clan. In *Proc. NIPR Symp. Anarct. Meteorites* 8 pp. 11–32.
- Weisberg M. K., Prinz M., Clayton R. N., Mayeda T. K., Sugiura N., Zashu S. and Ebihara M. (2001) A new metal-rich chondrite grouplet. *Meteorit. Planet. Sci.* **36**, 401–418.
- Weyer S. and Schwieters J. (2003) High precision Fe isotope measurements with high mass resolution MC-ICPMS. *Int. J. Mass Spectrom.* **226**, 355–368.
- Weyrauch M. and Bischoff A. (2012) Macrochondrules in chondrites - Formation by melting of mega-sized dust aggregates and/or by rapid collisions at high temperatures? *Meteorit. Planet. Sci.* **47**, 2237–2250.
- Weyrauch M., Oeser M., Brueske A. and Weyer S. (2017) In situ high-precision Ni isotope analysis of metals by femtosecond-LA-MC-ICP-MS. *J. Anal. At. Spectrometry* **32**, 1312–1319.
- White W. M. (2001) Stable Isotope Geochemistry. In *Geochemistry* pp. 361–420.
- Young E. D., Galy A. and Nagahara H. (2002) Kinetic and equilibrium mass-dependent isotope fractionation laws in nature and their geochemical and cosmochemical significance. *Geochim. Cosmochim. Acta* **66**, 1095–1104.
- Zanda B., Bourot-Denise M., Perron C. and Hewins R. H. (1994) Origin and Metamorphic Redistribution of Silicon , Chromium , and Phosphorus in the Metal of Chondrites. *Science (80-.)*. **265**, 1846–1849.
- Zanda B., Hewins R. H., Cohen B. A., Delaney J. S., Humayun M. and Campbell A. J. (2002) Accretion textures, iron evaporation and re-condensation in Renazzo chondrules. In *Lunar and Planetary Science Conference* p. #1852.
- Zipfel J. and Weyer S. (2007) In situ analyses of Fe isotopes in zoned metall grains of Hammadah al Hamra 237. In *Lunar and Planetary Science Conference* p. 1984.
- Zipfel J., Wlotzka F. and Spettel B. (1998) Bulk chemistry and mineralogy of a new “unique” metal-rich chondritic breccia, Hammadah al Hamra 237. In *Lunar and Planetary Science Conference* p. 1417.

Appendix

Appendix

1 APPENDIX PART I

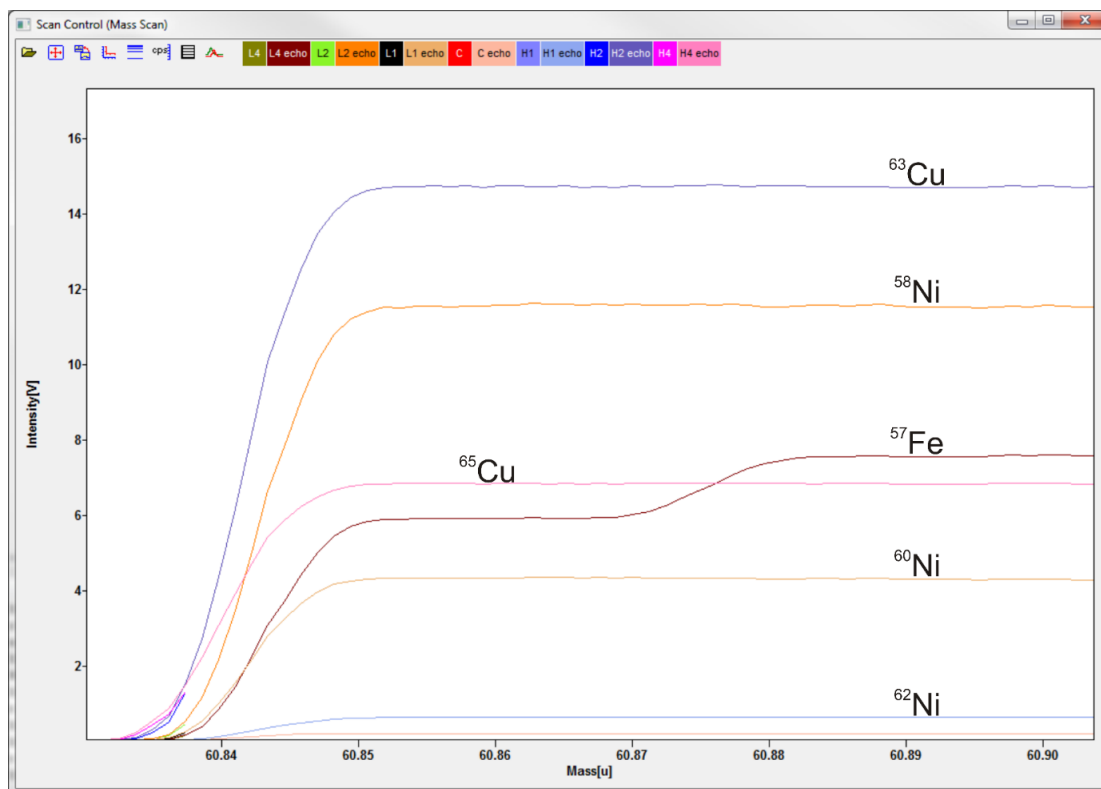


Figure S1: Image of a mass scan during fs-LA-MC-ICP-MS measurement on a Ni standard. The mass scan reveals that all Ni and Cu isotopes, as well as ^{57}Fe can be measured free from argide or oxide interferences. The measured isotopes are written above the respective lines. The lowest line displays the intensity of ^{61}Ni .



Figure S2: This photograph displays a copper spacer with a thickness of 0.8 mm. The spacer enhances the intensities by increasing the distance between the sample cone and the skimmer cone.

Appendix

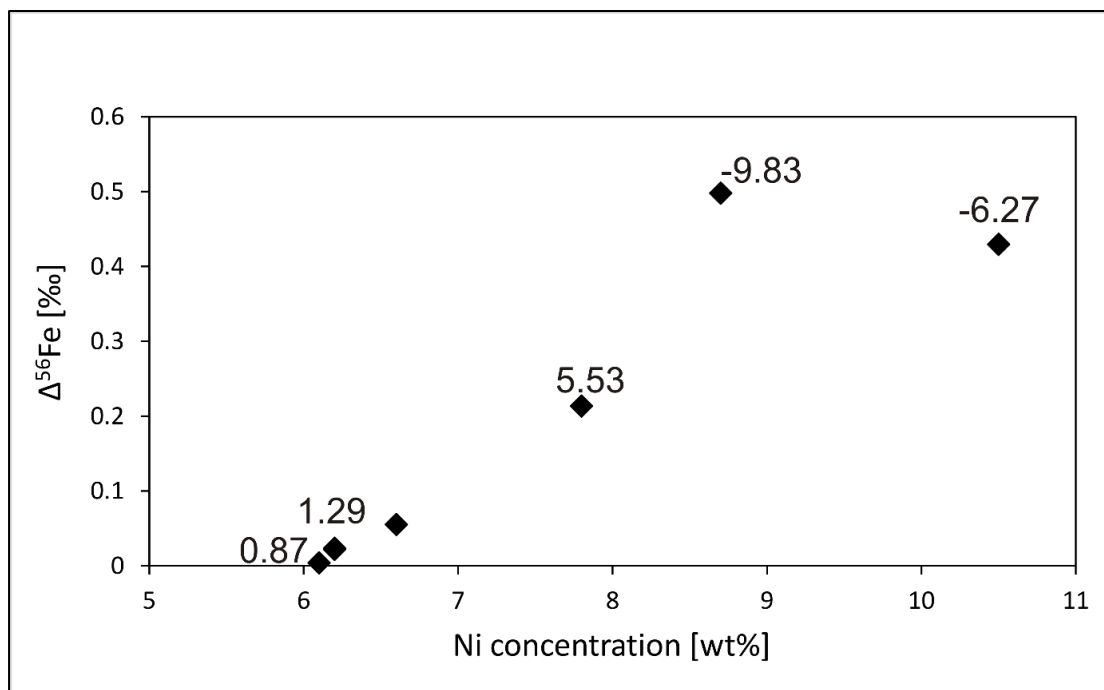


Figure S3: This diagram shows the offset of the measured $\delta^{56}\text{Fe}$, if the Ni mass bias was monitored simultaneously to Fe isotope analyses with LA-MC-ICP-MS, relative to an “interpolation method” for which Ni mass bias was monitored before and after Fe isotope analyses and applied to the bracketed Fe isotope analyses (see text for further explanation). The offset, shown as $\Delta^{56}\text{Fe}$ is plotted against the Ni concentration of the respective sample. The numbers given with the data points are the $\delta^{62/60}\text{Ni}$ values of the grains. Samples with more than ~ 7 wt% and a Ni isotope composition that differs by more than ~ 1.5 ‰ from that of the Ni standard generate an offset in the analyzed Fe isotope composition ($\Delta^{56}\text{Fe}$) outside the analytical uncertainty (0.1 ‰), i.e. for those samples, the “interpolation method” needs to be performed.

Table S1: Cup configuration of bulk solution nebulization and laser ablation MC-ICP-MS analyses for Ni.

Cup configuration for Ni isotope analyses							
cup	L4	L2	L1	C	H1	H2	H4
isotope	^{57}Fe	^{58}Ni	^{60}Ni	^{61}Ni	^{62}Ni	^{63}Cu	^{65}Cu

Table S2: Typical instrument settings of the MC-ICP-MS during laser ablation measurements.

Instrumental settings of Neptune Plus for LA-MC-ICP-MS analyses	
Cool gas: Ar (l min ⁻¹)	15
Aux gas: Ar (l min ⁻¹)	0.86
Sample gas: Ar (l min ⁻¹)	0.885
Carrier gas: He (l min ⁻¹)	0.49
nebulizer uptake rate ($\mu\text{l min}^{-1}$)	100
RF generator power (W)	1210
Accelerator voltage (V)	-10000
Extraction (V)	1898
Focus (V)	-590

Appendix

Table S3: $\delta^{62}\text{Ni}$ of single analyses of the Ni-rod and BAM-D184.1 measured in bracketing with NIST RM 1226 and re-calculated to SRM 986.

$\delta^{62}\text{Ni}$ [‰]			
BAM (RM 1226)	BAM (SRM 986)	Ni-rod (RM 1226)	Ni-rod (SRM 986)
0.31	0.03	-0.01	-0.29
0.42	0.14	0.02	-0.26
0.29	0.01	0.09	-0.19
0.40	0.13	-0.03	-0.31
0.35	0.07	0.01	-0.27
0.41	0.13	0.02	-0.26
0.36	0.08	0.00	-0.28
0.30	0.02		
0.37	0.09		
0.45	0.17		
0.34	0.06		
0.42	0.14		
0.38	0.10		
0.32	0.04		
0.36	0.08		
0.38	0.10		
0.39	0.11		
0.40	0.12		
0.38	0.10		
0.37	0.09		
0.34	0.06		
0.30	0.02		
0.35	0.07		
0.46	0.18		
0.34	0.06		
0.32	0.04		
0.35	0.07		
0.33	0.05		
0.35	0.07		
0.38	0.10		
0.44	0.16		
0.38	0.10		
0.41	0.13		
0.38	0.10		
0.34	0.06		
0.40	0.12		
0.38	0.10		
0.38	0.10		

Appendix

2 APPENDIX PART II

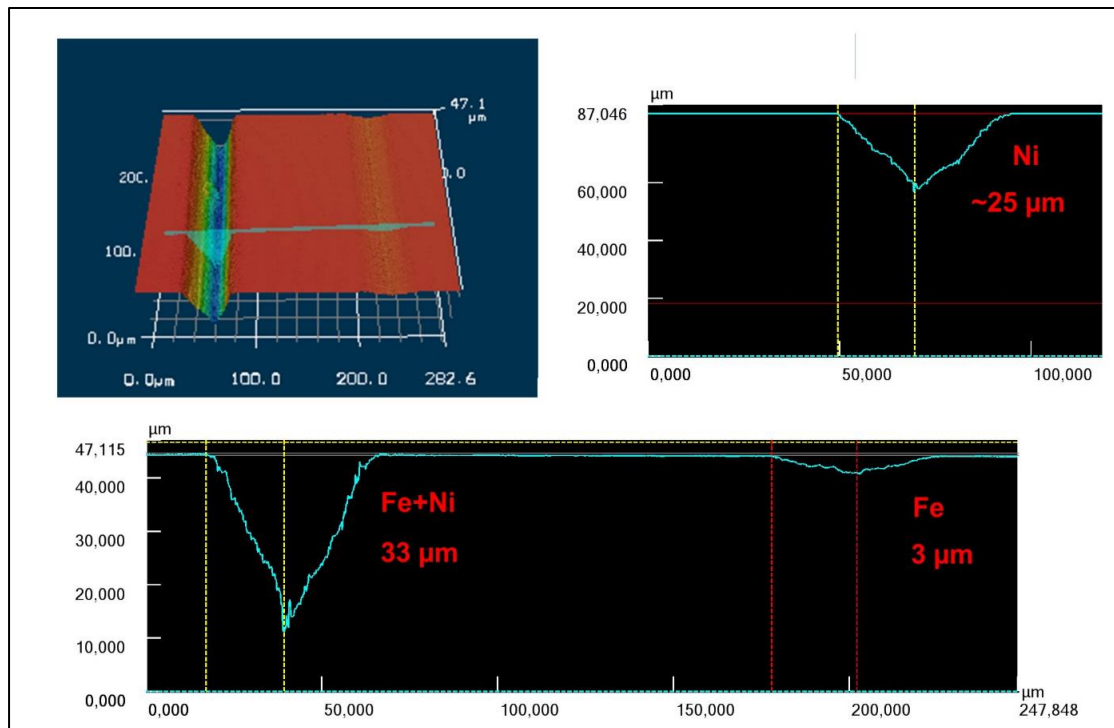


Figure S1: Laser ablation tracks observed with a 3D confocal laser microscope. Nickel isotope measurements leave laser pits that are much deeper than tracks left by Fe isotope analyses.

Appendix

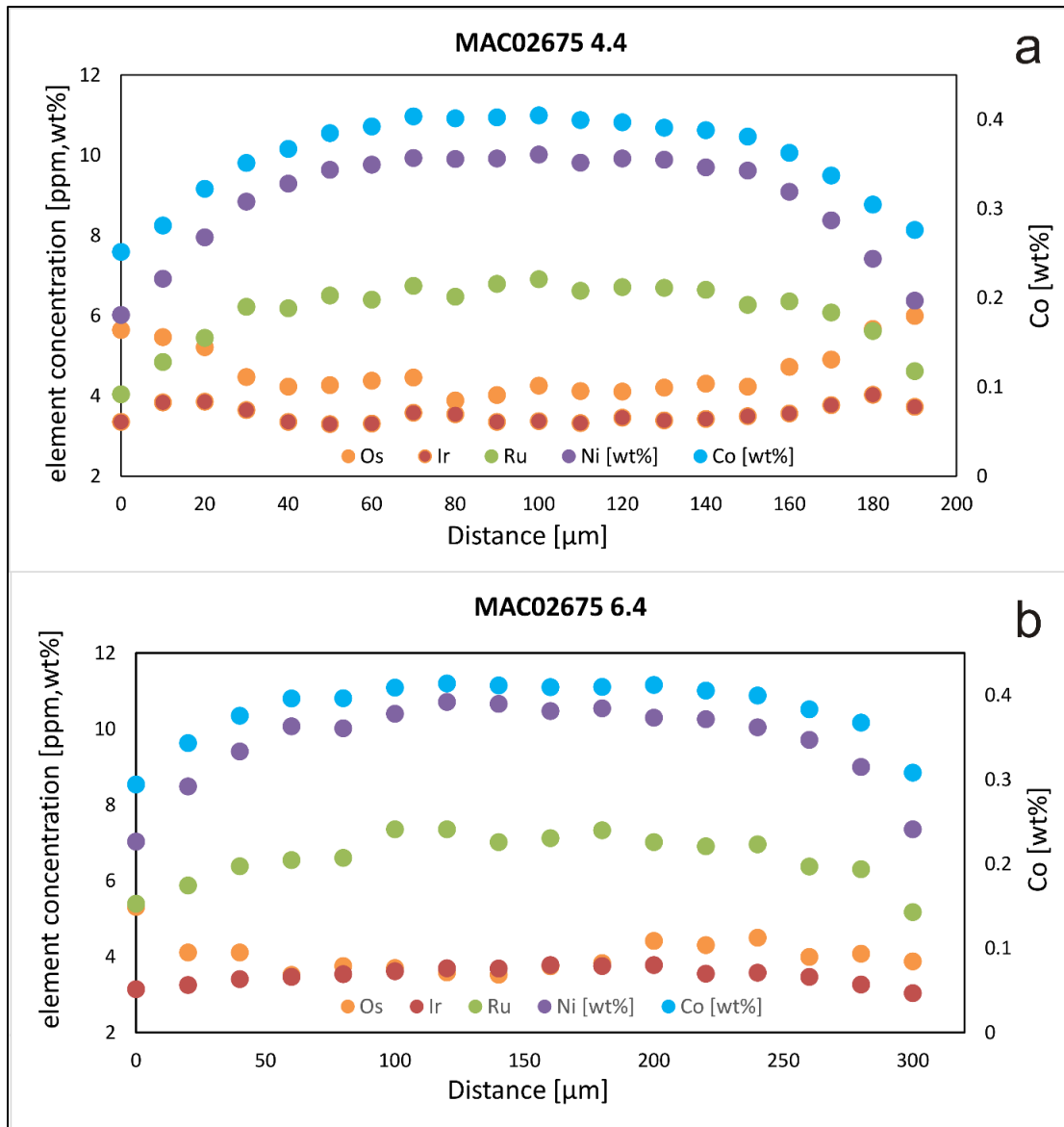


Figure S2: Refractory siderophile element profiles in zoned metal grains that are differing from the most common type (Fig. 2b). a) Zoning of Ni and Co are as in all zoned metals with high contents in the core and lower concentrations in rims. However, Ir and Os do not follow the trend of Ni, but are zoned reversely. Only Ru is following the trend of Ni. b) Nickel and Co are zoned with higher concentrations in the core and lower contents in the rims. Iridium and Osmium are not following that trend, but are showing flat patterns. Only Ru follows the trend of Ni.

Appendix

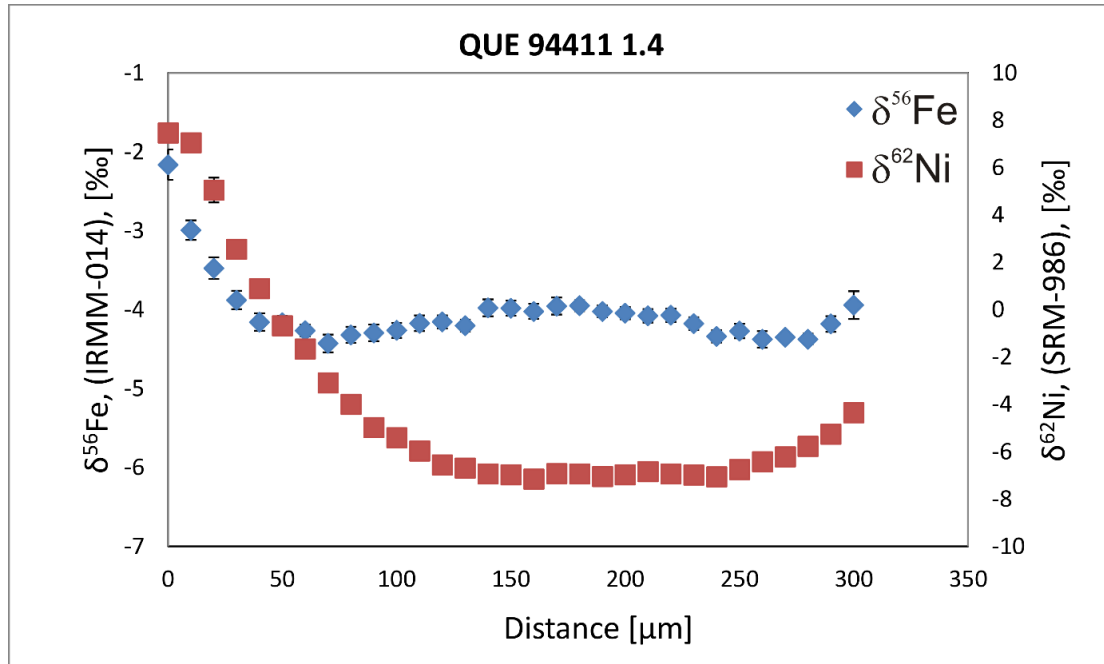


Figure S3: Isotope profiles of QUE94411_1.4, Ni isotopes are lighter in the core than in rims and show a bowl-shaped structure. Iron isotopes show a weak w-shaped profile. The lightest composition is not in the very core.

Table S1: List of peak and background measurement time (s) for all elements analyzed with EMPA in Frankfurt or Hannover. Mean detection limits (DL in wt%) are also summarized.

	Frankfurt			Hannover		
	background (s)	peak (s)	DL (wt%)	background (s)	peak (s)	DL (wt%)
Si	80	80	0.01	15	30	0.03
P	80	80	0.02	10	20	0.02
Ni	20	10	0.02	10	20	0.14
S	10	10	0.01	10	20	0.02
Co	40	20	0.02	10	20	0.12
Fe	60	30	0.02	10	20	0.12
Cr	40	20	0.02	10	20	0.07

Appendix

Table S2: Isotope and chemical compositions of all analyzed zoned metal grains.

Sample	grain	$\delta^{56}\text{Fe}$	$\delta^{62}\text{Ni}$	Ge	Cu	Au	Fe [wt%]	Pd	Co [wt%]	Ni [wt%]	Pt	Mo	Ru	Ir	W	O
HaH 237	9.1 core	-1.28 ± 0.08	-3.08 ± 0.23	0.24	0.26	0.00	86.52	6.20	0.47	13.00	15.15	9.90	12.37	7.69	0.22	
	9.1 rim	1.78 ± 0.11	1.98 ± 0.19	0.05	1.80	0.02	91.65	5.00	0.33	8.02	8.15	7.03	5.58	3.97	0.16	
	9.4 core	-3.74 ± 0.07	-6.34 ± 0.19	-0.06	0.45	0.00	85.84	6.25	0.50	13.66	13.40	10.90	11.37	6.87	0.12	
	9.4 rim	-2.03 ± 0.16	-2.2 ± 0.31	0.20	0.57	-0.01	90.79	5.27	0.36	8.85	7.83	8.08	6.23	4.14	0.15	
	10.5 core	-5.45 ± 0.1	-6.16 ± 0.18	0.14	0.34	0.02	84.97	6.17	0.52	14.51	18.01	11.75	15.88	9.82	0.19	1
	10.5 rim	-3.12 ± 0.43	1.71 ± 0.38	0.36	1.37	0.05	93.57	4.80	0.27	6.15	5.94	4.56	4.08	3.01	0.11	
QUE 94411	3.3 core	-3.50 ± 0.09	-2.31 ± 0.18	0.37	1.27	0.04	87.59	5.80	0.46	11.94	15.39	21.73	11.58	7.37	1.39	
	3.3 rim	2.30 ± 0.08	0.91 ± 0.32	0.21	0.96	0.04	91.65	5.06	0.34	8.01	7.57	7.05	5.56	3.97	0.20	
	1.3 core	-3.93 ± 0.11	-6.27 ± 0.16	0.10	0.84	0.01	88.19	6.18	0.43	11.37	9.89	9.65	8.88	5.03	0.13	
	1.3 rim	-0.36 ± 0.19	3.83 ± 0.32	b.d.	1.02	0.03	92.25	5.19	0.30	7.44	8.97	6.75	5.80	4.57	0.20	
	1.4 core	-4.04 ± 0.08	-6.97 ± 0.15	0.08	1.18	0.04	89.46	5.29	0.40	10.14	8.69	10.59	7.35	4.65	0.25	
	1.4 rim	-2.16 ± 0.19	5.05 ± 0.52	0.28	1.11	0.04	91.06	5.28	0.35	8.58	7.77	7.73	6.27	3.94	0.11	
	2.5 core	-5.25 ± 0.10	-9.83 ± 0.17	-0.09	0.89	0.02	90.60	5.05	0.36	9.04	7.40	6.42	6.04	3.51	0.10	
	2.5 rim	-0.31 ± 0.38	-1.79 ± 0.37	0.52	8.42	0.14	92.54	5.14	0.29	7.16	7.67	5.38	5.11	3.85	0.15	
	4.4 core	-7.41 ± 0.07	-10.85 ± 0.26	0.14	0.60	0.01	89.57	5.05	0.40	10.02	7.04	7.07	6.91	3.37	0.05	
	4.4 rim	-0.2 ± 0.32	-2.31 ± 0.46	2.46	27.07	0.49	93.34	5.41	0.28	6.38	7.11	5.95	4.62	3.73	0.18	
MAC 02675	4.1 core	-3.71 ± 0.12	-2.26 ± 0.26	0.11	2.49	0.04	90.61	5.88	0.37	9.02	7.96	6.83	6.27	3.96	0.17	
	4.1 rim	0.71 ± 0.15	0.08 ± 0.38	1.31	23.35	0.29	95.38	4.59	0.20	4.42	4.96	3.95	2.81	2.41	0.21	
	6.6 core	-4.27 ± 0.09	-5.24 ± 0.16	0.12	0.34	0.02	87.07	6.67	0.46	12.47	11.60	9.96	10.30	6.13	0.14	
	6.6 rim	-0.71 ± 0.28	-3.76 ± 0.13	0.18	4.60	0.05	92.80	4.79	0.29	6.90	6.25	7.40	4.46	3.37	0.19	
	1.2 core	-5.21 ± 0.13	-6.11 ± 0.17	0.21	0.72	0.03	87.48	5.26	0.45	12.06	11.81	8.85	10.23	6.36	0.09	
	1.2 rim	-2.75 ± 0.12	-3.19 ± 0.28	0.47	11.55	0.15	91.96	4.92	0.32	7.71	6.99	6.71	5.50	3.18	0.17	
	6.1 core	-6.49 ± 0.09	-8.39 ± 0.22	0.22	0.43	0.01	88.44	5.24	0.43	11.13	7.96	8.11	7.82	3.85	0.11	
	6.1 rim	-1.26 ± 0.21	-7.68 ± 0.18	0.08	1.75	0.01	90.90	4.86	0.35	8.74	6.74	6.55	6.06	3.47	0.06	
	6.4 core	-6.11 ± 0.13	-9.92 ± 0.20	0.25	0.56	0.01	88.87	5.17	0.41	10.72	7.36	9.26	7.36	3.70	0.12	
	6.4 rim	-1.82 ± 0.19	-7.60 ± 0.20	0.15	5.68	0.03	90.62	5.07	0.37	9.00	6.75	8.19	6.31	3.27	0.25	
Isheyevo	2.7 core	-2.72 ± 0.09	-4.62 ± 0.09	0.28	2.92	0.11	91.91	5.11	0.31	7.78	8.27	7.19	5.70	4.12	0.18	
	2.7 rim	0.75 ± 0.19	-0.76 ± 0.38	2.59	20.47	0.21	92.83	5.11	0.28	6.89	6.90	6.74	4.56	3.77	0.20	
	2.6 core	-3.49 ± 0.13	-5.01 ± 0.18	-0.13	0.54	0.07	91.67	4.80	0.35	7.98	6.35	9.46	5.60	3.32	2.91	
	2.6 rim	-2.29 ± 0.13	-2.76 ± 0.31	0.10	2.21	0.03	92.29	4.76	0.33	7.38	6.44	9.98	5.62	3.25	2.94	

Appendix

Table S3: Isotope and chemical compositions of all analyzed unzoned metal grains. Values are given in ppm, except for Fe, Ni, Co, Cr, Si, and P which are given in wt%.

sample	grain	$\delta^{56}\text{Fe}$ [‰]	$\delta^{62/60}\text{Ni}$ [‰]	Re	Os	W	Ir	Mo	Ru	Pt	Fe	Co	Ni	Cr	Pd	Au	Cu	Ge	Si	P
Gujba	2.10	-1.03 ± 0.04	-1.22 ± 0.05	0.30	4.55	1.12	3.42	9.12	5.31	7.91	91.20	0.32	7.85	0.34	5.31	1.43	6.49	0.49	0.06	0.31
	2.1.5	0.61 ± 0.04	1.23 ± 0.05	0.24	3.73	0.76	2.69	5.78	3.88	5.45	92.60	0.27	6.52	0.09	4.96	0.60	69.10	1.19	0.05	0.27
	2.1.1	0.60 ± 0.05	0.82 ± 0.08	0.24	3.77	0.81	2.66	5.78	3.80	5.57	92.79	0.27	6.57	0.10	4.89	0.75	69.00	1.29	0.05	0.28
	2.1.12	0.54 ± 0.04	0.80 ± 0.09	0.25	3.84	0.85	2.72	6.07	3.78	5.51	92.58	0.27	6.49	0.12	4.98	1.16	70.20	1.29	0.05	0.28
	2.1.3	0.47 ± 0.04	0.86 ± 0.11	0.25	3.84	0.85	2.72	6.07	3.78	5.51	92.65	0.28	6.52	0.11	4.92	0.60	71.70	1.15	0.05	0.26
Bencubbin	2.1.7	0.03 ± 0.04	0.91 ± 0.05	0.24	3.38	0.18	1.76	3.11	2.36	3.19	92.65	0.24	5.54	0.14	3.75	0.41	68.10	0.97	0.06	0.29
	2.1.2	0.06 ± 0.04	0.85 ± 0.05	0.25	3.31	0.18	1.78	3.08	2.30	3.10	92.34	0.24	5.57	0.17	3.73	0.41	69.40	1.00	0.06	0.29
	2.1.3	0.16 ± 0.04	0.97 ± 0.05	0.24	3.23	0.16	1.72	3.14	2.22	3.07	93.15	0.24	5.44	0.19	3.72	0.38	68.30	0.85	0.06	0.28
	2.3.5	-1.46 ± 0.04	0.16 ± 0.05	0.27	4.00	0.97	2.90	6.00	3.89	5.49	90.98	0.26	6.18	0.43	4.43	0.16	5.03	0.38	0.08	0.37
	2.3.9	0.09 ± 0.04	1.20 ± 0.05	0.38	5.74	1.06	4.01	8.16	5.21	7.75	91.59	0.28	6.60	0.28	5.26	0.37	98.90	1.02	0.06	0.22
NWA 4025	2.2.1	0.01 ± 0.04	0.93 ± 0.05	0.32	5.08	2.03	3.84	9.74	5.12	7.53	91.70	0.27	6.39	0.16	4.88	0.46	59.10	0.72	0.06	0.23
	3	-0.94 ± 0.05	0.56 ± 0.09	0.31	4.50	0.34	3.27	6.88	4.76	6.45	93.36	0.31	6.80	bd	4.92	0.10	1.54	0.17	0.03	0.24
	1	-0.13 ± 0.05	0.67 ± 0.1	0.17	2.35	0.23	1.18	2.84	1.72	2.10	95.39	0.28	5.10	bd	3.67	0.49	188.00	1.21	0.02	0.29
	2.3	-0.11 ± 0.05	0.64 ± 0.1	0.19	2.50	0.26	1.21	3.01	1.84	2.25	94.49	0.27	5.47	bd	3.90	0.52	159.00	1.43	0.02	0.28
	4	-0.02 ± 0.05	1.04 ± 0.1	0.55	8.26	1.45	5.81	11.70	7.22	10.60	93.25	0.31	6.62	bd	5.28	0.28	8.36	0.36	0.04	0.26
QUE 94411	5	0.04 ± 0.05	0.92 ± 0.11	0.37	5.49	1.12	3.94	7.68	5.06	7.41	94.18	0.29	5.87	bd	4.33	0.44	62.00	0.88	0.03	0.14
	6	-0.60 ± 0.05	0.56 ± 0.1	0.28	4.07	1.81	2.95	7.45	4.28	5.86	93.76	0.31	6.34	bd	4.48	0.13	2.56	0.17	0.03	0.14
	7.1	0.02 ± 0.05	1.06 ± 0.1	0.38	5.31	1.22	3.83	8.04	5.19	7.35	93.29	0.30	5.96	bd	4.37	0.37	50.10	0.73	0.02	0.13
	8	-1.50 ± 0.05	-2.47 ± 0.1	0.32	4.29	1.66	3.27	10.00	5.29	6.54	92.24	0.36	7.77	bd	5.19	0.10	1.34	0.17	0.03	0.30
	3.1	-1.58 ± 0.04	-2.44 ± 0.06	0.32	4.48	0.24	3.40	6.77	5.34	6.79	92.37	0.31	7.31	NA	4.77	0.12	4.38	0.39	NA	NA
MAC 02675	1.1	0.29 ± 0.04	0.83 ± 0.06	0.37	5.15	1.14	3.73	7.60	5.12	7.30	92.81	0.29	6.89	NA	5.19	0.39	65.25	1.29	NA	NA
	1.3	-0.38 ± 0.04	5.84 ± 0.19	0.32	4.40	0.24	3.06	5.63	3.95	5.95	94.70	0.23	5.07	NA	3.94	0.06	8.85	0.96	0.02	0.13
	6.2	-1.71 ± 0.04	-1.06 ± 0.07	0.32	4.46	1.28	3.30	8.14	5.23	6.45	92.05	0.31	7.64	NA	5.28	0.20	11.17	0.86	NA	NA
	6.3	1.59 ± 0.04	4.37 ± 0.08	0.28	4.05	0.49	2.87	9.98	4.05	5.66	94.14	0.26	5.60	NA	4.37	0.22	11.16	0.44	0.02	0.15
	big	0.18 ± 0.04	0.44 ± 0.08	0.20	2.72	0.50	1.93	3.61	2.95	3.78	93.34	0.28	6.37	NA	4.54	0.44	79.80	0.93	NA	NA
Hammadah 96	4.2	-0.11 ± 0.04	0.28 ± 0.08	0.26	3.69	0.92	2.48	5.49	3.50	4.87	93.79	0.26	5.94	NA	4.41	0.38	31.27	0.74	NA	NA
	4.3	0.23 ± 0.04	0.95 ± 0.08	0.36	5.17	0.63	3.97	6.35	5.46	7.86	93.09	0.28	6.62	NA	5.16	0.47	34.48	2.05	NA	NA
	9.6	-0.10 ± 0.05	0.77 ± 0.08	1.00	13.89	1.42	10.11	13.96	12.63	19.89	93.42	0.29	6.27	NA	4.75	0.34	131.54	2.35	NA	NA
	9.7	-0.23 ± 0.04	0.08 ± 0.07	0.04	0.49	0.05	0.28	0.34	0.67	0.55	94.01	0.26	5.73	NA	4.17	0.24	11.09	0.66	NA	NA
	10.2	-0.18 ± 0.04	1.93 ± 0.06	0.88	13.17	4.10	9.75	21.28	13.04	19.34	91.49	0.33	8.17	NA	6.33	0.16	4.34	0.13	0.05	0.30
Isheyevo	10.4	-2.08 ± 0.04	2.57 ± 0.07	0.35	4.87	1.24	3.78	9.75	5.73	7.67	91.66	0.34	7.99	NA	5.75	0.11	6.90	1.04	0.05	0.30
	2.3	0.14 ± 0.05	1.29 ± 0.07	0.08	0.90	0.48	0.70	2.70	1.62	1.74	93.31	0.28	6.40	0.13	4.62	0.22	53.14	1.02	bd	0.22
	2.4	0.00 ± 0.05	0.87 ± 0.08	0.24	3.26	0.77	2.37	4.24	3.49	4.89	93.29	0.29	6.39	0.03	4.85	0.80	327.24	4.61	bd	0.22
	1.1	0.40 ± 0.04	0.83 ± 0.07	0.29	3.93	0.89	2.86	5.96	4.09	5.77	93.02	0.29	6.68	0.17	4.93	0.38	59.40	0.80	bd	0.25
	1.4	-0.35 ± 0.05	5.53 ± 0.08	0.55	7.54	0.02	5.67	0.95	8.62	11.10	91.28	0.31	8.40	0.52	5.81	0.07	2.73	0.29	bd	0.13

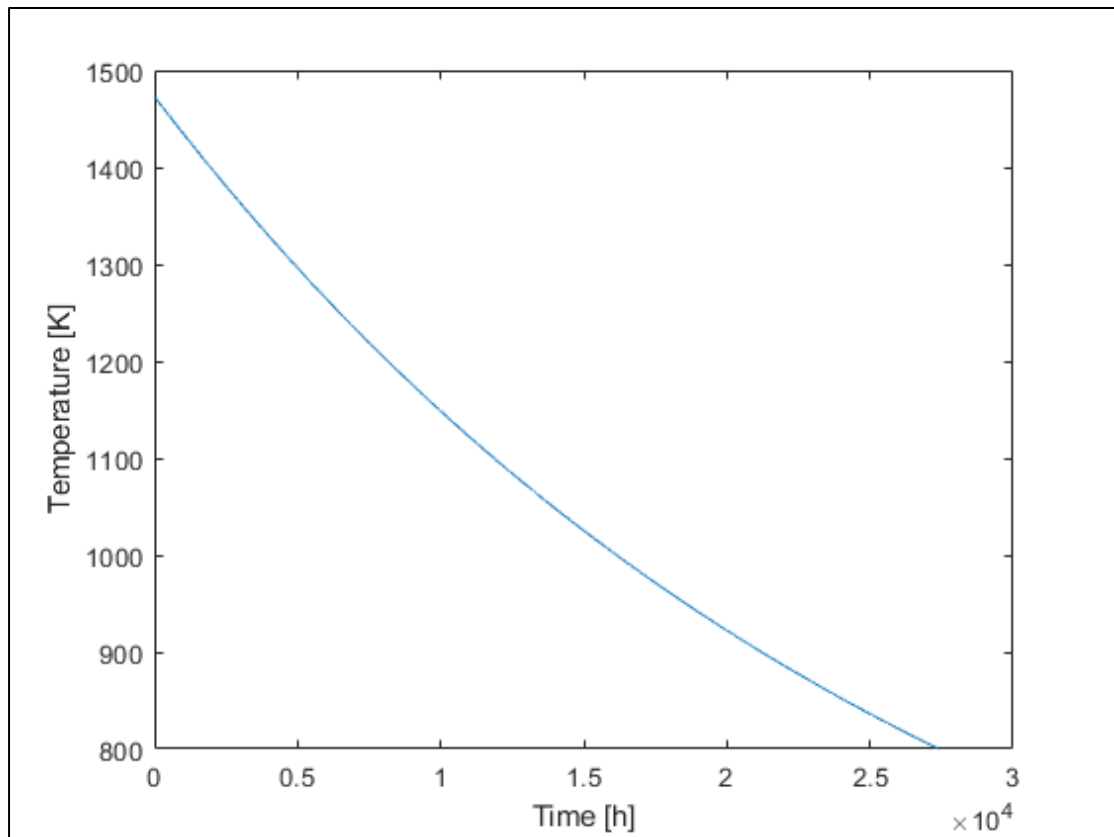
Appendix**3 APPENDIX PART III**

Figure S1: This diagram shows the evolution of the temperature (K) over the time (h) the modeled zoned metal condenses.

Appendix

Table S1: Isotope and element compositions of unzoned metal grains from CH chondrites. Isotope values are given in ‰, element abundances in ppm if not declared differently. NA= data not available.

sample	$\delta^{56}\text{Fe}$	2σ	$\delta^{57}\text{Fe}$	2σ	$\delta^{62}\text{Ni}$	2σ	$\delta^{61}\text{Ni}$	2σ	Ge	Cu	Au	Fe (wt%)	Pd	Co (wt%)	Ni (wt%)	Pt	Mo	Ru	Ir	W	Os	Re
PAT 5.1	-3.42	0.05	-5.12	0.08	-6.87	0.08	-3.40	0.16	0.49	6.46	0.84	90.36	6.32	0.37	9.26	7.08	2.65	6.74	3.60	0.41	4.69	0.36
PAT 4.3	-0.73	0.05	-1.00	0.09	-4.38	0.15	-1.85	0.35	0.52	3.44	5.51	93.24	0.04	0.49	6.26	2.96	61.25	1.14	1.00	14.52	0.05	0.01
PAT 4.1	0.75	0.05	1.12	0.09	-0.18	0.18	-0.03	0.48	0.40	8.22	1.70	93.98	4.14	0.28	5.74	5.50	6.44	4.04	2.79	0.42	3.83	0.26
Acer 5.6	2.35	0.06	3.53	0.11	4.68	0.08	2.29	0.16	1.60	10.71	0.17	94.76	4.14	0.25	4.99	5.20	10.85	3.81	2.64	0.61	3.83	0.27
Acer 2.2	0.24	0.06	0.35	0.13	0.50	0.08	0.42	0.17	NA	NA	NA	NA	NA	NA	NA	NA	NA	NA	NA	NA	NA	NA
Acer 1	0.21	0.06	0.33	0.11	0.72	0.08	0.22	0.14	0.76	32.30	0.38	93.46	4.57	0.27	6.26	5.71	6.85	4.30	2.79	1.06	3.85	0.29
Acer 3.1	-0.41	0.06	-0.66	0.11	-0.41	0.09	-0.13	0.20	NA	NA	NA	NA	NA	NA	NA	NA	NA	NA	NA	NA	NA	NA
SaU 1.3	0.14	0.05	0.32	0.09	-2.10	0.09	-1.21	0.14	5.78	32.08	0.07	91.38	5.15	0.35	8.26	0.66	1.83	1.08	0.28	0.36	0.46	0.03
SaU 1.4	1.26	0.05	1.87	0.08	5.09	0.08	2.47	0.16	0.41	6.47	0.14	93.62	4.92	0.26	6.12	6.99	4.79	4.59	3.54	0.12	5.09	0.36
SaU 5	0.05	0.05	0.13	0.08	0.17	0.09	-0.05	0.16	3.08	128.53	0.48	93.99	4.78	0.25	5.74	4.59	3.70	3.14	2.38	0.19	2.63	0.22
SaU 6	0.16	0.04	0.24	0.07	0.72	0.06	0.51	0.12	0.79	74.82	0.28	94.10	4.27	0.25	5.64	3.90	4.47	2.82	1.86	0.69	2.64	0.19
SaU 7	-0.01	0.05	-0.08	0.08	-0.30	0.08	-0.36	0.15	0.95	72.60	0.38	92.73	4.89	0.30	6.95	6.74	7.65	5.16	3.51	0.24	4.60	0.33
SaU 8	-0.08	0.05	0.00	0.07	0.61	0.07	0.48	0.13	1.97	24.40	0.20	94.38	3.96	0.24	5.38	3.45	4.14	2.64	1.75	0.61	2.38	0.17

Appendix

Table S2: Isotope compositions of cores and rims of zoned metal from CH chondrites.

sample	grain	$\delta^{56}\text{Fe}$ [‰]	2 σ	$\delta^{57}\text{Fe}$ [‰]	2 σ	$\delta^{62}\text{Ni}$ [‰]	2 σ	$\delta^{61}\text{Ni}$ [‰]	2 σ
PAT 91546	3.1 core	-5.00	0.08	-7.38	0.19	-5.83	0.13	-3.08	0.43
	3.1 rim	-3.39	0.10	-4.94	0.27	-1.79	0.37	-0.45	0.81
	3.2 core	-4.59	0.13	-6.85	0.23	-6.15	0.23	-3.14	0.34
	3.2 rim	-1.95	0.17	-3.01	0.36	0.00	0.24	-0.14	0.57
	3.4 core	-1.90	0.09	-2.88	0.14	-1.99	0.21	-0.84	0.22
	3.4 rim	-0.08	0.14	-0.09	0.22	0.63	0.22	1.23	0.66
	5.2 core	-0.74	0.10	-1.23	0.16	2.82	0.04	1.66	0.08
	5.2 rim	-0.49	0.10	-0.68	0.18	2.00	0.04	0.69	0.08
SaU 290	1.1 core	-7.65	0.11	-11.28	0.13	-9.81	0.18	-4.76	0.41
	1.1 rim	-1.24	0.12	-1.90	0.24	-2.94	0.26	0.01	0.57
	1.2 core	-2.19	0.11	-3.23	0.14	-5.31	0.19	-2.94	0.29
	1.2 rim	-0.36	0.16	-0.69	0.19	0.14	0.40	-0.61	0.41
Acfer 214	5.3 core	-3.78	0.11	-5.39	0.19	-3.73	0.19	-1.94	0.34
	5.3 rim	-0.13	0.14	-0.09	0.39	0.60	0.38	1.64	0.90

Appendix

Table S3: Element compositions of cores and rims of zoned metal from CH chondrites. *bd* = below detection.

sample	grain	Ge	Cu	Au	Fe (wt%)	Pd	Co (wt%)	Ni (wt%)	Pt	Mo	Ru	Ir	W	Os	Re
PAT 91546	3.1 core	0.18	0.58	0.79	90.14	4.60	0.40	9.63	7.34	7.27	7.15	3.99	0.11	4.73	0.32
	3.1 rim	4.29	29.76	1.66	91.76	4.74	0.33	7.91	6.22	6.69	5.00	3.18	0.14	4.65	0.36
	3.2 core	0.44	11.10	0.72	89.53	5.35	0.39	10.07	8.19	6.92	7.25	4.26	0.08	5.38	0.37
	3.2 rim	8.16	75.44	1.65	91.65	5.18	0.33	8.01	6.98	6.74	5.65	3.48	0.35	4.77	0.31
	3.4 core	0.01	0.59	0.48	91.84	5.04	0.35	7.80	6.14	9.66	5.42	3.16	0.32	3.62	0.30
	3.4 rim	1.93	11.65	0.79	93.33	4.90	0.28	6.38	6.63	8.45	4.58	3.52	0.32	5.29	0.38
	5.2 core	0.20	0.86	0.96	90.28	5.20	0.38	9.34	13.92	4.95	8.80	9.09	0.26	10.90	0.70
	5.2 rim	1.36	7.05	0.75	93.59	4.37	0.27	6.14	5.13	4.09	3.91	1.85	0.16	2.65	0.24
	1.1 core	0.19	1.88	0.05	90.76	5.00	0.35	8.88	6.95	5.91	6.09	3.28	0.12	3.05	0.26
SaU 290	1.1 rim	5.06	35.82	0.07	91.79	4.96	0.32	7.88	6.07	5.13	5.19	3.27	0.22	4.02	0.28
	1.2 core	0.19	1.03	0.05	91.18	5.36	0.34	8.48	7.37	6.13	6.04	3.42	0.17	3.91	0.28
	1.2 rim	1.67	13.01	0.08	92.93	4.98	0.28	6.78	6.75	6.19	4.53	3.75	0.30	5.18	0.33
Acfer 214	5.3 core	bd	1.03	0.06	91.45	4.91	0.34	8.20	6.93	5.38	5.86	3.31	0.11	4.30	0.29
	5.3 rim	bd	2.91	0.09	92.52	4.55	0.29	7.18	6.90	5.03	4.86	3.50	0.12	4.84	0.29

Appendix

4 APPENDIX PART IV

Table S1: Element compositions of analyzed CC chondrules. Red Pb values are unusually high and may be caused by contamination of the sample due to polishing.

chondrule	Li	Mg	Si	Sc	Ti	V	Cr	Mn	Cu	Zn	Rb	Sr	Y	Zr	Nb	Mo	Sn	La	Ce	Pr	Nd
	ppm	ppm	ppm	ppm	ppm	ppm	ppm	ppm	ppm	ppm	ppm	ppm	ppm	ppm	ppm	ppm	ppm	ppm	ppm	ppm	ppm
QUE1	0.84	246733.78	241827.98	7.57	695.72	114.09	3884.81	1310.11	4.14	32.06	0.08	12.10	1.63	4.59	0.55	1.42	1.22	0.36	1.12	0.17	0.74
QUE4	0.55	255630.43	252861.96	1.00	232.89	102.28	3874.97	604.02	4.82	49.86	0.13	3.72	0.12	0.63	0.36	0.64	1.56	0.14	0.54	0.16	0.19
QUE5	0.63	241988.90	233552.50	3.75	408.59	105.23	3530.75	875.94	11.11	50.85	0.31	6.71	0.88	2.09	0.70	0.98	1.64	0.21	0.78	0.18	0.51
QUE10	2.05	228940.48	226656.27	0.37	57.13	96.09	3029.16	570.51	16.13	79.66	0.17	2.72	0.14	0.47	0.12	1.99	1.60	0.20	0.43	0.07	0.06
QUE8	0.63	253257.99	248724.22	2.42	353.16	102.28	3422.56	681.71	0.56	23.51	0.09	5.16	0.37	1.27	0.37	0.48	0.71	0.15	0.66	0.07	0.34
QUE10.1	2.33	231312.92	223438.02	0.24	25.59	71.89	3294.71	597.17	1.28	25.96	0.08	1.06	0.02	0.10	0.09	0.61	0.66	0.02	0.06	0.01	0.01
MAC9	0.83	259189.10	256539.95	0.49	117.33	95.99	3884.81	490.53	1.75	29.41	0.06	1.36	0.13	0.39	0.17	0.42	0.99	0.07	0.43	0.33	0.05
MAC2	2.55	260968.43	259298.45	0.28	41.63	89.69	3737.28	482.15	1.06	24.00	0.06	0.14	0.02	0.08	0.12	0.43	0.99	0.01	0.11	0.01	0.09
MAC3	0.72	240209.57	242747.48	6.13	468.72	106.22	3432.40	450.92	0.80	33.64	0.22	7.68	1.61	3.98	0.36	0.46	1.22	0.27	0.78	0.25	0.59
MAC4	0.59	236057.80	233552.50	11.61	896.18	114.09	3206.19	769.31	0.38	22.03	0.48	15.24	2.96	7.17	0.67	0.49	0.95	0.47	1.37	0.25	1.05
MAC6	0.73	247920.00	244586.48	7.85	701.61	112.12	3520.91	616.21	0.31	24.59	0.07	11.11	1.74	4.56	0.57	0.46	1.01	0.35	1.17	0.17	0.65
MAC7	1.27	262154.65	251022.96	0.40	134.43	98.05	3412.73	545.37	0.86	24.10	0.06	1.44	0.02	0.18	0.19	0.48	0.99	0.03	0.31	0.02	0.09
SAU1	2.97	260375.32	264355.68	0.56	73.11	97.56	4592.92	845.48	20.65	38.06	0.17	40.42	0.13	0.45	0.15	0.80	0.83	0.03	0.17	0.01	0.04
SAU2	0.78	193946.99	262516.69	12.98	931.55	89.69	5930.48	3633.26	1.08	18.69	1.43	15.74	3.07	7.80	0.64	2.22	1.07	0.47	1.32	0.20	1.09
SAU3	0.56	253851.10	244586.48	2.50	376.75	108.18	4553.58	658.10	0.45	21.83	0.08	6.40	0.17	0.74	0.33	0.48	0.68	0.20	0.70	0.08	0.38
SAU4	0.56	260375.32	251942.46	1.23	220.51	101.30	4268.37	807.39	1.97	26.16	0.07	5.56	0.28	0.73	0.25	0.73	0.71	0.07	0.41	0.05	0.11
SAU6	0.69	250292.44	257459.45	4.08	420.97	80.74	4701.11	1272.02	0.48	23.31	0.08	6.13	0.72	2.17	0.38	0.81	0.92	0.19	0.73	0.07	0.44
SAU7	0.67	256223.54	249183.97	3.34	367.90	107.20	4199.52	959.73	0.26	22.72	0.07	5.10	0.62	1.83	0.35	0.70	0.75	0.16	0.60	0.08	0.37
SAU8	4.98	253851.10	254700.96	0.39	122.63	91.66	3983.16	691.62	2.87	37.96	0.07	2.53	0.10	0.28	0.16	1.57	0.82	0.03	0.24	0.02	0.05
SAU9	0.48	202843.64	274010.41	11.90	801.84	71.01	4946.98	1393.89	2.08	19.47	4.71	10.62	2.73	7.41	0.61	0.87	0.82	0.46	1.18	0.19	1.03
SAU10	0.75	253851.10	251482.71	4.08	430.99	109.17	4120.84	613.16	13.87	27.24	0.08	21.15	0.91	2.32	0.38	0.70	0.82	0.21	0.75	0.10	0.44
ISH2	1.17	205809.19	255160.70	15.24	1196.87	100.32	4091.34	2947.74	2.01	17.21	0.77	20.26	3.82	9.78	0.85	1.74	0.85	0.64	1.70	0.24	1.27
ISH3	0.63	249106.22	243666.98	5.31	586.64	109.17	4465.07	1736.65	0.34	20.26	0.08	6.50	0.87	2.68	0.47	1.15	0.87	0.26	0.93	0.10	0.54
ISH4	0.69	250885.55	251022.96	3.20	372.62	105.23	3648.77	868.33	2.49	25.47	0.07	5.09	0.62	1.69	0.35	0.62	0.94	0.16	0.64	0.07	0.35
ISH5	0.58	257409.76	258838.70	0.99	170.98	95.10	3796.29	520.23	4.39	25.18	0.07	1.93	0.14	0.50	0.22	0.59	1.19	0.05	0.35	0.02	0.15
ISH6	0.48	256223.54	243207.23	4.47	478.16	111.13	4091.34	1363.43	0.80	24.19	0.04	6.19	0.93	2.60	0.42	0.91	0.84	0.19	0.74	0.09	0.47
ISH7	0.98	254444.21	272171.42	0.33	139.14	94.51	3265.20	418.17	0.50	21.64	0.06	1.16	0.03	0.11	0.19	0.30	0.98	0.03	0.28	0.02	0.05
ISH12	0.71	255037.32	243207.23	2.02	316.02	104.25	3697.94	747.98	0.31	21.74	0.07	4.63	0.33	1.00	0.34	0.69	0.85	0.12	0.60	0.06	0.27

Appendix

Table S1 continued: Element compositions of analyzed CC chondrules. Red Pb values are unusually high and may be caused by contamination of the sample due to polishing.

chondrule	Sm	Eu	Gd	Tb	Dy	Ho	Er	Tm	Yb	Lu	W	Pb	Al	Ca	Fe	Na	O	Ce anom.
	ppm	ppm	ppm	ppm	ppm	ppm	ppm	ppm	ppm	ppm	ppm	ppm	ppm	ppm	ppm	ppm	wt%	in %
QUE1	0.25	0.09	0.25	0.06	0.39	0.08	0.26	0.03	0.30	0.02	2.53	1.04	11923.97	17129.62	16301.47	80.62	45.99	-31.11
QUE4	0.12	0.03	0.12	0.01	0.04	0.01	0.05	0.01	0.07	0.01	8.88	7.57	2667.15	4549.81	6851.58	269.95	46.57	-44.94
QUE5	0.23	0.06	0.14	0.03	0.17	0.04	0.10	0.02	0.17	0.02	20.56	16.62	6041.47	26689.69	7393.80	192.98	46.68	-38.29
QUE10	0.02	0.03	0.10	0.01	0.03	0.01	0.05	0.01	0.02	0.01	0.35	12.00	11836.03	12888.43	29207.36	5269.51	45.56	-45.78
QUE8	0.08	0.04	0.10	0.02	0.11	0.01	0.05	0.01	0.13	0.01	0.13	0.31	5300.73	6188.15	3400.55	66.39	46.75	-5.07
QUE10.1	0.05	0.01	0.13	0.01	0.04	0.00	0.02	0.01	0.03	0.00	0.04	0.30	11836.03	12888.43	29207.36	5269.51	45.56	-28.26
MAC9	0.04	0.03	0.12	0.00	0.04	0.01	0.02	0.01	0.05	0.01	0.15	0.88	-451.85	1403.19	3342.56	-118.44	47.68	-55.56
MAC2	0.03	0.02	0.15	0.01	0.02	0.01	0.04	0.01	0.07	0.00	0.11	0.07	65.39	160.05	6646.37	51.31	46.72	76.62
MAC3	0.24	0.07	0.26	0.05	0.26	0.07	0.21	0.03	0.18	0.03	0.18	1.01	8335.51	9615.26	16137.43	472.41	47.54	-54.19
MAC4	0.40	0.12	0.48	0.07	0.52	0.10	0.36	0.05	0.32	0.09	0.18	0.18	16839.45	19477.75	13143.09	231.04	46.80	-39.89
MAC6	0.26	0.09	0.33	0.05	0.33	0.08	0.22	0.04	0.23	0.04	0.18	0.25	12114.51	12424.09	4857.57	-66.15	46.81	-27.34
MAC7	0.08	0.02	0.10	0.01	0.02	0.01	0.03	0.01	0.05	0.01	0.11	0.10	670.06	1841.39	3204.64	-68.34	47.43	127.14
SAU1	0.06	0.02	0.10	0.01	0.05	0.01	0.02	0.01	0.02	0.01	0.17	0.26	-1269.35	303.23	6524.51	18.00	46.54	35.41
SAU2	0.41	0.15	0.36	0.10	0.59	0.12	0.35	0.08	0.43	0.06	0.01	0.09	15801.66	19754.50	17016.40	1862.90	46.69	-34.68
SAU3	0.13	0.07	0.16	0.02	0.10	0.01	0.01	0.01	0.15	0.01	0.18	0.04	4987.03	9178.12	6353.46	8.27	47.59	-16.71
SAU4	0.05	0.03	0.15	0.01	0.06	0.02	0.05	0.01	0.06	0.01	0.12	0.13	503.20	3438.84	7484.81	-54.23	46.46	6.09
SAU6	0.19	0.08	0.12	0.03	0.20	0.03	0.08	0.02	0.14	0.01	0.02	0.11	6680.65	9050.17	7334.41	174.13	46.20	-5.69
SAU7	0.11	0.05	0.15	0.03	0.15	0.04	0.09	0.01	0.12	0.01	0.18	0.04	5805.92	5439.10	6510.24	153.94	46.53	-21.58
SAU8	0.03	0.02	0.12	0.01	0.02	0.01	0.03	0.01	0.04	0.00	0.15	0.80	750.72	1674.31	10974.46	60.56	47.29	63.18
SAU9	0.31	0.11	0.43	0.07	0.52	0.11	0.30	0.06	0.31	0.05	0.00	0.16	14671.51	18163.02	10246.78	3007.76	47.20	-39.40
SAU10	0.08	0.06	0.16	0.02	0.25	0.04	0.12	0.02	0.17	0.02	0.09	0.23	5980.41	8953.86	6395.52	-13.62	46.75	-20.05
ISH2	0.48	0.14	0.60	0.09	0.70	0.15	0.43	0.08	0.48	0.07	0.02	0.04	22094.82	21266.76	17171.78	6280.36	46.52	-34.14
ISH3	0.25	0.07	0.12	0.04	0.25	0.06	0.12	0.02	0.23	0.02	0.17	0.06	8436.20	11621.04	15121.81	-18.73	46.43	-10.88
ISH4	0.16	0.06	0.16	0.02	0.14	0.03	0.12	0.02	0.14	0.01	0.14	0.34	5486.06	8441.37	13478.57	150.54	46.30	-9.02
ISH5	0.05	0.02	0.10	0.01	0.05	0.01	0.03	0.01	0.06	0.00	0.08	0.24	1975.14	2735.60	6806.46	143.73	46.34	86.93
ISH6	0.16	0.07	0.18	0.03	0.24	0.05	0.15	0.02	0.16	0.02	0.16	0.08	7413.16	6034.54	13147.17	90.47	46.13	-12.32
ISH7	0.02	0.03	0.20	0.01	0.02	0.01	0.01	0.01	0.02	0.01	0.05	0.05	448.38	1627.21	6417.96	45.96	46.97	82.37
ISH12	0.08	0.04	0.13	0.01	0.10	0.02	0.07	0.02	0.10	0.01	0.12	0.05	448.38	1627.21	6417.96	45.96	46.97	9.18

Appendix**5 CURRICULUM VITAE****Personal information**

E-mail	m.weyrauch@mineralogie.uni-hannover.de
Birth	20.03.1989 in Mülheim a.d. Ruhr
Nationality	German

Employment

Since 11/2014	Research assistant/PhD student at the Institut für Mineralogie, Leibniz Universität Hannover Chemical and isotopic analyses of Fe,Ni-alloys in meteorites via laser ablation in combination with mass spectrometry, clean lab work, presentation of the latest work at international conferences, preparation of scientific papers, supervision of bachelor/master students.
08/2014-10/2014	Research assistant at the Institut für Planetologie, Westfälische Wilhelms-Universität Münster Literature research on different topics in the field of planetary science, preparation of scientific papers, chemical analyses via electron microprobe and scanning electron microscope
09/2011-07/2014	Student assistant at the Institut für Planetologie, Westfälische Wilhelms-Universität Münster Literature research on different topics in the field of planetary science, proofreading of manuscripts, editing of plots and tables for publications, chemical analyses via electron microprobe and scanning electron microscope

Education

10/2011 – 01/2014	Study of Earth Sciences at the Westfälische Wilhelms-Universität Münster, Master of Science. Research areas: meteorites and planetary bodies, applied mineralogy, petrology, geochemistry.
10/2008 – 09/2011	Study of Earth Sciences at the Westfälische Wilhelms-Universität Münster, Bachelor of Science.

Appendix

07/1999-06/2008 Focus on: meteorites and planetary bodies, petrology, geochemistry. Basics in: chemistry, maths, physics, and biology.
Secondary school, Kopernikus Gymnasium Walsum, A-levels. Focus on: natural sciences and languages.

Internships

03/2011 **4 weeks at the Institut für Planetenforschung am Deutschen Zentrum für Luft- und Raumfahrt (Institute for Planetary Science at the German Centre for Aviation and Space flight)**

Mapping of surface areas of Mars and Moon with ArcGis.

09/2010 **3 weeks at Mineralogisches Museum am Steinmann-Institut, Bonn (Mineralogical Museum)**

Research on health issues related to gold mining and usage of gold in work materials. Procurement of exhibits, design of a display case, and writing of descriptions for exhibits.

Miscellaneous

Languages German (mother tongue)
 English (fluent, written and spoken)
 French (basic knowledge, A2)
 Spanish (basic knowledge, B1)

Language study travel 2 weeks in 07/2005: Summer Academy at Strathclyde University, Glasgow (Scotland)

Engagement 08/2016-02/2018: secretary of the association
 "Freunde der Geowissenschaften Hannover e.V."

 2016/2017: student member in the advisory board of the Deutsche Mineralogische Gesellschaft

 10/2012 – 10/2014: representative of the student body in the board of the Institut für Planetologie, Westfälische Wilhelms-Universität Münster

 2010 – 2012: member of the body of representatives of the students of the department for Earth Sciences, Uni Münster

Appendix

6 LIST OF PUBLICATIONS

Peer reviewed articles

- Weyrauch M.** and Bischoff A. (2012). Macrochondrules in chondrites – Formation by melting of mega-sized dust aggregates and/or by rapid collisions at high temperatures? *Meteoritics & Planetary Science* **47**, 2237-2250.
- Trigo-Rodriguez J., Di Llorca J., **Weyrauch M.**, et al. (2014). The Ardón L6 ordinary chondrite: A long hidden Spanish meteorite fall. *Meteoritics & Planetary Science* **49**, 1475-1484
- Horstmann M., Humayun M., Fischer-Gödde M., Bischoff A. and **Weyrauch M.** (2014): Si-bearing metal and niningerite in Almahata Sitta fine-grained ureilites and insights into the diversity of metal in the ureilite parent body. *Meteoritics & Planetary Science* **49**, 1948-1977.
- Bartoschewitz R., Appel P., Barrat J.-A., Bischoff A., ..., **Weyrauch M.**, Wimmer K. (2017). The Braunschweig meteorite – a recent L6 chondrite fall in Germany. *Chemie der Erde* **77**, 207-224.
- Bischoff A., Wurm G., Chaussidon M., Horstmann M., **Weyrauch M.**, and Weinauer J. (2017) The Allende multi-compound chondrule (ACC) – chondrule formation in a local super-dense region of the early solar system. *Meteoritics & Planetary Science* **52**, 906-924.
- Weyrauch M.**, Oeser M., Brüske A., and Weyer S. (2017). In situ high-precision Ni isotope analyses of metals by femtosecond-LA-MC-ICP-MS. *Journal of Analytical Atomic Spectrometry* **32**, 1312-1319.
- S.M. Chernozhkin, **M. Weyrauch**, S. Goderis, M. Oeser, S.J. McKibbin, I. Horn, L. Hecht, S. Weyer, P. Claeys, F. Vanhaecke (2017). Thermal equilibration of iron meteorite and pallasite parent bodies recorded at the mineral scale by Fe and Ni isotope systematics. *Geochimica et Cosmochimica Acta* **217**, 95-111.
- Weyrauch M.**, Horstmann M., and Bischoff A (2018). Chemical variations of sulfides and metal in enstatite chondrites – Introduction of a new classification scheme. *Meteoritics & Planetary Science* **53**, 394-415.

Conference contributions

- Weyrauch M.** and Bischoff A. *Macro chondrules in chondrites and their textural differences to normal-sized chondrules – indications for a different origin?. 75th Meteoritical Society Meeting*, Cairns, 2012.
- Horstmann M, Bischoff A, Pack A, Albrecht N, **Weyrauch M.**, et al. Mineralogy and oxygen isotope composition of new samples from the Almahata Sitta strewnfield. *75th Meteoritical Society Meeting*, Cairns, 2012.
- Weyrauch M.**, Horstmann M., Wurm G. and Bischoff A. Macro chondrules in chondrites – formation due to rapid collisions of fully molten spherules? *Paneth Kolloquium in Nördlingen*, 2012.
- Weyrauch M.**, Horstmann M. and Bischoff A. Major and minor element systematics in enstatite chondrite metal and sulfides. *Paneth Kolloquium in Nördlingen*, 2013.
- Bischoff A. Chaussidon M., and **Weyrauch M.** Mineralogy and chemistry of large chondrules formed. *77th Meteoritical Society Meeting*, Casablanca, 2014.

Appendix

- Weyrauch M.**, Horstmann M., and Bischoff A. Chemistry of sulfides and metal in enstatite chondrites - how many parent lithologies (bodies)? *77th Meteoritical Society Meeting, Casablanca, 2014.*
- Trigo-Rodriguez J.M., Llorca J. **Weyrauch M.**, Bischoff A., ..., and Mestres N. Ardón: A long hidden L6 chondrite fall. *77th Meteoritical Society Meeting, Casablanca, 2014.*
- Weyrauch M.**, Horstmann M. and Bischoff A. Sulfide chemistry of enstatite chondrites – identification of EH- and EL-subgroups? *Deutsche Mineralogische Gesellschaft Meeting, Jena, 2014.*
- Weyrauch M.**, Zipfel J., Weyer S. and Oeser M. Diversity of CB and CH Chondrite Metal. *Goldschmidt Conference, Prag, 2015.*
- Weyrauch M.**, Zipfel J. and Weyer S. Ni isotope composition of zoned metal grains in CBb chondrite Hammadah al Hamra 237. *Paneth Kolloquium in Nördlingen, 2015.*
- Weyrauch M.**, Zipfel J. and Weyer S. Constraints on the formation of zoned metal grains in CB and CH chondrites from Ni and Fe isotope signatures and HSE abundances. *4th HSE Geochemistry Workshop, Durham, 2016.*
- Weyrauch M.**, Weyer S., and Zipfel J. Fe and Ni isotope composition of metal grains from CH and CB chondrites. *79th Meeting of the Meteoritical Society, Berlin, 2016.*
- Weyrauch M.**, Zipfel J., and Weyer S. Formation conditions of zoned and unzoned metal grains in CB and CH chondrites. *80th Meeting of the Meteoritical Society, Santa Fe (NM), 2017.*
- Weyrauch M.**, Weyer S., and Zipfel J. The relationship of zoned and unzoned metal in CH and CB chondrites. *Goldschmidt Conference, Paris, 2017.*
- Chernozhukhin S.M., Goderis S., **Weyrauch M.**, ..., and Vanhaecke F. Implications of Fe and Ni stable isotope ratios for the formation of the pallasite parent body. *Goldschmidt Conference, Paris, 2017.*
- Weyrauch M.**, Zipfel J., and Weyer S. Origin of metal in CR-clan chondrites – constraints from Fe and Ni isotopes and highly siderophile elements. *Paneth Kolloquium in Nördlingen, 2017.*